# Multiparticle configurations in $^{155}$Lu ($N = 84$) and $^{158}$Ta ($N = 85$)

Thesis submitted in accordance with the requirements of the University of Liverpool for the degree of Doctor in Philosophy

by

**Robert John Carroll**

Oliver Lodge Laboratory

2012

This thesis is dedicated to my Mum and Dad.

Thank you.

*"If you aren't having any ideas, you aren't having any good ones."*

Professor Martin L. Perl, Winner of the 1995 Nobel Prize in Physics

*"The things one feels absolutely certain about are never true."*

*"The Picture of Dorian Gray"* by Oscar Wilde

*"Impossible is just a word to let people feel good about themselves when they quit."*

*"Skies of Arcadia"* by Sega, Overworks

# Acknowledgements

I would like to say a huge thank you to my supervisor Dr. David Joss for providing the opportunity to work at the cutting edge of nuclear physics research and for his many words of help and encouragement during my studies.

I would like to thank Prof. Robert Page for many useful and interesting discussions, which often changed my perspective of the problems at hand.

I am incredibly grateful for the example set by Dr. Heidi Watkins, who was always looking out for me. You have been a great role model and much valued friend.

Many thanks to Dr. David O'Donnell, Dr. Paul Sapple, John Revill and Liam Gaffney for putting up with me bouncing ideas off you. Your thoughts have always been appreciated.

Thanks to all members of the Nuclear Physics group at the University of Liverpool for being a very positive influence on my experiences here. Experiments, conferences, the summer school and daily life would have been less use and much less enjoyable without such a good group of friendly and intelligent people.

I would like to thank the staff at the University of Jyväskylä for many a patient explanation of the more subtle aspects of the experimental apparatus.

I would like to recognise the collaborators involved in this research and thank them for their contributions.

I would also like to acknowledge the financial support of the STFC, which has facilitated my involvement in this research.

Finally, I would like to say a big thank you to all of my friends and family for their support. In particular, members of the Liverpool University Fencing Club have made this time a very enjoyable one for me and have provided an effective relief to many a stressful day.

# Abstract

Excited states in $^{155}$Lu and $^{158}$Ta have been populated in fusion evaporation reactions at the Accelerator Laboratory at the University of Jyväskylä. Gamma-ray spectroscopy techniques have been employed, using both the JUROGAM spectrometer at the target position and the GREAT spectrometer at the focal plane of the RITU separator, and level schemes have been constructed.

Gamma-ray spectroscopy performed on $^{155}$Lu has revealed new structures at high spin and has confirmed spin isomerism as the mechanism by which the decay of the $^{155m2}\mathrm{Lu}_{(25/2^-)}$ state is hindered. The previous level scheme has been revised and compared with systematic trends across $N = 84$ isotones. Single-particle configurations have been assigned to low-lying states and mechanisms expected to construct structures at higher spin are discussed.

Previously, no excited states in the doubly odd $^{158}$Ta nucleus were known above the two low-lying $\alpha$-decaying states, which are proton unbound. For the first time, excited states built on the $^{158m1}\mathrm{Ta}_{(9^+)}$ $\alpha$-decaying state have been observed. Comparisons with $N = 85$ isotones are made and the interactions between nucleons in the $\pi h_{11/2}$, $\nu h_{9/2}$ and $\nu f_{7/2}$ orbitals are discussed.

A new isomeric state, which decays by both $\alpha$-particle and $\gamma$-ray emission, has been observed at high spin in $^{158}$Ta. No proton decay is observed from this state, despite a large proton Q-value. This hindrance to proton decay can be understood to be an effect of the centrifugal barrier at high spin. This introduces the possibility of other high-spin isomers existing beyond both the proton and neutron drip lines.

# Contents

# Chapter 1

# Introduction

The atomic nucleus is a unique system that is home to phenomena that cannot be found in any other known system. It is a many-body system whose properties are defined by the behaviour of its constituent nucleons, which are strongly interacting fermions. The nucleus is poorly understood on a microscopic level. The interactions between nucleons themselves is a many-body problem that has yet to be solved and so a "bottom up" approach to understanding the nucleus is of limited use. Furthermore, the amount of computing time required to perform such calculations on all but the lightest nuclei is completely unfeasible.

The solution to this problem has been to develop nuclear models that describe the observed phenomena as closely as possible and today the field of nuclear physics is concerned with the development of such models and the acquisition of experimental data with which to test their validity [1].

Although developing nuclear models vastly simplifies and streamlines the problems associated with describing the nucleus, there are still many difficulties facing their development. There are thousands of different known nuclei [2] and the difference of a single nucleon can make large changes to the properties of the nucleus. Earlier models are based on the properties of nuclei close to stability, however, im-

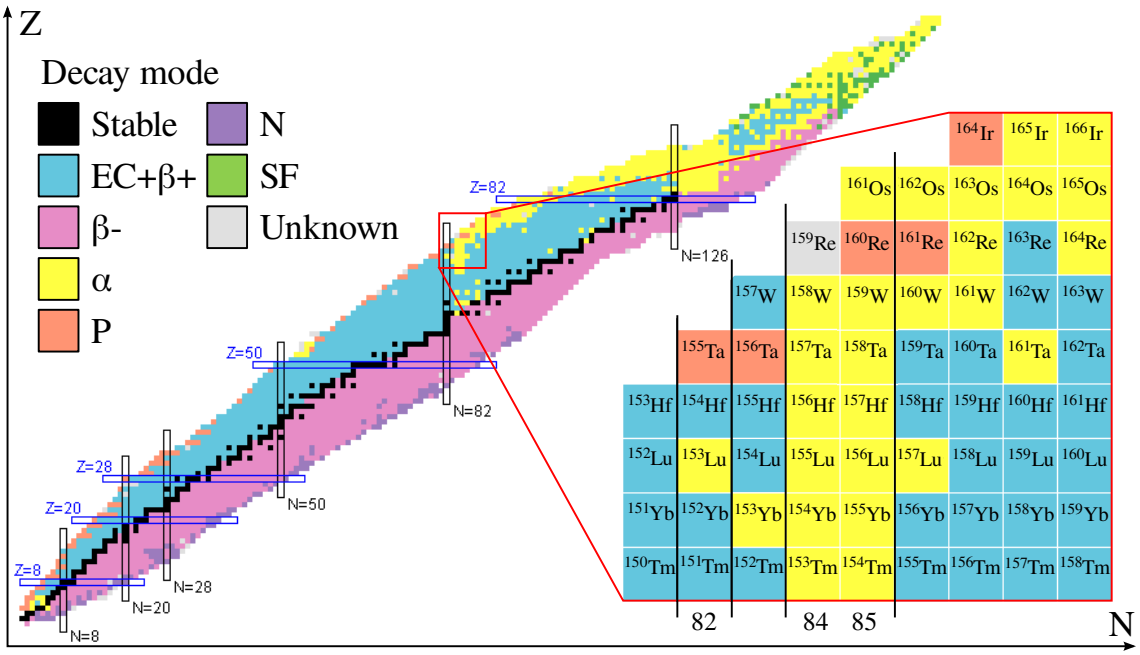


Figure 1.1: The chart of nuclides indicating the mode by which nuclei decay [3]. The region above $N = 82$ close to the proton drip line is enlarged.

provements in accelerator and detector technology have pushed back the observable limits, enabling more rigorous testing of the current models far from stability. Nuclei under conditions such as extreme isospin, spin, mass and deformation are examples of conditions where new phenomena may emerge resulting in stringent tests of nuclear models.

The chart of nuclides, shown in Figure 1.1, shows known nuclei as a function of proton number $Z$ and neutron number $N$. The chart depicts a line of stability for particular combinations of $Z$ and $N$. The chart clearly shows separate regions, either side of the line of stability, which correspond to nuclei that are deficient in either protons or neutrons. At the extremes of these regions are the proton and neutron drip lines, beyond which protons and neutrons, respectively, are unbound within the nucleus.

Such extremes provide an interesting testing ground for nuclear models because they are far from the stable isotopes upon which early nuclear models are based.

Furthermore, the range of nuclides make it possible to study systematic trends across chains of nuclei, displaying the effects of repeatedly adding or removing individual nucleons from a system.

This work is concerned with nuclei close to the proton drip line and the $N = 82$ shell closure. In this region, nuclei can be considered as a number of valence particles coupled to a semi-magic $^{146}$Gd core and the orbitals available for nucleon occupation are $1h_{11/2}$, $2d_{3/2}$ and $3s_{1/2}$ for protons, and $2f_{7/2}$, $1h_{9/2}$ and $1i_{13/2}$ for neutrons. The experimental investigation of isotone chains in such neutron-deficient nuclei is a probe of the dependence of single-particle states, based on the coupling of a small number of valence nucleons, on the atomic number $Z$.

The $^{155}$Lu nucleus is the lowest $Z$ isotone ($N = 84$) in which a high-spin $25/2^-$ isomer, built upon a configuration of aligned neutrons, has been observed [4]. Although the nature of the isomerism is thought to be due to the large spin change between the initial and final states this has not been verified. The lowering in excitation energy of the $25/2^-$ state with respect to the $23/2^-$ state across $N = 84$ isotones with increasing $Z$ is considered to be the cause of such a spin change occurring in $^{155}$Lu but not in the lighter isotones. Gamma-ray spectroscopy has been performed on excited states in $^{155}$Lu in order to confirm the nature of the high-spin isomer, identify states above the isomer and assess the evolution of structure approaching the proton drip line with increasing $Z$.

Experimental studies of $N = 85$ isotones have also been extended to excited states in doubly-odd $^{158}$Ta, which is the lowest in $Z$ beyond the proton drip line [5]. Prior to this work, nothing was known about excited states above the $\alpha$-decaying $(2^-)$ and $(9^+)$ states, however, many of its isotones have been studied and show a lowering in excitation energy of configurations involving a $h_{9/2}$ neutron as a function of increasing $Z$. This can be seen in the change in energy between the $(9^+)$ and $(10^+)$ states, which is observed to decrease with increasing $Z$. This energy difference has

not been confirmed in nuclei as high in $Z$ as $^{159}$W ($Z = 74$) or $^{160}$Re ($Z = 75$) [6], nor has it been observed in $^{156}$Lu [4]. Spectroscopy of excited states in $^{158}$Ta has revealed structures that have never been seen before and comparison with previously studied isotones show how these structures have been affected by the increasing proton valence space.

# Chapter 2

# Physics background

## 2.1 Nuclear models

The atomic nucleus is a complex system that comprises from one to hundreds of nucleons all of which interact strongly with neighbouring nucleons but weakly with those at distances greater than ∼1 fm. This is a particularly difficult system to describe using the interactions of the individual particles and using calculations of this sort to describe heavy elements would require an unfeasible amount of computing power. The solution to this problem has been to develop mathematical models that describe phenomena displayed by the nucleus. This reduces the problems associated with calculating the properties of heavy nuclei by forming a more tractable problem.

One of the main assumptions is that each nucleon in the nucleus moves in a mean field potential, which describes an effective interaction, rather than interacting with many particles simultaneously. A particle confined within a potential is restricted to discrete energies. Nucleons cannot transfer energy when they scatter due to the limited availability of potential final states. The only unoccupied levels are at higher excitation energies, usually out of the range of scattering energies.

The formation of discrete energy levels within a potential results in the existence

of shell structure. Large energy differences between groups of levels, which are close in energy or degenerate, form regions of high level density, or shells. When a shell has vacancies, nucleons can be excited into higher energy states within the shell with relative ease. When a shell is full, available levels for nucleon excitation are much higher in energy and so the nucleus is more stable against excitation. Experimental evidence for shell structure is abundant, in particular, the evidence for magic numbers is indicative of the large energy differences that would be incurred by the closure of a shell [1].

The choice of potential will affect the calculated magic numbers due to differences in the relative positions of the levels and so the development of a potential that adequately describes this phenomenon is particularly important. Commonly considered potentials are the square well, harmonic oscillator and Woods-Saxon potentials, Figure 2.1.

The square well potential is defined as

$$V(r) = \begin{cases} -V_0 & r \leq R \\ 0 & r > R \end{cases}, \tag{2.1}$$

where $r$ is the distance from the centre of the nucleus, $R$ is the nuclear radius and $V_0$ is the depth of the well. The base of this potential is flat, which is representative of the short range of the strong interaction. The edges of the square well are sharp and offer no realistic description regarding the effective interaction at the surface of the nucleus. The first two magic numbers can be correctly reproduced using the square well potential [1].

The harmonic oscillator potential can be defined as

$$V(r) = \begin{cases} -V_0[1 - (r/R)^2] & r \leq R \\ 0 & r > R \end{cases}. \tag{2.2}$$

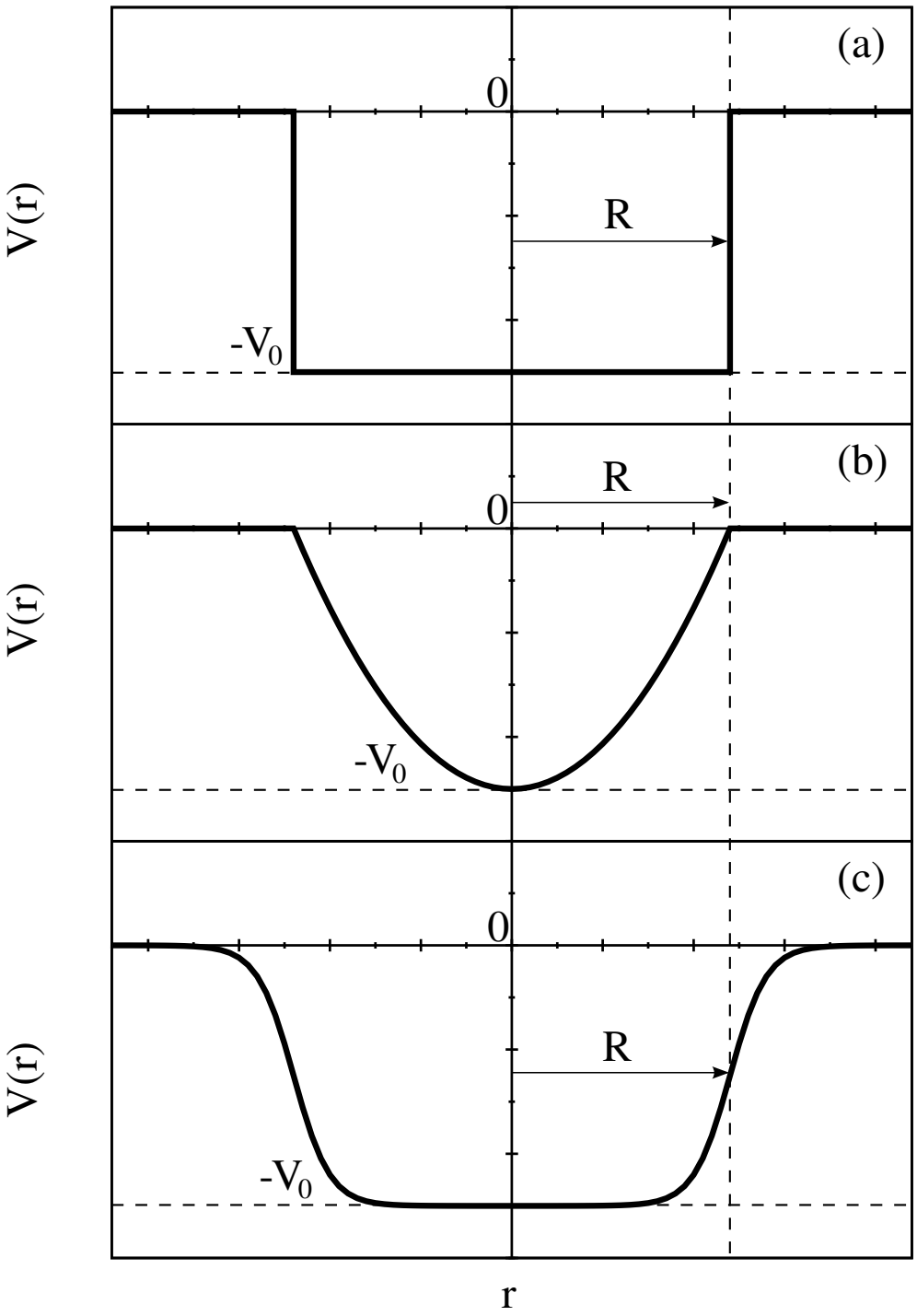


Figure 2.1: Nuclear potentials as a function of the distance from the centre of the nucleus $r$. **(a)** Square well, **(b)** Harmonic oscillator and **(c)** Woods-Saxon potentials. The nuclear radius is indicated by $R$ and the depth of the potential by $V_0$.

The sharp edges inherent to the square well are not present in this potential, however, a number of features of the harmonic oscillator do not accurately represent nuclear behaviour. The potential gradually increases from the centre of the nucleus, reminiscent of longer range forces that would cause nucleons to be attracted to the centre of the nucleus, which is not the case. The first three magic numbers can be reproduced using the harmonic oscillator potential [1].

As neither of these potentials correctly describe the nucleus improvements must be made. The Woods-Saxon potential is an example of such an improvement and describes the nucleus using well depth, nuclear radius and skin diffuseness terms [7]. It can be written as

$$V(r) = \frac{-V_0}{1 + exp[(r - R)/a]}, \tag{2.3}$$

where $a$ is the diffuseness term. The flat base of this potential is an appropriate description of the mean field as all nucleons away from the surface should feel a similar short ranged attraction. The smooth edge describes the decrease in the attractive force acting on nucleons at the surface of the nucleus. As with the harmonic oscillator, the Woods-Saxon potential can be used to reproduce the first three magic numbers.

Levels calculated using the Woods-Saxon potential are shown in Figure 2.2 [1]. Only the first three magic numbers are reproduced and so further modifications must be made to the potential to extend this model to heavier nuclei. The spin-orbit interaction is such a modification and alters the force acting on a nucleon depending on the coupling of its $l$ and $s$ quantum numbers, relieving the degeneracy of spin-orbit partners [1, 8, 9]. The spin-orbit modification can be written as

$$V(r) \Rightarrow V(r) + V_{so}(r)\vec{l} \cdot \vec{s}, \tag{2.4}$$

where $V_{so}(r)$ is the strength of the interaction, $l$ is the orbital angular momentum

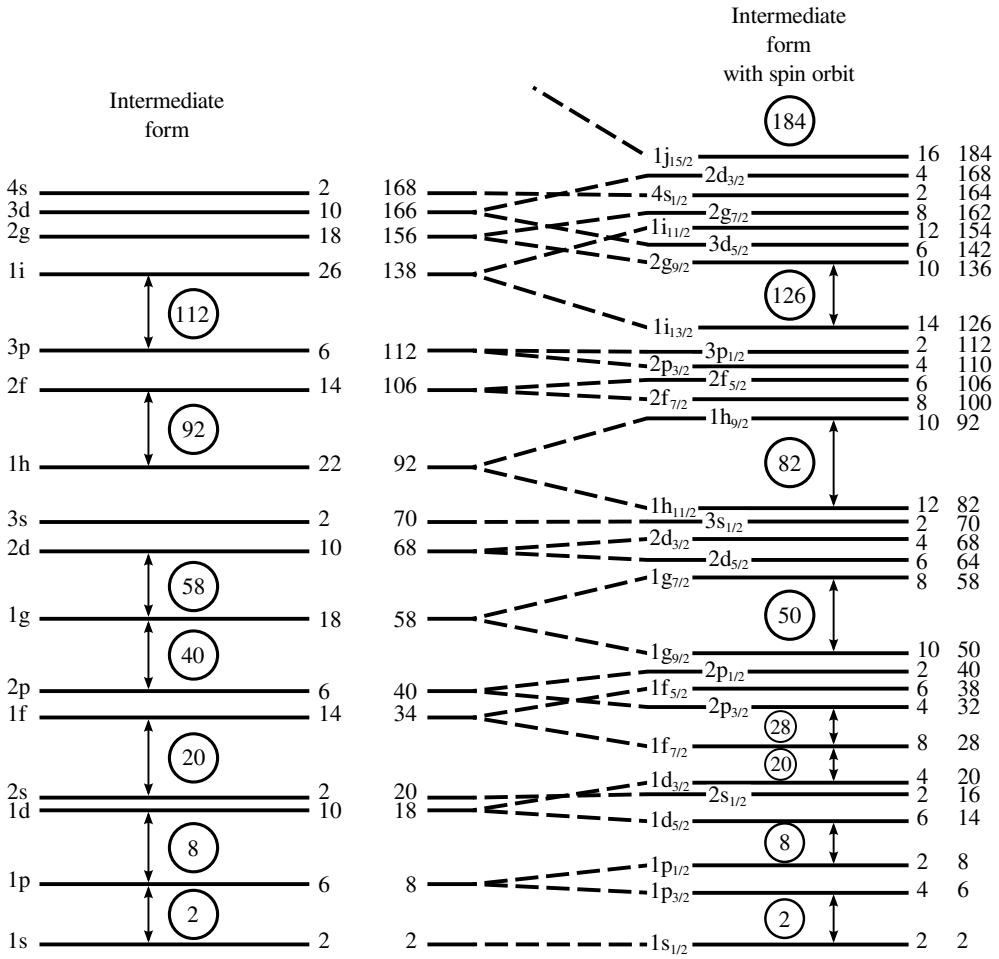


Figure 2.2: Levels calculated using the Woods-Saxon potential *(left)* without the spin-orbit interaction and *(right)* with the spin orbit interaction [1]. The experimentally verified magic numbers are better reproduced with the spin-orbit interaction included.

quantum number and $s$ is the spin quantum number. The effect of including the spin-orbit term on calculated values is shown in Figure 2.2. This modification is crucial in order to match nuclear models with observed phenomena.

## 2.2 The drip lines

The nucleus is held together by a total binding energy, which is defined as the difference between the total mass of the constituent nucleons and the total mass of

the system

$$B(A,Z) = ZM_P + (A-Z)M_N - M(A,Z), \tag{2.5}$$

where $B$ is the binding energy, $Z$ and $A$ are the atomic and mass numbers, respectively, $ZM_P$ and $(A-Z)M_N$ are the sums of the individual proton and neutron masses, respectively and $M$ is the total mass of the nucleus. The differences in the binding energy between one system and another, one nucleon lighter, enable the separation energy of an individual nucleon to be defined as

$$\begin{aligned} S_P(A,Z) &= B(A,Z) - B(A-1,Z-1), \\ S_N(A,Z) &= B(A,Z) - B(A-1,Z), \end{aligned} \tag{2.6}$$

where $S_P$ and $S_N$ are the separation energies for a single proton or neutron, respectively. For nuclei subject to extreme neutron or proton deficiency, the single-particle separation energies can fall below zero resulting in nuclei that are unbound. This occurs when

$$\begin{aligned} \left(\frac{\partial B}{\partial Z}\right)_{N=const} &= 0, \\ \left(\frac{\partial B}{\partial N}\right)_{Z=const} &= 0, \end{aligned} \tag{2.7}$$

for $S_P$ and $S_N$, respectively, where $N$ is the neutron number. These limits are called the drip lines. The nuclides that are the focus of this work lie close to and beyond the proton drip line.

Beyond the proton drip line no additional energy is required to remove a proton from the nucleus, however, the presence of the Coulomb and centrifugal barriers ensure that decay by proton emission is hindered. For this reason it is possible to perform spectroscopy on nuclei beyond the proton drip line.

## 2.3 Gamma-ray transitions

The study of excited states in atomic nuclei is crucial for gaining insight into nuclear behaviour, revealing arrangements of nucleons within the nucleus and the energies required for such arrangements to occur. The nucleus can be produced in excited states upon formation in a nuclear reaction or a radioactive decay. Where possible, $\gamma$ rays are emitted in order to lose both energy and angular momentum. These $\gamma$ rays are a valuable probe of the structure of the nucleus as they are a direct consequence of the de-excitation process.

The emission of $\gamma$ rays accounts for differences between the initial and final states that must be conserved, including energy, angular momentum and parity. This gives rise to selection rules that determine the properties of the emitted $\gamma$ rays. The energy carried by the transition is approximately equal to the difference in the excitation energies of the initial and final states. A small fraction of this energy is transferred to the nucleus to conserve momentum as the $\gamma$ ray is emitted, however, this energy is negligibly small for $\gamma$-ray energies $< 5$ MeV and so, in this work, the energy of the transition is considered to be

$$E_\gamma = E_i - E_f, \tag{2.8}$$

where $E_i$ and $E_f$ are the excitation energies of the initial and final states respectively. Measuring the energy of an emitted $\gamma$ ray indicates the difference in excitation energy between the initial and final states. The difference in the angular momentum between the initial and final states must also be conserved such that

$$\vec{L} = \vec{I_i} - \vec{I_f}, \tag{2.9}$$

where $\vec{I_i}$ and $\vec{I_f}$ are the angular momentum of the initial and final states and $\vec{L}$ is the

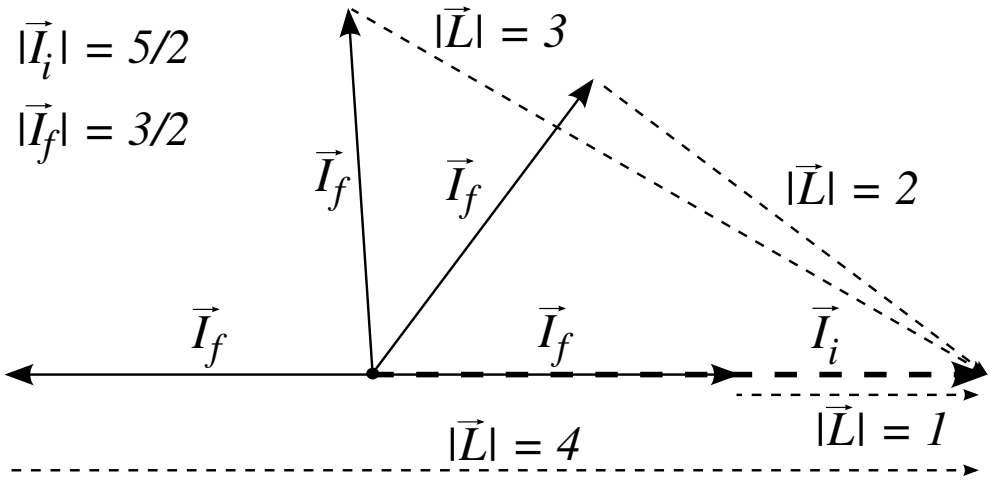


Figure 2.3: A vector diagram corresponding to the selection rule in Equation 2.10, demonstrating the angular momentum $\vec{L}$ that can be carried away from the nucleus by a $\gamma$-ray transition when the nucleus de-excites from an initial state to a final state with angular momentum $I_i = 5/2$ and $I_f = 3/2$.

angular momentum carried from the nucleus by the $\gamma$-ray transition. A consequence of Equation 2.9 is that a range of possible angular momenta are available for the $\gamma$-ray transition to carry away from the nucleus and gives rise to the selection rule

$$|I_i - I_f| \leq L \leq I_i + I_f, \tag{2.10}$$

where $I_i$ and $I_f$ are the initial and final state angular momentum and $L$ is the multipolarity of the $\gamma$-ray transition. This is demonstrated diagrammatically in Figure 2.3.

The conservation of parity during the decay from the initial state to the final states is also accounted for by the $\gamma$-ray transition. The parity of a wavefunction can be defined by reflecting its co-ordinates about the origin as indicated by

$$\psi(x) = \begin{cases} \psi(-x) & \text{(even parity, } \pi = 1) \\ -\psi(-x) & \text{(odd parity, } \pi = -1) \end{cases} \tag{2.11}$$

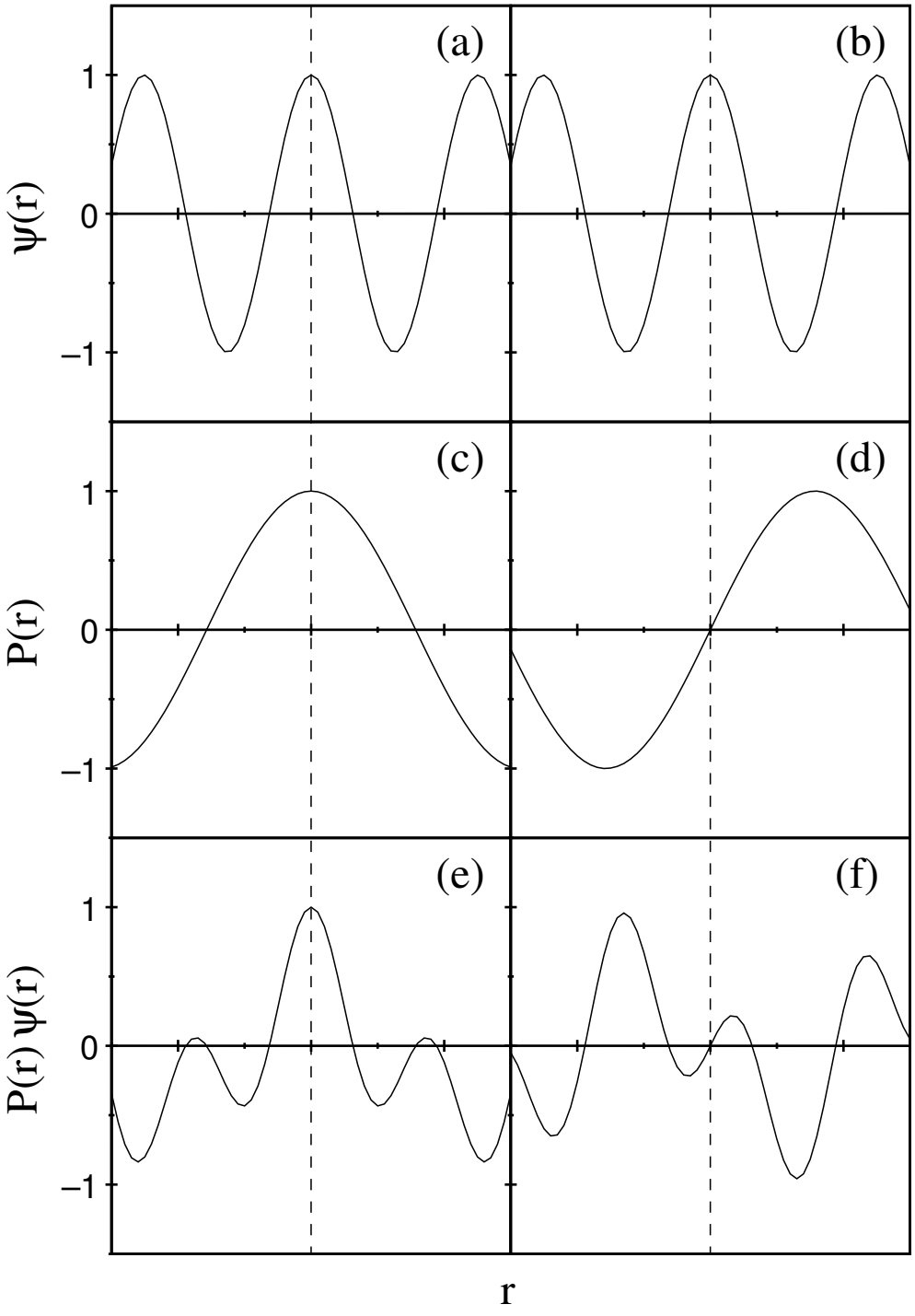


Figure 2.4: The effect of $\Delta\pi = no$ and $\Delta\pi = yes$ transitions on the parity difference between an initial and final state. **(a)** and **(b)** An initial state $\psi(r)$ with even parity. **(c)** A $\Delta\pi = no$ function, $P(r)$. **(d)** A $\Delta\pi = yes$ function, $P(r)$. **(e)** A final state following the $\Delta\pi = no$ transition. The parity remains even. **(f)** A final state following the $\Delta\pi = yes$ transition. The parity has changed from even, $\pi_i$, to odd, $\pi_f$.

| $L$ | $T_{el}$ (s) | $T_{magn}$ (s) |
|---|---|---|
| 1 | $6.73\ A^{-2/3}\ E_{\gamma}^{-3} \times 10^{-15}$ | $2.24\ A^{0}\ E_{\gamma}^{-3} \times 10^{-14}$ |
| 2 | $9.37\ A^{-4/3}\ E_{\gamma}^{-5} \times 10^{-9}$ | $3.12\ A^{-2/3}\ E_{\gamma}^{-5} \times 10^{-8}$ |
| 3 | $1.98\ A^{-2}\ E_{\gamma}^{-7} \times 10^{-2}$ | $6.60\ A^{-4/3}\ E_{\gamma}^{-7} \times 10^{-2}$ |
| 4 | $6.30\ A^{-8/3}\ E_{\gamma}^{-9} \times 10^{4}$ | $2.10\ A^{-2}\ E_{\gamma}^{-9} \times 10^{5}$ |
| 5 | $2.83\ A^{-10/3}\ E\gamma^{-11} \times 10^{11}$ | $9.43\ A^{-8/3}\ E_{\gamma}^{-11} \times 10^{11}$ |

Table 2.1: Half-lives based on Weisskopf estimates for electric and magnetic transitions for the first five orders of multipolarity [10], where $A$ is the mass number and $E_{\gamma}$ is the $\gamma$-ray energy in MeV.

and can be determined using

$$\pi \;=\; (-1)^{l}, \tag{2.12}$$

where $l$ is the orbital angular momentum quantum number of the state. The parity change incurred by a particular $\gamma$-ray multipolarity is given by

$$\begin{aligned} \Delta\pi(EL) &= (-1)^{L}, \\ \Delta\pi(ML) &= (-1)^{L+1}, \end{aligned} \tag{2.13}$$

where

$$\Delta\pi = 1 = no,$$
$$\Delta\pi = -1 = yes,$$

labels $E$ and $M$ denote electric and magnetic transitions, respectively, and $L$ is the angular momentum carried away by the transition. The effect of $\Delta\pi = no(yes)$ on the parity of the final state is demonstrated in Figure 2.4. Equations 2.10 and 2.13 form the selection rules for allowed $\gamma$-ray multipolarites for transitions between an initial state $I_i^{\pi_i}$ and final state $I_f^{\pi_f}$.

Theoretical estimates of the lifetime of a $\gamma$-decaying state were suggested by Weisskopf [11], assuming a single proton is responsible for the transition. Although

these estimates are crude, they are considered in this work when constraining the multipolarities of $\gamma$-ray transitions and assessing the single-particle nature of a transition. Weisskopf estimates are shown in Table 2.1.

## 2.4 Radioactive $\alpha$ decay

The phenomenon of radioactive $\alpha$ decay is of great importance to the field of nuclear physics, providing insight into the structure of nuclei from which they are emitted and identifying nuclei due to their distinct decay energies. The $\alpha$ particle itself is identical to a $^4$He nucleus and is a strongly bound system as indicated by the difference between the total mass of the system and the mass of its constituent nucleons. It can exist unbound within the nucleus, that is, its separation energy can be such that it does not require any additional energy to escape. This gives rise to the currently accepted mechanism by which $\alpha$ decay occurs, which requires that the $\alpha$ particle be contained within the nucleus by a Coulomb barrier through which it must quantum tunnel in order to escape [12], as illustrated in Figure 2.5. This prevents the decay from occurring immediately, but also provides a means by which the particle may not only escape but, due to variations in the energy and barrier conditions, may have a unique half life.

The probability of $\alpha$-particle emission from a nucleus is:

$$P_{\alpha\ decay} = P_{preform}.P_{tunnel} \tag{2.14}$$

where $P_{preform}$ is the probability of the $\alpha$ particle existing within the nucleus and $P_{tunnel}$ is the probability of the $\alpha$ particle penetrating the Coulomb barrier. The tunnelling probability can be calculated using models of the Coulomb barrier and the probability of $\alpha$-particle emission is related to the measurable half-life of the decay.

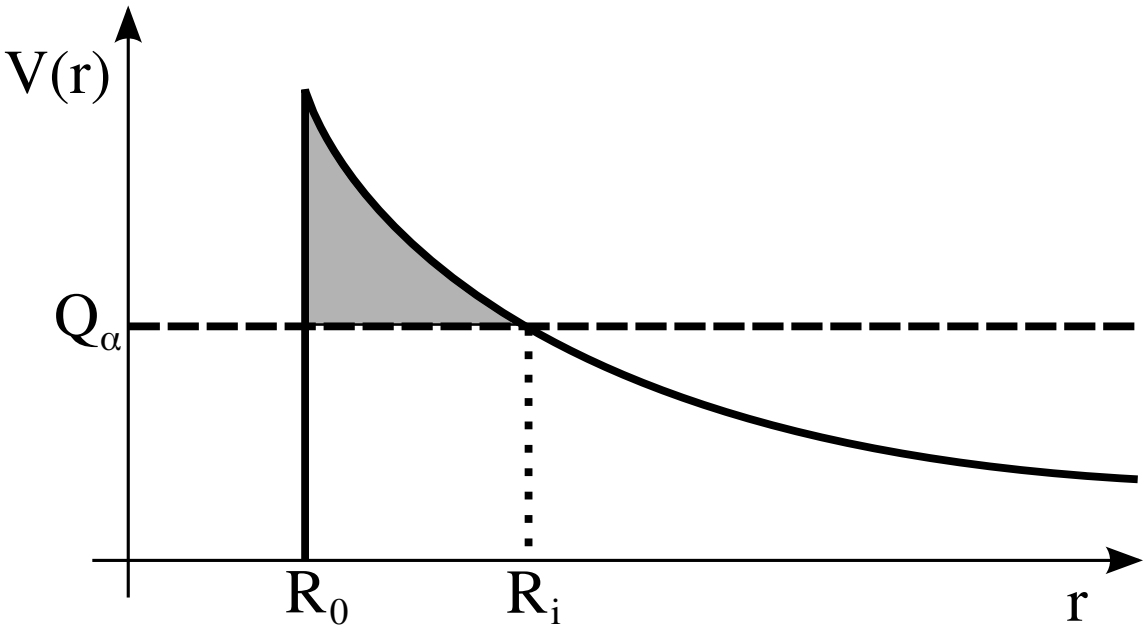


Figure 2.5: Schematic plot of an $\alpha$ particle tunnelling through a Coulomb barrier. $R_0$ represents the nuclear radius and $R_i$ indicates the distance at which the $\alpha$ particle has effectively escaped the nucleus. The shaded region indicates the barrier through which the $\alpha$ particle must quantum tunnel in order to escape the nucleus.

The probability of the $\alpha$ particle forming in the nucleus prior to decay can be used as a probe into the structure of the decaying nucleus. For a given potential barrier and Q-value, the half-life is dependant on the probability of the $\alpha$ particle forming and so longer half-lives would suggest structural hindrance. The opposite would be true of decays with shorter half-lives. This can be discussed in terms of the reduced decay width

$$\delta^2 = \frac{\lambda_{exp} h}{P_{tunnel}} \; [eV], \tag{2.15}$$

where $\lambda_{exp}$ is the experimental partial decay constant. As a guide, unhindered decays have a $\delta^2$ of $\sim$40 keV while for hindered decays it is $\sim$1 keV [13], although comparison with neighbouring nuclei would provide more useful values.

As previously stated, the tunnelling probability can be obtained by modelling the barrier through which the $\alpha$ particle must penetrate in order to escape, and can

be written as

$$P_{tunnel} = e^{-2G}, \tag{2.16}$$

where $G$ is the Gamow factor, which represents the barrier that must be penetrated before the $\alpha$ particle can escape from the nucleus, as indicated by the shaded region in Figure 2.5. Appropriate theoretical calculations to construct such a barrier, assuming a spherical nucleus, are discussed by Rasmussen [14] and have been adopted here. The Coulomb barrier can be constructed using an electric potential

$$V_{Coulomb}(r) = \frac{Z_D Z_\alpha e^2}{4\pi\epsilon_0 r}, \tag{2.17}$$

where $r$ is the distance from the centre of the nucleus and $Z_D$e and $Z_\alpha$e indicate the charge on the daughter nucleus and the $\alpha$ particle respectively.

In addition to the Coulomb barrier, $\alpha$ decays that carry angular momentum from the nucleus face additional resistance to their emission due to the increase in the potential barrier. This can be accounted for by adding a centrifugal term

$$V_{centrifugal}(r) = \frac{\hbar^2}{2mr^2} l(l+1), \tag{2.18}$$

to the barrier, where $m$ is the reduced mass of the $\alpha$ particle and $l$ is the angular momentum it carries from the nucleus.

The potential barrier is considered to drop rapidly at the surface of the nucleus due to the short-range strength of the nucleon-nucleon interaction. An appropriate modification to the barrier potential [15] to incorporate a smooth transition at the edge of the nucleus has been adopted,

$$V_{surface}(r) = -1100 \exp\left(-\left[\frac{r - 1.17A^{\frac{1}{3}}}{0.574}\right]\right) \ [MeV], \tag{2.19}$$

where $r$ is the distance from the centre of the nucleus and $A$ is the nuclear mass.

This modification is only valid for distances close to the surface of the nucleus, with $r \geq 7$ fm. The total potential barrier and its constituents are plotted in Figure 2.6. The greater the Q-value of the $\alpha$ particle, the greater the tunnelling probability.

Radioactive $\alpha$ decay occurs when the $\alpha$ particle has successfully tunnelled through the barrier. The mass of the $\alpha$ particle is such that an observable fraction of the Q-value, $\sim$2.5 % near $A = 158$, is transferred to the daughter nucleus due to conservation of momentum. The kinetic energy available to the $\alpha$ particle after losing a fraction of the Q-value to the daughter nucleus, assuming that the mother nucleus was at rest, is given by

$$T_\alpha = \frac{Q}{1 + \left(\frac{M_\alpha}{M_D}\right)} \tag{2.20}$$

where $M_\alpha$ and $M_D$ are the masses of the $\alpha$ particle and the daughter nucleus respectively.

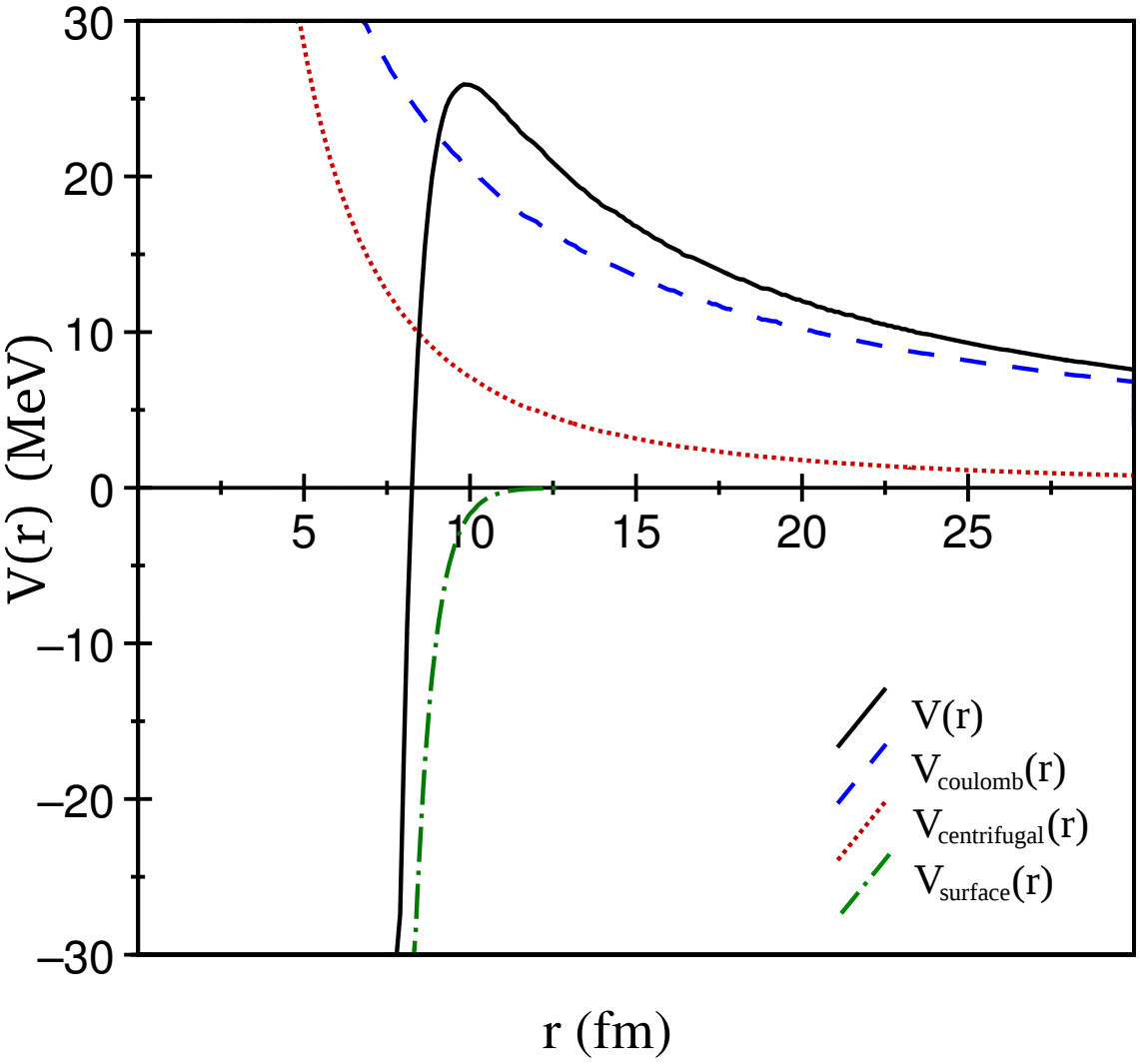


Figure 2.6: A potential barrier V(r) and its constituent components. These example potentials are calculated based on an $\alpha$ particle carrying 11 units of angular momentum from a $^{158}$Ta nucleus.

# Chapter 3

# Experimental Apparatus and Methodology

In order to successfully perform $\gamma$-ray spectroscopy on neutron-deficient nuclei a number of challenges must be met. The difficulties involved regarding the efficient detection of $\gamma$ rays are somewhat over-shadowed by the challenges introduced when synthesising and isolating nuclei of interest. Only when these challenges have been met can analytical techniques be applied for the purposes of furthering nuclear structure research. In this chapter, the experimental apparatus and techniques used to meet these challenges are described with the purpose of providing the relevant experimental background for the analysis that follows.

## 3.1 Heavy-ion fusion evaporation reactions

The study of nuclear structure at the extremes of neutron deficiency requires that nuclei be synthesised artificially. The production of neutron-deficient nuclei can be achieved using fusion evaporation reactions in which a beam of accelerated nuclei is projected onto a fixed target. Collisions between beam and target nuclei may

result in their fusion into a compound nucleus. As the line of nuclear stability falls below the $Z = N$ line, with increasing mass, the fusion of two stable nuclei will usually result in the production of a compound nucleus deficient in neutrons. Such compound nuclei are particularly unstable systems as they are highly excited and carry a large amounts of angular momentum.

Particle evaporation enables the compound nucleus to lose energy and will de-excite the system to within a fraction of the proton and neutron separation energies of the yrast line. Any further particle emission would result in the yrast line being crossed. The yrast line, shown in Figure 3.1, occurs when the maximum angular momentum has been achieved for a given excitation energy (hence the use of the Swedish word "yrast", whose literal meaning is "dizziest") and so states cannot exist below this line. A consequence for fusion evaporation reactions is that once within a fraction of the proton and neutron separation energies of the yrast line, particle emission is no longer a valid mode of de-excitation.

At this stage the nucleus is considered to be an evaporation residue. The product has been synthesised and is highly excited with a large angular momentum. The reaction exit channels depend very much on the amount of energy and angular momentum the compound nucleus has upon formation as they define its proximity to the yrast line, determining the amount of particle evaporation possible. As such, a single choice of beam and target can produce a variety of reaction channels, some of which may be populated preferentially with an appropriate choice of beam energy.

The emission of $\gamma$ rays enables energy and angular momentum to be transferred away from the nucleus, which enables it to draw closer in energy to the yrast line. Initially, $\gamma$-ray emissions are statistical, that is, the density of states is high and the resulting transitions do not form resolvable peaks. The emission of statistical transitions brings the evaporation residue close to the yrast line.

Cascades of $\gamma$-rays transitions along the yrast line allow for further removal of

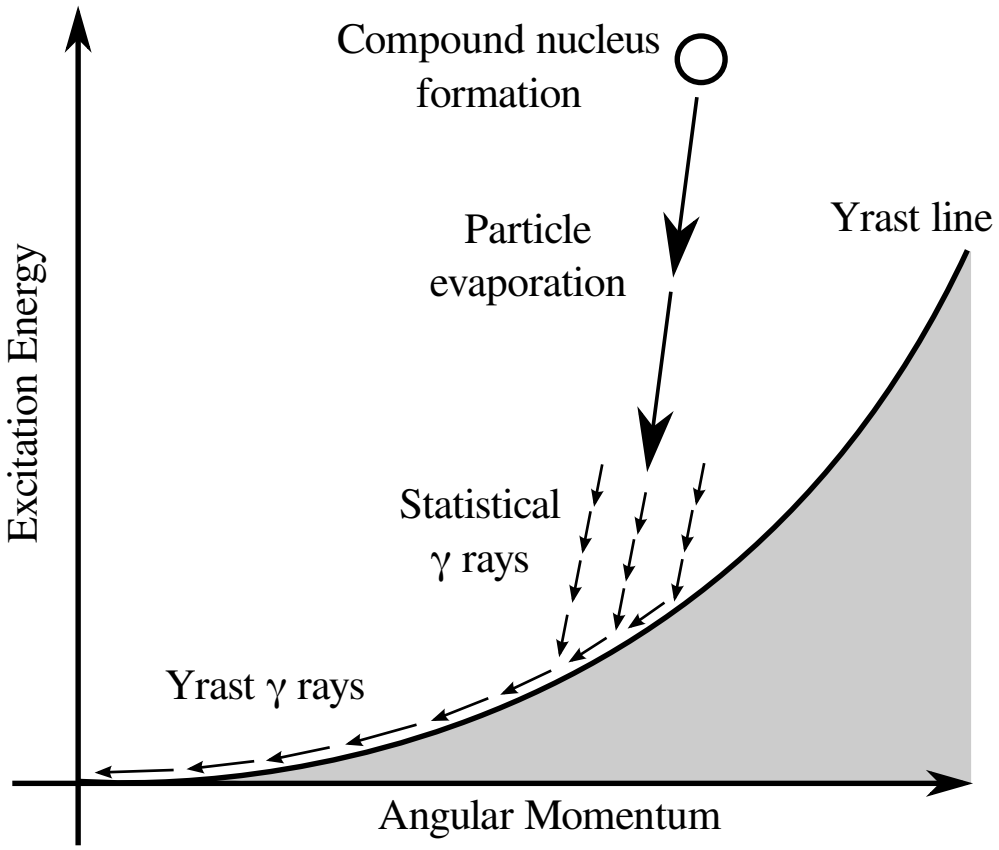


Figure 3.1: Representation of the de-excitation of the compound nucleus in a heavy-ion fusion evaporation reaction. Particle emission carries energy from the nucleus until the evaporation residue is within the proton and neutron separation energies of the yrast line. Statistical $\gamma$ rays continue to de-excite the nucleus towards the yrast line. Cascade of $\gamma$-ray transitions between states close to the yrast line further de-excite the nucleus.

energy and angular momentum from the system. Unlike statistical $\gamma$ rays, these transitions can be resolved due to the rather limited availability of states close to the yrast line. As the emission of $\gamma$ rays is a response to the changing structure of the nucleus, yrast cascades provide an opportunity to observe a variety of nuclear structure phenomena.

## 3.2 Challenges for spectroscopy

Fusion evaporation reactions make it possible to synthesise neutron-deficient nuclei in excited states close to the proton drip line, however, a number of challenges must be addressed before $\gamma$-ray spectroscopy can be performed effectively.

The probability of fission following the fusion of beam and target nuclei is significant in heavy neutron-deficient nuclei. This introduces a large $\gamma$-ray background, which obscures $\gamma$-ray transitions from the desired reaction channels. Competing reaction channels will also introduce a source of background, as does Coulomb excitation of the target material by the beam, which further obscure the transitions originating from a particular channel of interest.

While production of nuclei close to the proton drip line can be achieved, the large background contributions prevent the study of nuclei with the lowest cross-sections and so the suppression of the $\gamma$-ray background is of great importance. These challenges can be met by coupling a $\gamma$-ray spectrometer to a recoil separator with a focal plane detection system and utilising selective tagging techniques.

A spectrometer at the target position is required to detect emitted $\gamma$-ray transitions, however, as previously stated, the background contributions will be very high. The use of a recoil separator to suppress fission products and unreacted beam makes recoil-$\gamma$ correlations, between spectrometers at the focal plane of the separator and at the target position, possible. Recoil-$\gamma$ correlations are dependant on temporal relationships and require that data from each detector be stored with an associated time stamp.

Recoil-$\gamma$ correlations enable the contributions from fission and Coulomb excitation to be suppressed, however, the background that arises from the range of possible reaction channels is still present and, for weaker reaction channels, $\gamma$-ray transitions may still be obscured. To distinguish between these reaction channels, the Recoil

Decay Tagging (RDT) technique [16] is employed, which identifies nuclei by their characteristic radioactive decays. Decays are correlated spatially and temporally with the mother nuclei and conditions are placed on the energy and half-life characteristics to complete the identification process. RDT correlations ensure that $\gamma$ rays that are not accompanied by appropriate signals are discarded.

## 3.3 Experimental Apparatus

Efficient high-resolution spectroscopy is of tremendous importance when studying the structure of the nucleus, however, the large $\gamma$-ray background associated with fusion evaporation reactions presents a far more immediate problem. High-resolution spectroscopy is of limited use if the $\gamma$-ray emissions of interest cannot be separated from the background. The experimental apparatus at the Accelerator Laboratory at the University of Jyväskylä can be used in conjunction with selective tagging techniques in order to suppress this large $\gamma$-ray background and obtain relevant nuclear structure information.

The apparatus used at the University of Jyväskylä will be described with reference to the requirements that must be met to enable the techniques performed in this work.

### 3.3.1 The Jurogam spectrometer

The hyper-pure germanium (HPGe) detector array JUROGAM [17, 18], shown in Figure 3.2, is the primary tool for performing $\gamma$-ray spectroscopy in this work. The JUROGAM spectrometer comprises 43 HPGe detectors, with an energy resolution of $\sim$1.9 keV at 356 keV, focused on a single target position and covering a large solid angle to optimise efficiency. Detectors are arranged in a "honeycomb" pattern and are tapered at the ends, which enables them to tessellate, leaving as little solid angle

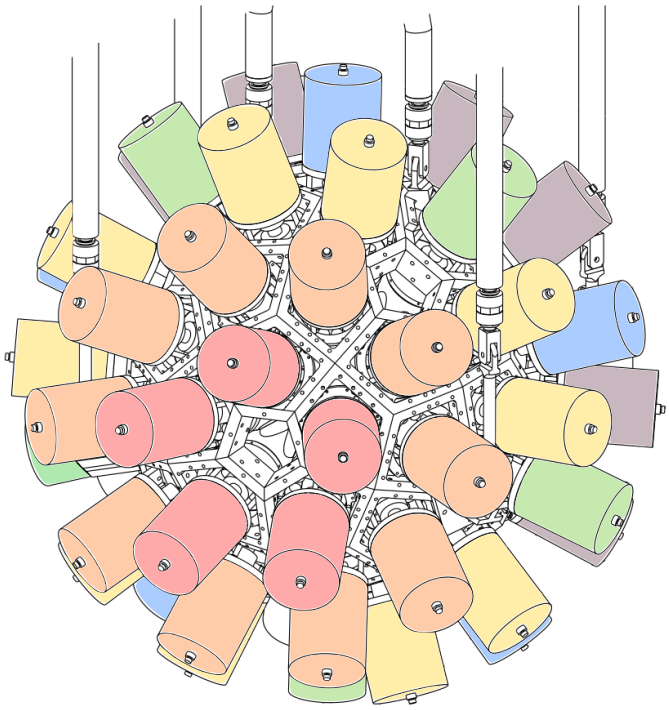

Figure 3.2: Schematic diagram of the JUROGAM array [19]. Detectors arranged in rings at six different angles from the beam direction are distinguished by colour.

uncovered as possible.

Each detector is equipped with a Compton-suppression shield of bismuth germanate (BGO) [20]. Signals in a detector that are in coincidence with a signal in the BGO shield are discarded as they correspond to $\gamma$ rays that have Compton scattered out of the detector and have not deposited their full energy into the Ge crystal. Heavy-metal collimators shield the front faces of the BGO scintillators in order to prevent transitions that are completely absorbed in the germanium crystal from being discarded due to coincidences with separate $\gamma$ rays entering the BGO shields directly.

The relative energy efficiency of the Jurogam array is shown in Figure 3.3. It is at its most efficient at ~200 keV. The JUROGAM spectrometer is used to perform coincidence analysis on high multiplicity events. The number of detected $\gamma$ rays per

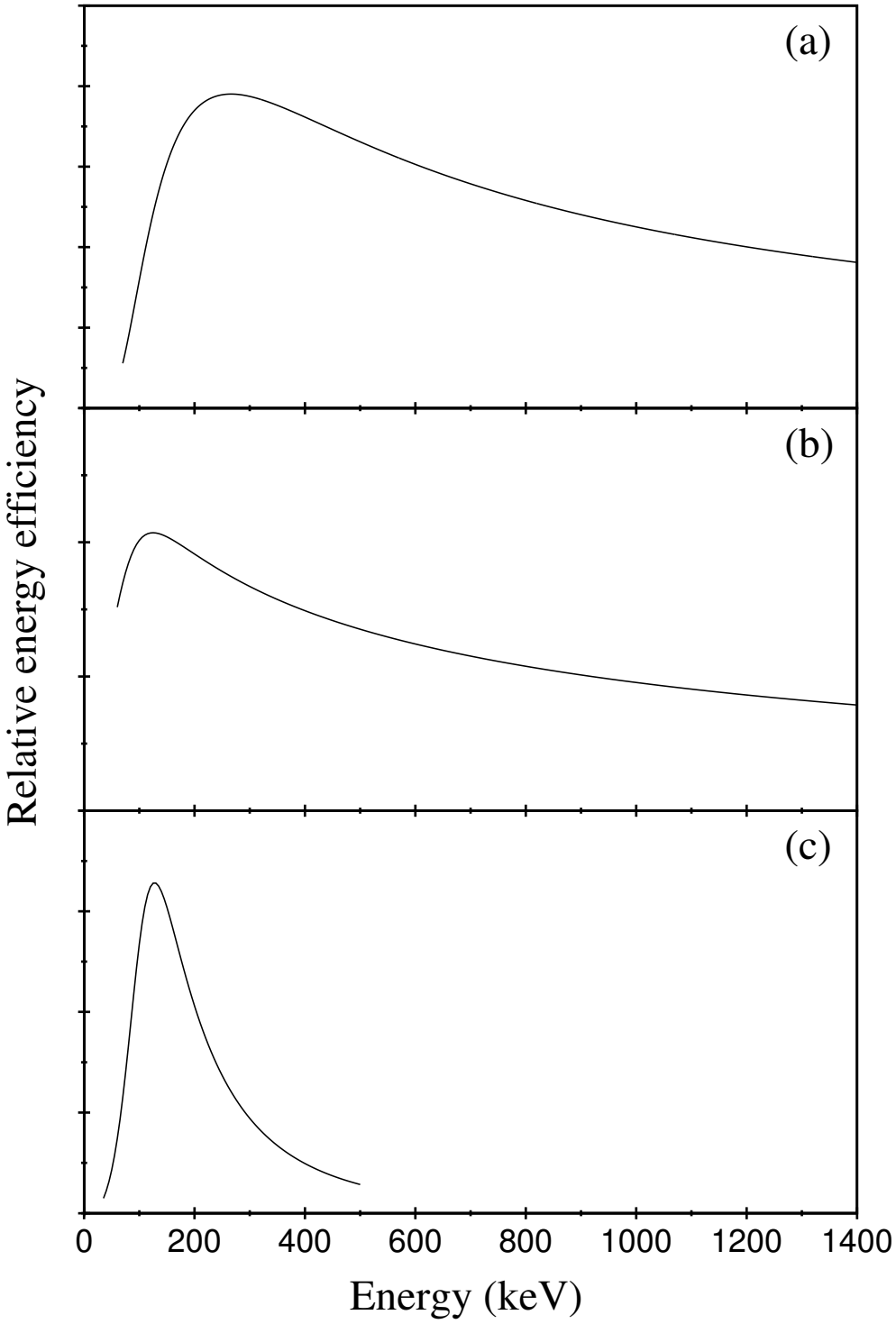


Figure 3.3: Relative energy efficiency curves for the germanium detectors used in this work. Relative efficiency scales are linear, starting at zero. Relative efficiencies for **(a)** the Jurogam spectrometer, **(b)** the focal plane clover detector and **(c)** the focal plane planar detector have been obtained using a compound $^{152}$Eu$^{133}$Ba source.

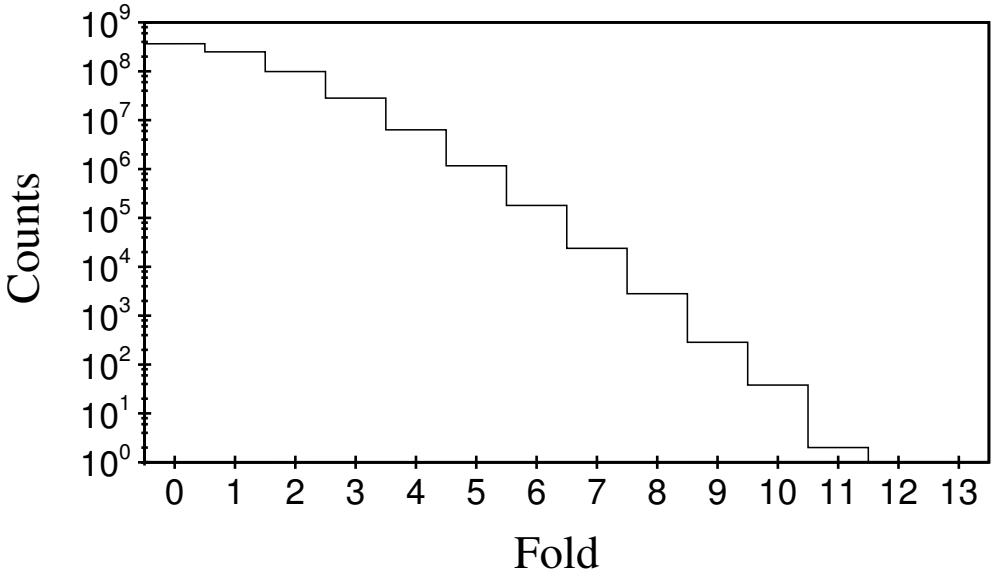


Figure 3.4: Recoil gated fold detected by JUROGAM during a fusion evaporation reaction in which a $^{58}$Ni beam is incident on a $^{102}$Pd target with a beam energy of 255 MeV.

event, the fold, for JUROGAM is shown in Figure 3.4.

### 3.3.2 The RITU separator (Recoil Ion Transport Unit)

The RITU separator [21] is used to separate fusion evaporation residues (recoils) from unreacted beam and fission fragments and transport them to a spectrometer at the focal plane for identification.

RITU, illustrated in Figure 3.5, is operated as a gas-filled separator for the purpose of efficient transmission of recoils to the focal plane while suppressing transmission of unreacted beam and fission fragments. Recoils leaving JUROGAM do so at a range of angles from the beam axis, due to particle evaporation and scattering within the target, forming a narrow conical shape. A quadrupole magnet at the entrance of RITU focuses these recoils vertically, reducing the width of the cone and improving the acceptance to the dipole magnet. Fission fragments leave JUROGAM in a significantly wider cone and are effectively removed by this first quadrupole

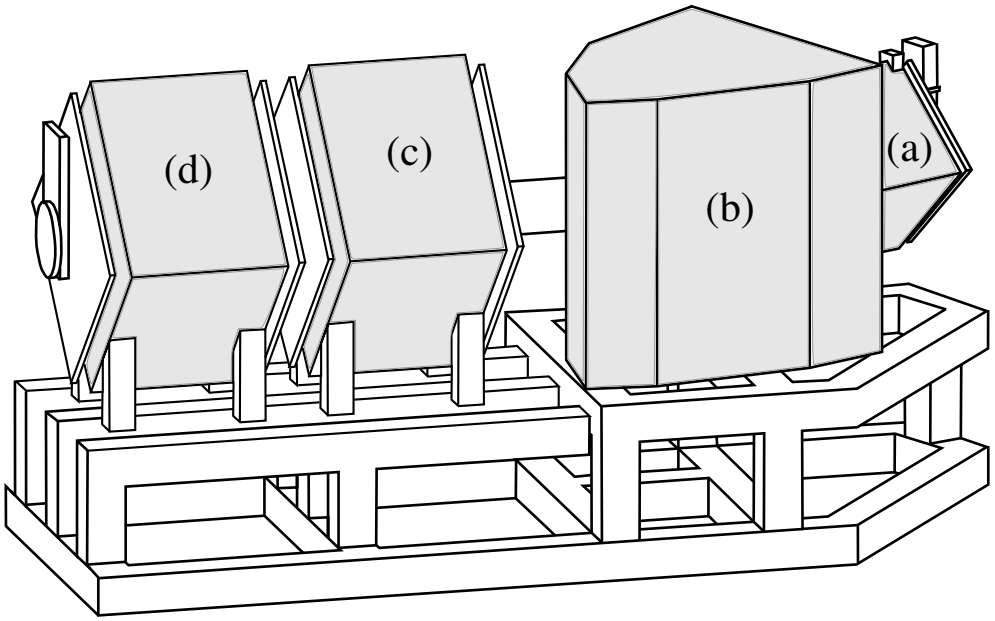


Figure 3.5: Schematic diagram of the RITU gas-filled separator [19]. Recoils exit JUROGAM and are vertically focused by the quadrupole magnet at **(a)** matching the recoil cone to the acceptance of the dipole magnet. **(b)** The unreacted beam is suppressed when deflected by the dipole magnet at and recoils are focused horizontally at **(c)** and vertically at **(d)** by quadrupole magnets, for efficient transmission to the focal plane.

magnet.

Suppression of the unreacted beam is achieved by deflecting nuclei in a magnetic field produced by the dipole magnet. In a vacuum mode separator, the field produced by a dipole magnet will separate nuclei depending on their mass to charge ratio. Such a separation technique can be used for the identification of nuclei, but is inefficient, transporting only a fraction of the available reaction channels to the focal plane. RITU is a gas-filled separator, normally employing helium gas, and when beam and recoils are deflected in the magnetic field collisions with the gas cause them to scatter, removing their mass to charge ratio information. This enables far greater recoil transmission efficiency than a vacuum separator, at the expense of mass to charge ratio separation.

Separation between recoils and unreacted beam is dependant on the magnetic

rigidity,

$$B\rho = \frac{mv}{eq}, \tag{3.1}$$

which determines the deflection of a particle in a magnetic field. A further two quadrupole magnets are employed to focus the recoils and guide them to the focal plane detector.

### 3.3.3 The GREAT spectrometer (Gamma Recoil Electron Alpha Tagging)

The identification of nuclei following heavy-ion fusion evaporation using the RDT technique requires a spectrometer capable of detecting both the recoils and their subsequent radioactive decays. The GREAT spectrometer [22] is a diverse tool for performing spectroscopy at the focal plane of RITU. It is comprised of a number of detectors, which make it suitable for the detection of recoils, $\alpha$ decays, electrons, X-rays and $\gamma$-ray emissions.

Although different configurations are possible, in this work the GREAT spectrometer was comprised of five main detector components: the Multi-wire proportional counter (MWPC); the double-sided silicon strip detectors (DSSDs); the PIN diode array; the planar germanium detector; and the clover germanium detector. These components are shown in Figure 3.6.

The MWPC is a gas counter located at the entrance of the GREAT spectrometer. Recoils transported via RITU will pass through this detector, ionising the isobutane gas resulting in their detection. One of the primary roles of the MWPC is to enable distinctions to be made between DSSD events that originated from the target position and those that originated inside the GREAT spectrometer. It also serves to suppress scattered beam that reaches the focal plane. This will be described in more detail in Section 3.4.1.

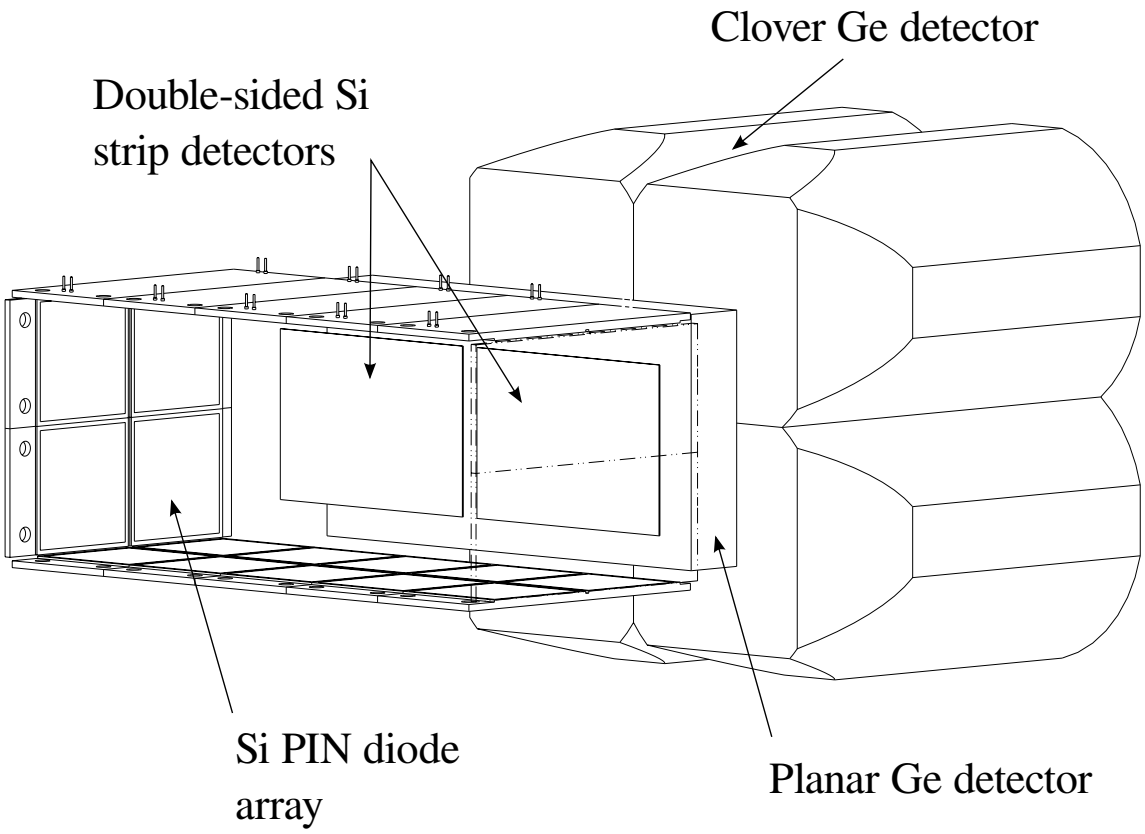


Figure 3.6: Main constituents of the GREAT spectrometer [22].

The DSSDs are a pair of silicon detectors, each of area 60 mm × 40 mm with a thickness of 300 $\mu$m and an energy resolution of ∼30 keV at 5730 keV, in which recoils become implanted. Charge collection is achieved using contacts arranged in strips vertically on the front face and horizontally on the back face of the silicon and the combination of signals in the front and back strips allow for the determination of the origin of the radiation within the DSSDs. With two detectors consisting of 40 × 60 strips, the DSSDs have 4800 pixels. This high level of pixelation allows accurate spatial correlations to be made between multiple DSSD events, enabling correlations at much higher implantation rates than would otherwise be possible.

The PIN diode array consists of 28 silicon detectors. Although capable of detecting conversion electrons and $\beta$ decays, $\alpha$ particles that escape the DSSDs can also be detected using this array. In the scenario that an $\alpha$ particle escapes the DSSDs and

is detected by the PIN diodes, the majority of the energy is shared between these detectors. This makes it possible to reconstruct the energy of an $\alpha$ decay, although energy losses between detectors limit the accuracy of such measurements.

The planar germanium detector, positioned behind the DSSDs, is most efficient for detecting X-rays and low-energy $\gamma$ rays. Like the DSSDs, signals in the planar detector are read from vertical and horizontal contact strips on the front and back of the detector. The lowest energy transitions do not penetrate very far into the germanium and will produce only small amounts of charge. As such, the strips on the front face of the detector are better suited to detecting X-rays and $\gamma$ rays of energy $E_\gamma < 100$ keV. The energy resolution is $\sim$2.1 keV from the front face and $\sim$2.4 keV from the back face of the planar detector at 80 keV.

The clover germanium detector is comprised of four separate HPGe crystals [22] and is accountable for $\gamma$-ray spectroscopy of isomer delayed transitions, capable of detecting transitions in the energy range $\sim$100-2000 keV. The energy resolution is $\sim$2.6 keV at 356 keV. The clover detector was positioned directly above the DSSDs providing a large surface area for the detection of $\gamma$-ray emissions originating from within the GREAT spectrometer.

Unlike the HPGe detectors at the target position, the focal plane clover is not equipped with a Compton suppression shield. Instead, transitions that have Compton scattered between the individual crystals can be added together to reconstruct the original energy of a $\gamma$-ray emission, rather than simply discarding the event. Although this procedure improves the peak-to-total ratio in the region $E < 500$ keV, as demonstrated in Figure 3.7, the total intensity of the majority of $\gamma$-ray peaks is not greatly affected. As such, the focal plane clover detector is suitable for coincidence analysis, as described in Section 3.4.6, by sacrificing the add-back procedure.

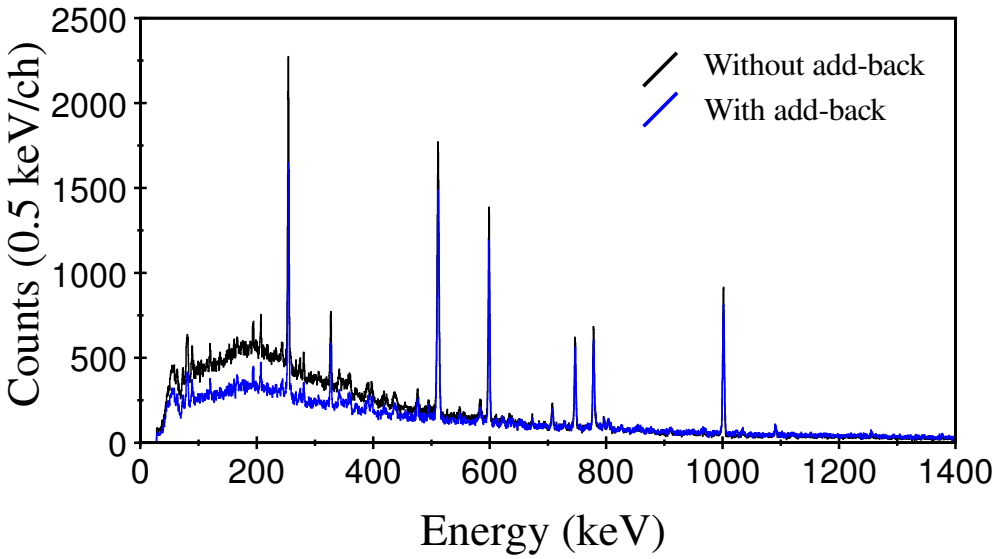


Figure 3.7: Energy spectrum of $\gamma$ rays detected in the focal plane clover detector. The peak-to-background ratio is significantly improved in the add-back (blue) spectrum for $E < 500$ keV in comparison to the spectrum without add-back (black).

### 3.3.4 Total Data Read-out (TDR)

Total Data Read-out (TDR) is a triggerless data acquisition system [23] that requires that events be built up in software [24] rather than following a hardware trigger. It is common in data acquisition to only collect signals from detectors for a period of time after a triggering condition has been passed. This incurs a system wide dead time in which further events may be missed. When the triggering rates are low or when the desired events are frequent compared to background events this is an effective method of data acquisition. However, when triggering rates are high or when the desired events are infrequent in comparison with background such a system will serve to miss useful data.

The TDR system combats this by reading from all detectors individually with no requirement of a triggering condition. Each signal is then assigned a time stamp determined by a system wide clock to a precision of 10 ns. This eliminates common dead time.

Events are built in software and correlations can be made with a software trigger. An inherent advantage of this is that observations may be made prior to a triggering event with ease, and correlations can be made over relatively long time periods without missing events that may have occurred during this time. This is a necessity for the RDT technique, in which it shall be seen that the $\gamma$-ray data, which is of interest, precedes the triggering conditions by several milliseconds.

Collecting and storing all data output over the course of an experiment would incur large amounts of stored data, much of which is of little use or interest. In order to limit the amount of unwanted data stored a pre-filter is employed decide which data to store. In this work the pre-filter only stored data that could be correlated with an event in the DSSDs. As such, when performing offline analysis all correlations must be made relative to events in the DSSDs.

## 3.4 Experimental Techniques

The data provided by the apparatus described in the previous section allows for a range of experimental techniques to be utilised. Such techniques are necessary in order for data associated with the desired reaction channel to be identified.

### 3.4.1 The Recoil Decay Tagging (RDT) Technique

The use of heavy-ion fusion evaporation reactions enables the synthesis of neutron-deficient nuclei, however, an inherent feature of this process is a range of possible reaction channels, which contribute to a rather large $\gamma$-ray background. The Recoil Decay Tagging (RDT) technique [16] is a means of identifying a specific reaction channel by requiring that the measured decay properties of an evaporation residue conform to the characteristic energy and decay time of the nucleus of interest.

The basic operation of the RDT technique, as illustrated in Figure 3.8, is to

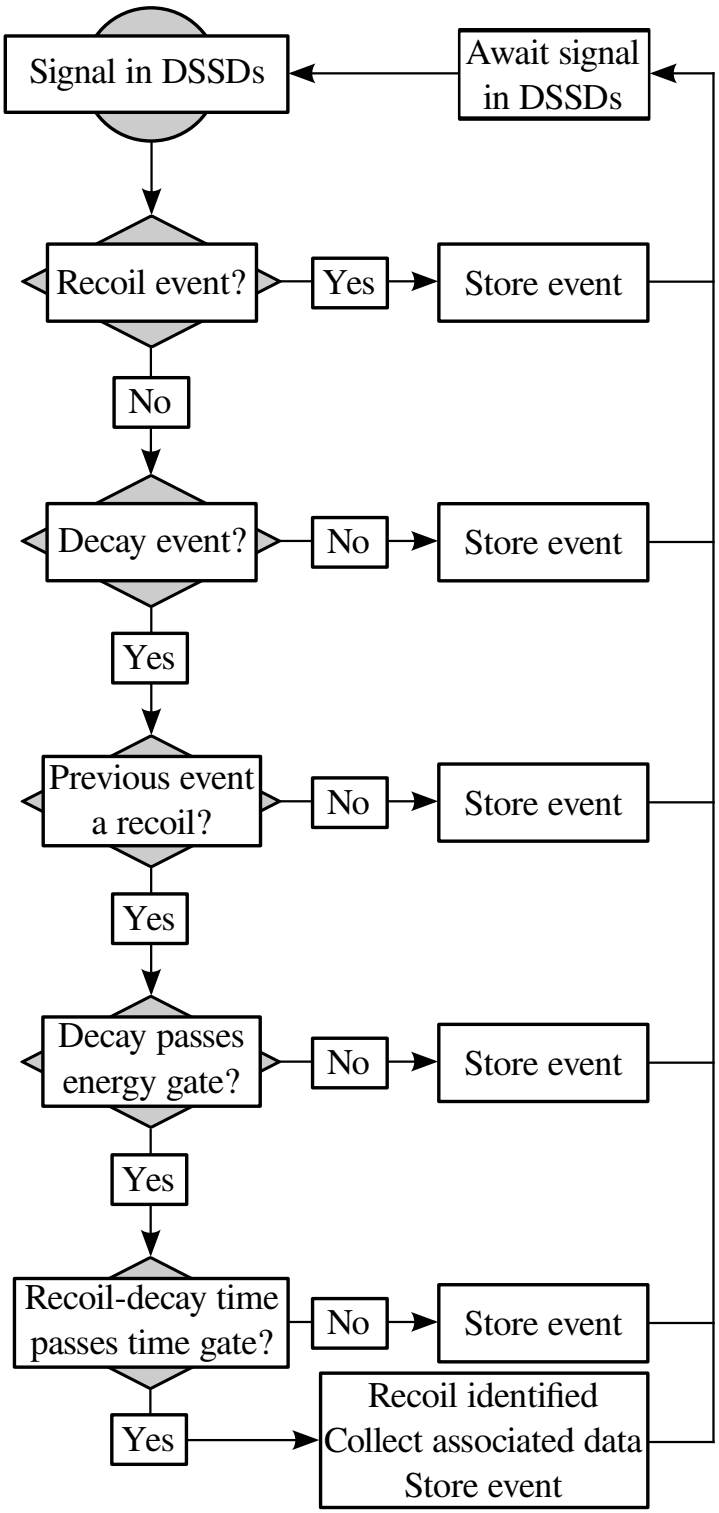


Figure 3.8: Flowchart illustrating the basic operation of the RDT technique. Stored events are placed in the tagger, as illustrated in Figure 3.10.

process signals in the DSSDs to distinguish between recoil and decay events, check whether decay events are preceded by recoil and to determine whether the energy and decay time properties of the decay match those of the desired nucleus. Once a decay has passed these conditions, the corresponding recoil is considered to have been identified and so correlations with signals in other detectors can be made.

In order to distinguish between recoil and decay events each is assigned an experimental definition. As recoil events are transported to the DSSDs via the RITU separator, they must pass through the MWPC before becoming implanted in the DSSDs. While a recoil event would result in an MWPC signal accompanying the signal in the DSSDs, the same is true of any remnants of the beam that have eluded the separation process. In order to ensure that unreacted beam is not treated as a recoil, further distinctions must be made between DSSD signals accompanied by an MWPC signal. Differences in the charge and velocity of the unreacted beam and recoils enable these distinctions to be made.

The greater charge carried by recoils causes more ionisation in the MWPC than scattered beam. Furthermore, the velocity of the unreacted beam is generally greater than that of recoils and so the time between signals in the MWPC and DSSDs will differ. The separation of unreacted beam from the DSSD signals is demonstrated in Figure 3.9. By demanding that events pass a 2-dimensional gating condition, encompassing the time-of-flight (TOF) between the MWPC and the DSSD and the deposited energy in the MWPC corresponding to recoil events, scattered beam can be distinguished from recoils.

Decays are more simply defined as events that are not accompanied by a signal in the MWPC as they originate from recoils that have already entered the GREAT spectrometer. Recoil and decay events can been identified a treated separately using these definitions.

The processing of DSSD events, as shown in Figure 3.8, requires that they be

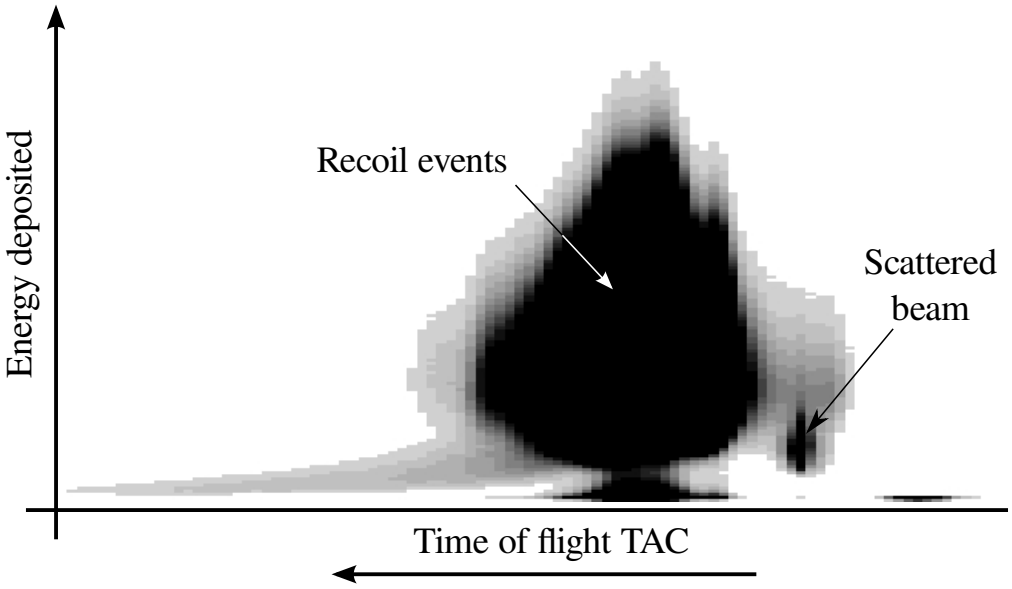


Figure 3.9: Energy deposited in the MWPC against the flight time between the MWPC and the DSSDs. Scattered beam and recoiling evaporation residues can be distinguished by differences between the amount of energy they deposit and their flight times.

stored for ease of correlation. This is achieved in software using a "tagger", Figure 3.10, which is a 3-dimensional array in which two of the dimensions correspond to DSSD pixel coordinates and the length of the third dimension is based on time. When an event occurs, it is stored in an element of the tagger that corresponds to that pixel. This event will be stored until a pre-specified time has passed. Further events detected in a pixel will be stored in the tagger in addition to those already stored and when a decay event is detected previous events from that pixel are readily available for correlation. As events from different pixels are stored separately, spatial correlations between events are inherent, and as all events carry a time stamp, temporal correlations are very simple. The operation of the tagger is shown in Figure 3.10.

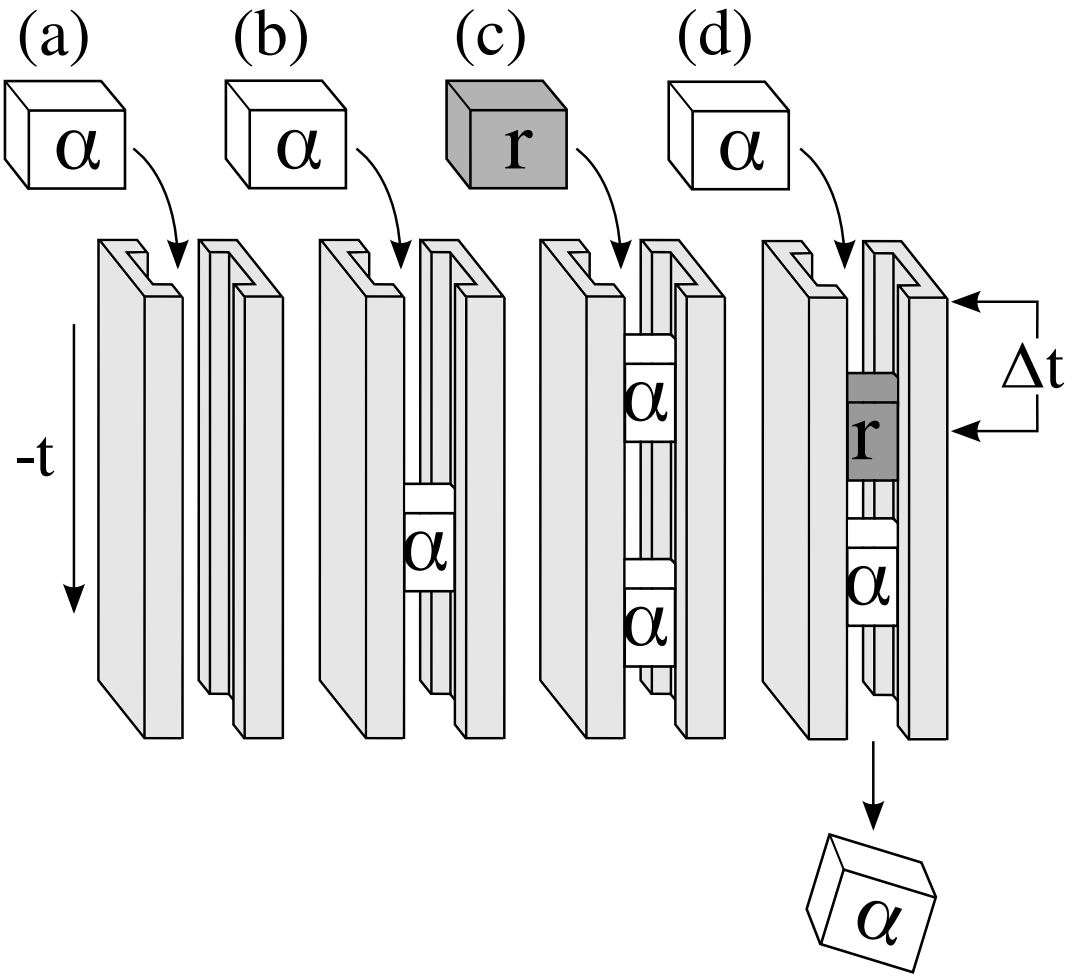


Figure 3.10: The storing and correlation of events in one DSSD pixel, using the tagger, is represented by this figure. The tagger stores DSSD events for a pre-specified period of time during which correlations between events can be made. **(a)** A decay event is detected and stored, as directed by the procedure illustrated in Figure 3.8, by being placed in the tagger. **(b)** Another decay event is detected. As the previous event was not a recoil, it is only stored. **(c)** A recoil event is detected and stored. **(d)** A decay event is detected. As the previous event was a recoil, energy and time gates are applied before storing the event. After the pre-specified storage time runs out, events are discarded.

### 3.4.2 Gamma-ray correlations

A practical purpose for the RDT technique is the correlation of data associated with a particular reaction channel. Gamma-ray data collected by JUROGAM and GREAT for a specific reaction channel can be obtained using temporal correlations with the

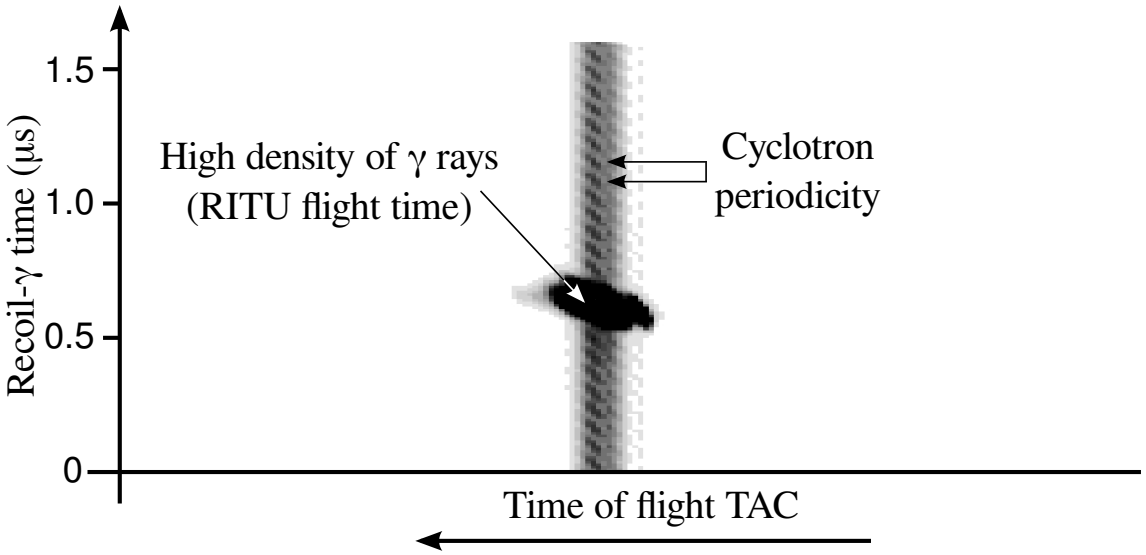


Figure 3.11: Recoil-$\gamma$ time difference against the flight time between the MWPC and the DSSDs. At the average recoil-$\gamma$ time difference a high density of $\gamma$ rays collects corresponding to the RITU flight time. The regular dark patches indicate the cyclotron frequency, where there is a higher probability of a reaction resulting in the detection of a greater number of $\gamma$ rays.

identified recoil and decay events.

As the periodicity of the cyclotron is significantly lower than the RITU flight time, $\sim$70 ns and $\sim$0.5 $\mu$s respectively, many fusion evaporation reactions may take place at the target position in the time it takes a recoil to reach the focal plane thereby introducing a large $\gamma$-ray background.

The correlation of recoil events with $\gamma$-ray emissions at the target position can be achieved by taking account of the flight time of a recoil through the RITU separator and ignoring data that deviate from this flight time. An average flight time through RITU can be obtained by plotting the time difference between DSSD recoil events and JUROGAM data. Although this will cover a broad range of time differences, over a large number of events a peak will build at the average flight time due to the increased probability of transitions being observed at that time difference. This is shown in Figure 3.11. This demonstrates the power of building

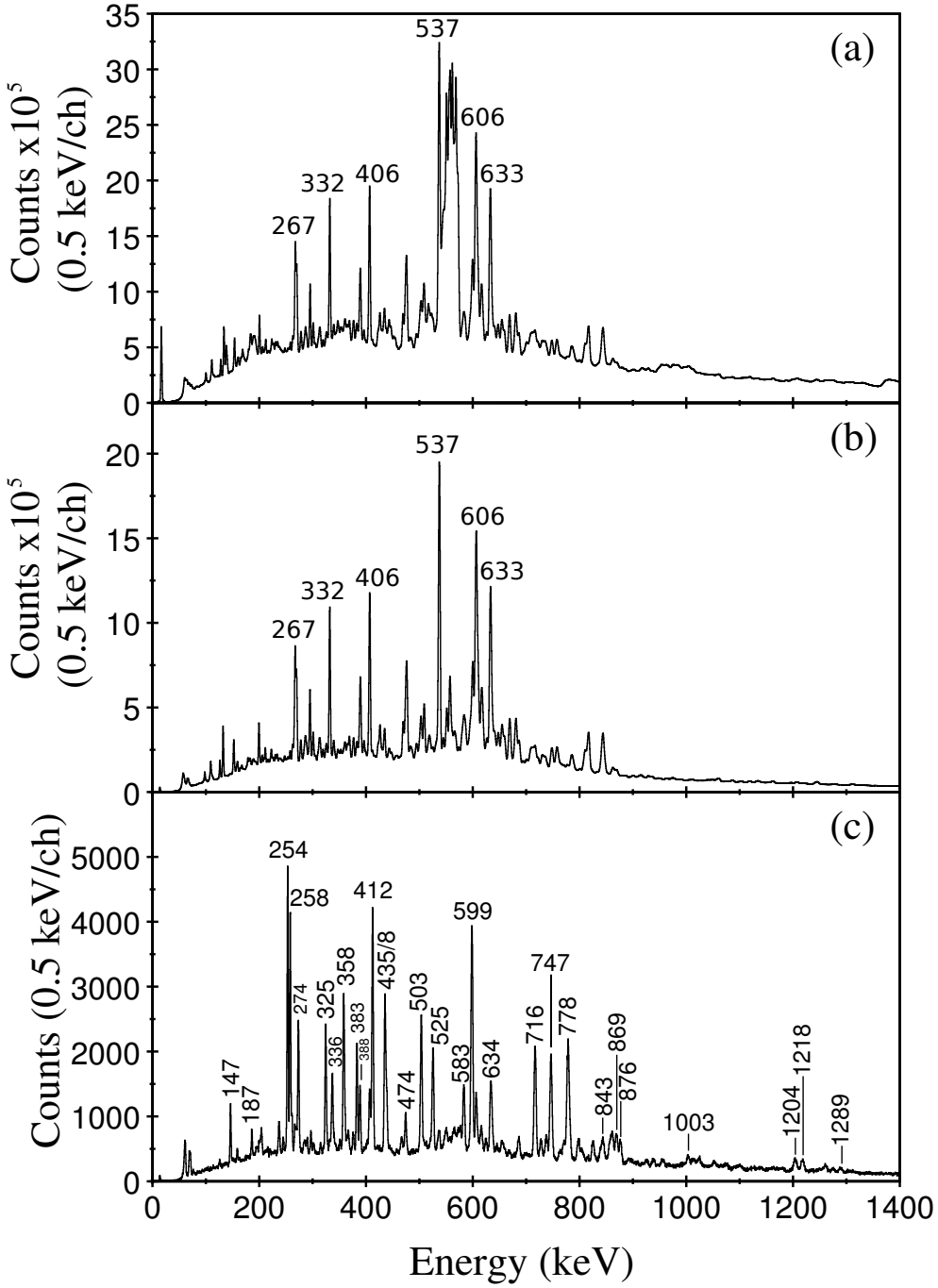


Figure 3.12: Gamma-ray spectra from JUROGAM. **(a)** Pre-filtered spectrum containing all $\gamma$-ray data in JUROGAM corresponding to any focal plane signal. Emissions from the strongest reaction channels are visible as is the de-excitation of the target material. Labelled peaks belong to the strongest fusion evaporation channel, $^{157}$Lu. **(b)** Recoil gated spectrum. Target de-excitation events have been suppressed. **(c)** RDT spectrum using the $^{158m1}$Ta $\alpha$ decay as a tag. The strongest channels have been suppressed revealing transitions in $^{158}$Ta, whose energies are labelled.

events in software using the triggerless TDR system as sorting data once will enable an average RITU flight time to be obtained and this can be used in subsequent sorts to correlate identified recoils in delayed coincidence with $\gamma$ rays. The effects of correlating identified recoils with $\gamma$-ray data is shown in Figure 3.12.

As recoils can be correlated with $\gamma$ rays detected by JUROGAM, so too can they be correlated with $\gamma$ rays detected by the GREAT spectrometer. The requirements for correlations at the focal plane differ to those at the target position as instead of an average flight time there is only the decay time to consider. As such, focal plane $\gamma$ rays are collected if they occur within a specified time of a DSSD event.

A major limitation to the RDT technique is the decay time of the nucleus. Significant losses will occur for nuclei with short half-lives, less than $\sim$0.5 $\mu$s, as they will often decay before reaching the focal plane spectrometer, preventing the identification of the nucleus using its characteristic decay. Identification of nuclei with longer half lives, $\sim$100 ms or more, can also be problematic if the recoil rates at the focal plane are high. The longer the decay time and the higher the recoil rate, the more likely it is for miscorrelations to occur. This is described in more detail in Section 3.4.7. Further limitations for the RDT technique are nuclei with low $\alpha$-decay branching ratios.

Where the RDT technique is applicable it is possible to perform $\gamma$-ray spectroscopy despite relatively low production cross sections and large $\gamma$-ray backgrounds incurred in these reactions.

### 3.4.3 Recapturing escaped $\alpha$ decays for tagging

Following the decay of an implanted recoil, it is possible for $\alpha$ particles to escape from the DSSDs having deposited only a fraction of their energy. In such a scenario the energy deposited would not pass the selection criteria for RDT and the data associated with the event would be lost.

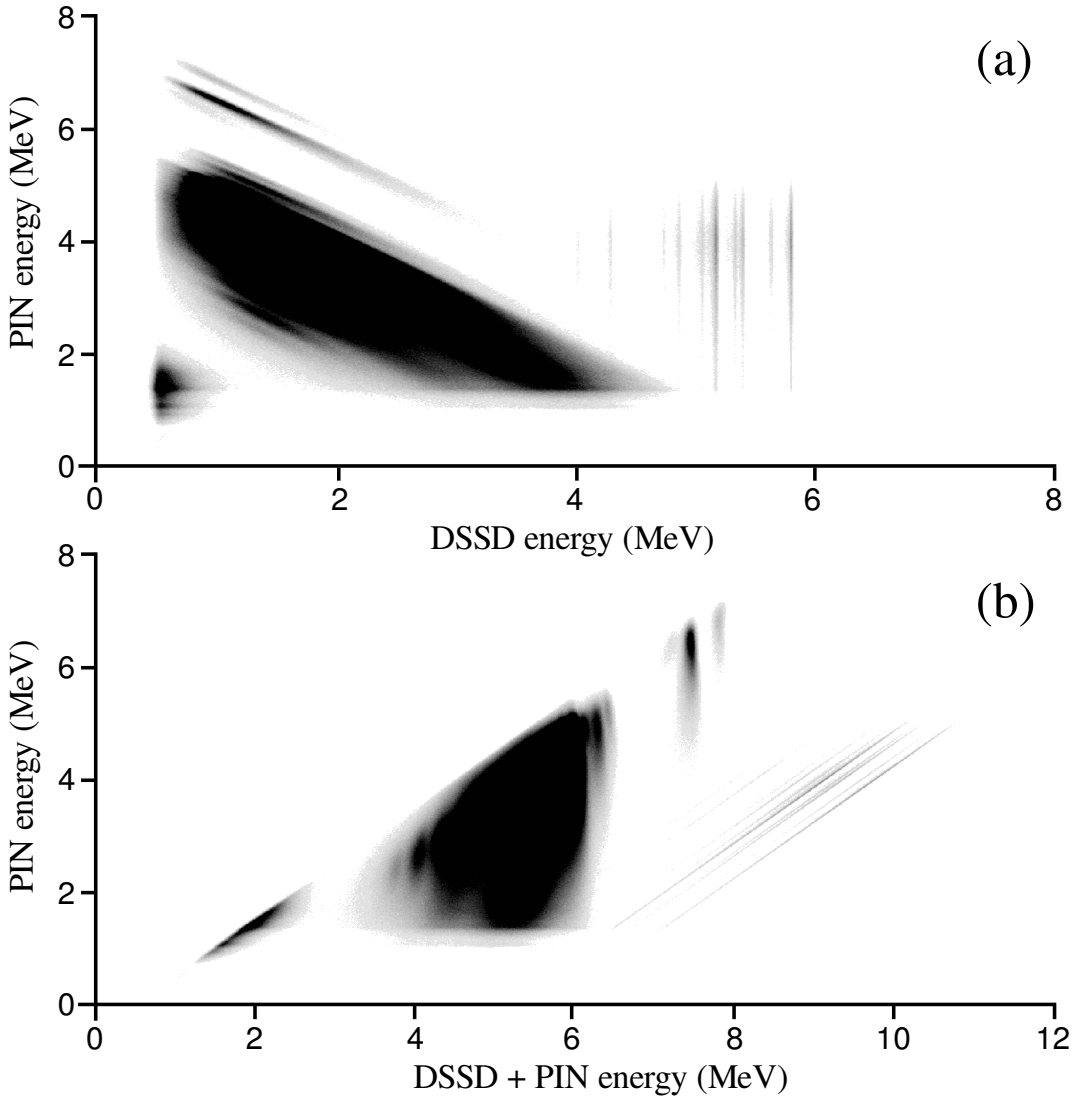


Figure 3.13: **(a)** Energy deposited in the DSSDs against energy deposited in the PIN diodes. Downward sloping clusters correspond to $\alpha$ decays that have escaped the DSSDs and deposited some of their remaining energy in the PIN diode array. These features can be used for recoil identification. Vertically arranged clusters indicate coincidences between random signals in the PIN diodes and DSSD signals corresponding to $\alpha$ decays that have deposited their full energy. **(b)** DSSD + PIN diode energy (partially reconstructed $\alpha$ particle energy) against energy deposited in the PIN diodes.

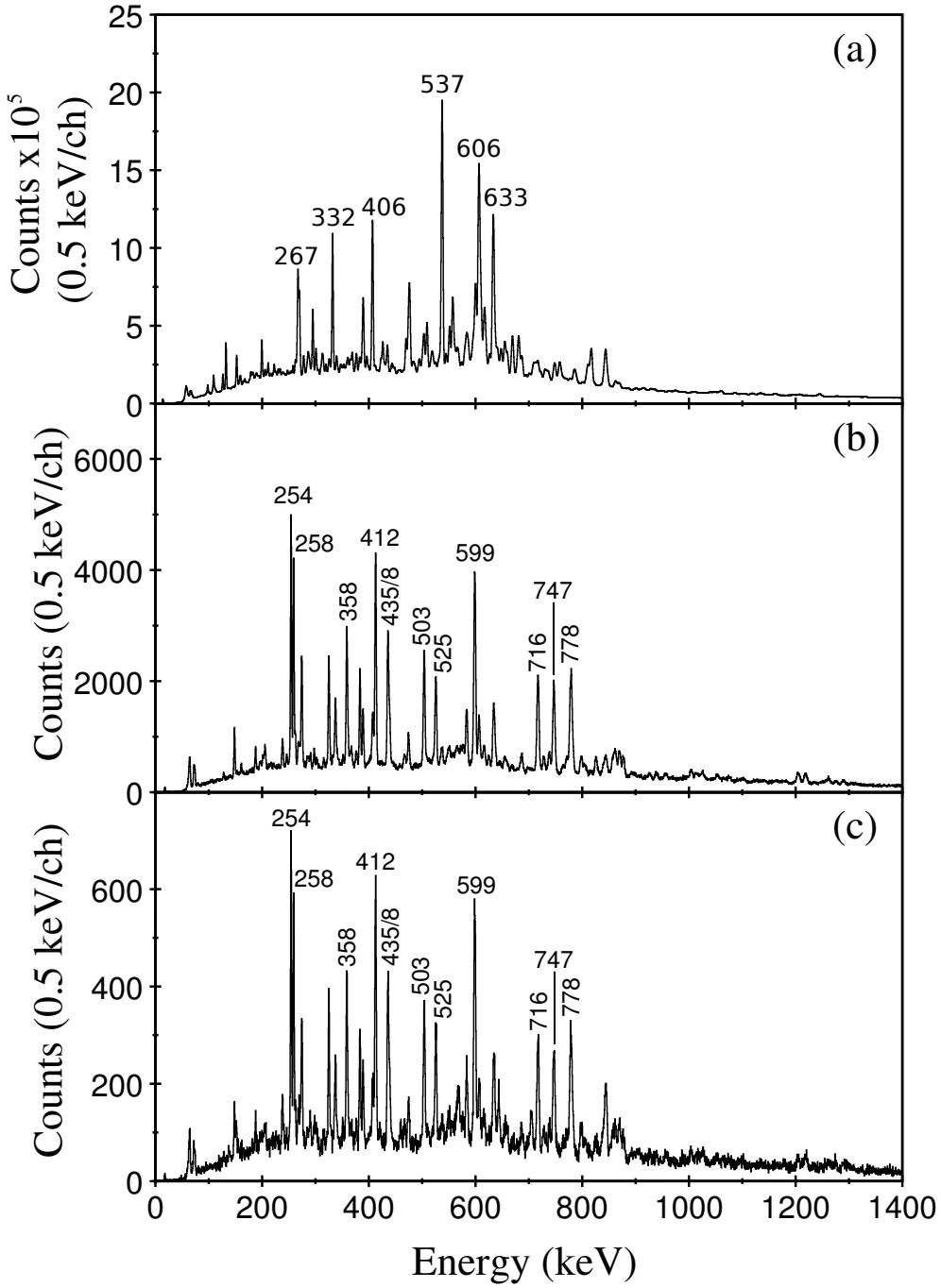


Figure 3.14: Energy spectra of $\gamma$ rays in JUROGAM. **(a)** Recoil gated. **(b)** Tagged using $^{158m1}$Ta $\alpha$ decays (6046 keV) in the DSSDs with a 175 ms correlation time. **(c)** Tagged using recaptured $^{158m1}$Ta $\alpha$ decays with a 175 ms correlation time. The features are similar to those in (b).

A number of these $\alpha$ particles will deposit their remaining energy in the PIN diodes, presenting an opportunity to recapture these events. The energy deposited in the PIN diodes is inversely proportional to the energy deposited in the DSSDs, as shown in Figure 3.13, although some consideration for energy losses between detectors must be made and, as such, decays cannot be expected to pass the original energy conditions by simply adding the DSSD and PIN diode energies together.

While the full energies of the $\alpha$ particles cannot be reliably reconstructed, features corresponding to specific decays can be distinguished and used as a selective tag. A comparison of a spectrum of $\alpha$ decays in the DSSD with the reconstructed energies enables these features to be identified, thus escaped $\alpha$ decays can be recaptured.

A 1-dimensional energy condition around the reconstructed energies would address the issue of energy loss between detectors, however, such a condition would also include a number of DSSD events coincident with random PIN diode signals. This can be addressed by employing a 2-dimensional gate around the reconstructed energies and the energy deposited in the PIN diodes, cutting off the energy region in which $\alpha$ decays deposit their full energy in the DSSDs.

Using recaptured $\alpha$ particles for RDT makes it possible to increase the number of $\gamma$-ray correlations. This is demonstrated in Figure 3.14, which shows that this technique can be used to obtain further $\gamma$-ray data in addition to data obtained by tagging on full energy peaks in the DSSDs.

### 3.4.4 Calibrations

The output of all detectors in this work is a voltage proportional to the collected charge and thus the deposited energy. The spectroscopy of all detected radiation is reliant on the ability to convert this electrical output into a corresponding energy. Differences between the bias voltages of different detectors, combined with variations

in detector crystals and radiation damage ensure that a signal from a detector has limited meaning without calibration. The most practical method of obtaining an accurate voltage to energy conversion is to regularly calibrate detectors using known sources of radiation as a reference.

The two most common methods of obtaining such a calibration using this experimental set up are done using either known stationary sources to perform an external calibration or decays from known reaction products to perform an internal calibration. In both cases, data from the calibration sources are collected and the detector outputs are compared with the known energies. Fitting a function to this comparison, for each detector output, enables conversion from output voltage to energy to be accomplished in software.

At the Accelerator Laboratory at the University of Jyväskylä, a compound $^{152}$Eu$^{133}$Ba source is the most commonly used stationary external source of $\gamma$ rays and is suitable for calibration of the JUROGAM array and the focal plane germanium detectors. The $^{152}$Eu nuclei $\beta$-decay to excited states in $^{152}$Sm and $^{152}$Gd [25]. Subsequent $\gamma$-ray emissions cover an energy range of 122-1408 keV. The $^{133}$Ba nuclei $\beta$-decay to excited states in $^{133}$Cs [26]. The range of energies is 80-384 keV, narrower than the $^{152}$Eu contribution, however this particular range is a region of large variation in the energy efficiency of the JUROGAM and Clover germanium detectors and so additional data points in this region are important. In practice, JUROGAM detects $\gamma$-ray emissions from moving sources and so requires a Doppler correction, as described in Section 3.4.5, in addition to the external calibration.

The silicon detectors at the focal plane can not be accurately calibrated using an external source as there are significant decay energy losses in the dead layer of the detector. Furthermore, the range of calibration energies available from an external source is very narrow and considerably lower than required for an accurate calibration of the region of interest.

Instead, an internal calibration of the DSSDs can be achieved using known radioactive decays of implanted nuclei. Reaction products created at the target position will be deflected in RITU and become implanted in the DSSDs. When these nuclei decay, the whole process occurs inside the detector, from emission to total absorption, under conditions identical to those of the experiment.

In some cases, a number of reaction products of the beam and target from the experiment are known and can be used for calibration. In the scenario that peaks of known energies cannot be unambiguously identified, their identity can be confirmed using the RDT technique if the associated $\gamma$-ray emissions are known.

### 3.4.5 Doppler-shift correction

The reaction products of fusion-evaporation reactions are not created at rest. As such, $\gamma$ rays detected at the target position are emitted from a moving source, which Doppler shifts their energies. Those $\gamma$ rays that are emitted in the forward direction, with an angular range of $0^o \leq \theta < 90^o$, will experience an increase in energy whilst those emitted in the backward direction, $90^o < \theta \leq 180^o$, will experience a decrease in energy. In order to account for these shifts in energy the Doppler correction,

$$E = E_0 \left(1 + \frac{v}{c} cos\left(\theta\right)\right), \tag{3.2}$$

must be applied, where $E$ is the detected energy, $E_0$ is the true energy, $v/c$ is the velocity of the nucleus and $\theta$ is the angle of the detector relative to the beam axis. The $v/c$ parameter can be calculated using known true energies of transitions and comparing them the those detected at different angles in JUROGAM. The effect of this correction is illustrated in Figure 3.15.

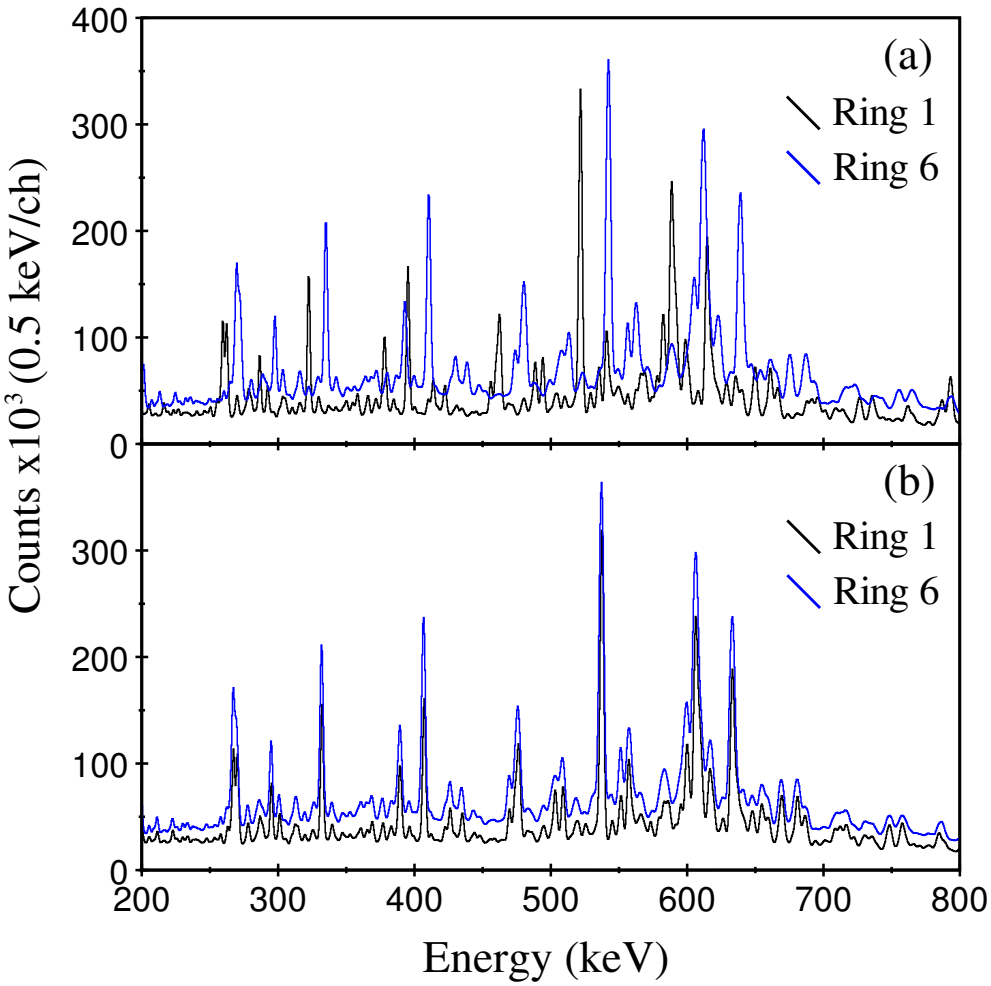


Figure 3.15: Recoil gated JUROGAM spectrum. The recoil velocity $v/c = 0.032$. Ring 1 is 157.6$^o$ from the beam direction whereas Ring 6 is only 72.05$^o$. **(a)** No Doppler correction has been applied. Ring 1 has experienced a downwards shift in energy whilst Ring 6 has experienced an upward shift. **(b)** Doppler corrected, shifts in energy have been corrected and now indicate the true energy.

### 3.4.6 Gamma-ray coincidences

The identification of $\gamma$-ray emissions from a nucleus is of limited use unless nuclear structure information can be retrieved. Due to the limited resolution of electronic timing, $\sim$10 ns, successive $\gamma$-ray transitions appear to be emitted simultaneously while being separated by sub-nanosecond state lifetimes.

Although a comprehensive ordering of prompt transitions based on electronic

timing is not possible and alternative methods of lifetime determination cannot be employed using only the apparatus described in Section 3.3, the de-excitation process can be reconstructed using coincidences between transitions. This provides an insight into the behaviour of the nucleus during de-excitation as transitions that are truly coincident represent successive changes in the structure of the nucleus.

In this work, transitions are considered to be coincident if they occur within $\sim$50 ns (5 time stamps) of each other. This accounts for the variations in the signal processing time of the detector electronics. In high-multiplicity events such as de-excitation following fusion evaporation reactions, the number of coincident transitions in an event is equal to the fold, the number of detected transitions. High-fold coincidences are desirable as they provide constraints with which to identify a decay path.

When studying high-fold coincidences, the lower fold data must be discarded. This is not true of studying lower fold data, as higher fold data can be unpacked into lower fold events. For example, when studying two-fold data, a three-fold event can be considered as three pairs of two-fold events, whereas when studying three-fold data, two-fold or lower events cannot form any three-fold events and must be discarded.

For ease of analysis, coincidence data is stored in a symmetrised matrix, as shown in Figure 3.16. The benefit of storing coincidences in this manner is that by selecting a $\gamma$-ray energy on one axis and projecting onto the other, a spectrum can be obtained that indicates which transitions are in coincidence with this $\gamma$ ray. The analysis of a number of $\gamma$-ray coincidence spectra may identify discrete decay paths by which the nucleus loses excitation energy and allow for an energy level scheme to be built for the nucleus.

Unobserved decay paths of statistical transitions can feed the level scheme such that a number of levels are by-passed. As such, transitions at lower excitation

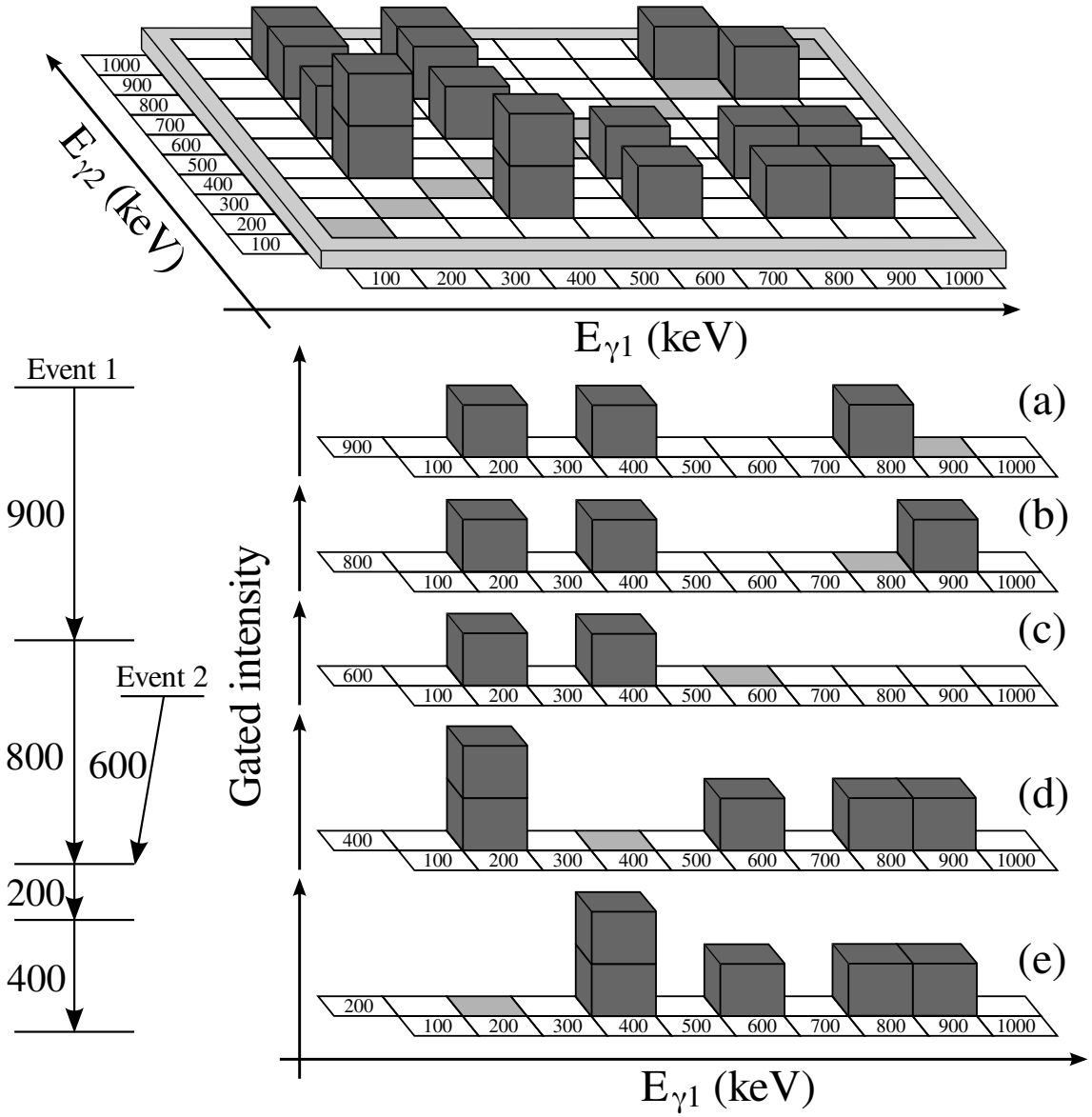


Figure 3.16: A symmetrised matrix containing data from an example level scheme. Two events, Event 1 (900,800,200,400) and Event 2 (600,200,400), have been unpacked and stored. Projections of 900, 800, 600, 400 and 200 keV across the matrix are shown and indicate coincidences with those $\gamma$-ray energies. A 600 keV transition is not present in projections of **(a)** 900 keV and **(b)** 800 keV as it lies in a separate decay path. Similarly, 800 and 900 keV transitions are not present in the projection of **(c)** 600 keV. The 600, 800 and 900 keV transitions are all present in projections of **(d)** 400 keV and **(e)** 200 keV, indicating that the separate decay paths converge.

energies occur more frequently than those at higher excitation energies, increasing their relative intensity. This makes it possible to order transitions within a discrete decay path.

### 3.4.7 Background and contamination

The effects of background noise on experimental apparatus can have disastrous consequences for successful analysis in that it can severely hinder the accuracy with which a measurement can be made, possibly obscuring data to the point of statistical insignificance. There are many possible sources that can introduce background effects into the system ranging from electronic noise in the detectors to randomly coincident radiation and the ability to suppress these effects is of tremendous importance. The suppression of unwanted background can be achieved through many different methods, appropriate to the scenario, which can be considered to be either the selection of "good" data or the subtraction of "bad" data.

Ensuring that certain conditions are passed before collecting data reduces background effects by only selecting "good" data. The RDT technique, as previously discussed, is used to select data from a relatively large $\gamma$-ray background, as displayed in Figure 3.12.

In contrast, background subtraction identifies "bad" data and removes it. In order to perform background subtraction techniques, a knowledge of the source of the background is necessary. In the ideal case, the background contributions to the data can be collected separately. With an unsubtracted spectrum and a spectrum of the background, normalisation and subtraction can effectively remove the background components.

If unwanted data are present in a tagged spectrum due to an inadequacy of the tagging conditions the spectrum is considered to be contaminated. The most common forms of contamination, using the apparatus and techniques in this chapter,

occur due to unwanted events with similar decay properties passing the tagging conditions, and miscorrelations due to random recoil implantation between tagged decays and their associated recoil.

The range of reaction channels populated during fusion evaporation reactions ensures that a variety of nuclei with different decay properties reach the focal plane. If there is any overlap between these decay properties it is possible for the tagging conditions to include more than just the desired decay, ultimately leading to unwanted features in tagged spectra. Such contamination can be removed in the same way that background can be subtracted, by obtaining a spectrum of the contaminant, normalising it to the contamination in the tagged spectrum and subtracting. Obtaining a spectrum of the contaminant is vital to its removal from the tagged spectrum, the ease and quality of which is entirely situation dependant.

Contamination by miscorrelation occurs when an unrelated recoil enters a DSSD pixel after a recoil of interest, but before the decay, as shown in Figure 3.17. Tagging on the decay causes it to be falsely correlated with the unrelated recoil, incurring contamination. The unrelated recoil is not entirely random as it will depend not only on the available recoils and their production cross sections, but also on the half-life of the unrelated recoil. Those with shorter half-lives are more likely to decay before the desired recoil decays, preventing the miscorrelation. Those with longer half-lives are less likely to decay before the desired recoil, incurring a miscorrelation.

Obtaining a background spectrum is not simple. While recoil gated transitions will provide a spectrum which contains data in the proportions in which reaction products are produced, they do not account for the variations in half-life specific to each channel. As such, an alternative method must be used to obtain a background spectrum that accounts for the half-life of the unrelated recoils. An appropriate background spectrum can be obtained by collecting $\gamma$ rays associated with a recoil that is followed by a recoil within the RDT time gate used for the nucleus of inter-

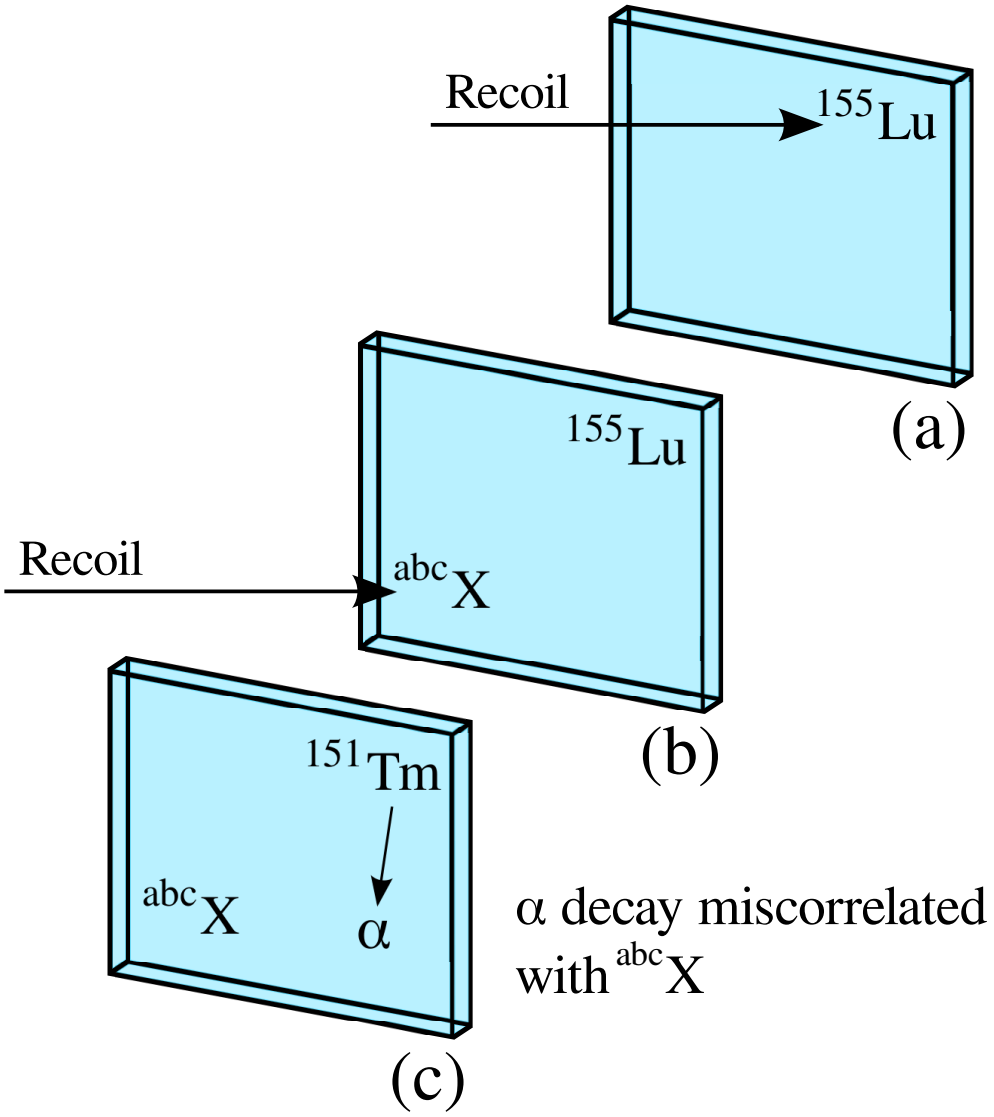


Figure 3.17: A mechanism by which miscorrelations can occur in a DSSD pixel. **(a)** A recoil of interest becomes implanted in the DSSDs. **(b)** An unrelated recoil becomes implanted in the same DSSD pixel shortly after the first. **(c)** The first recoil decays via $\alpha$ emission. The last recoil in the pixel is falsely identified as the source of the $\alpha$ decay.

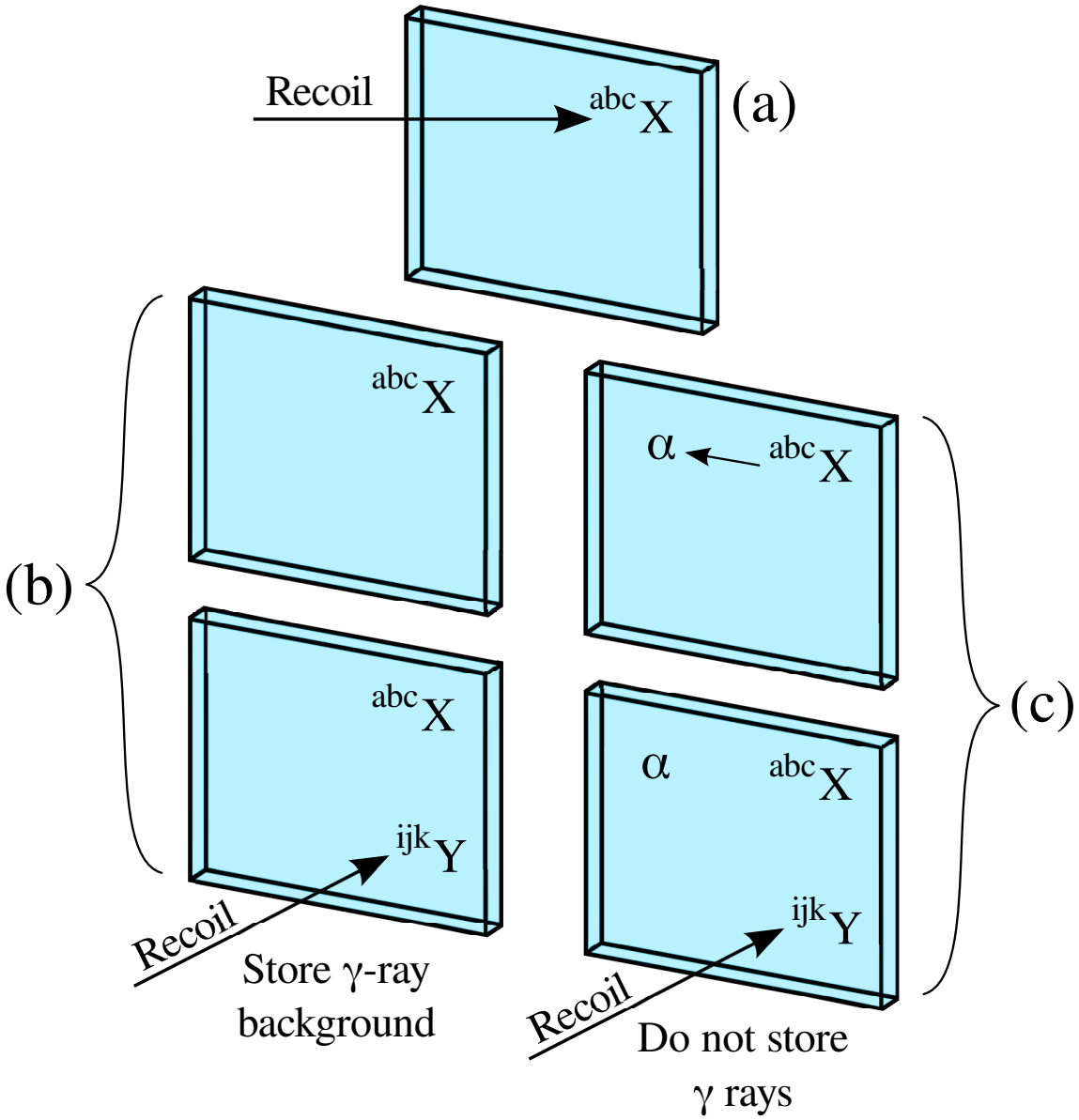


Figure 3.18: Obtaining a miscorrelation background spectrum. **(a)** A recoil, $^{abc}$X, assuming the role of the miscorrelated recoil, becomes implanted in a DSSD pixel. **(b)** Another recoil enters the pixel within the correlation time and before the $^{abc}$X recoil decays. The $\gamma$-ray transitions associated with $^{abc}$X are stored as miscorrelated background. **(c)** The $^{abc}$X recoil decays before the $^{ijk}$Y recoil enters the pixel. During RDT, $^{abc}$X would not have been miscorrelated, and so its associated $\gamma$-ray transitions are not stored as background.

est. This ensures that the channels with a relatively long half-life, and thus more dominant in the background, are collected more frequently while those with a relatively short half-life, which are less dominant in the background, are collected less frequently. This process is shown in Figure 3.18. The normalisation and subtraction of this background spectrum will then remove miscorrelated data from the tagged spectrum.

# Chapter 4

# Multiparticle configurations of excited states in $^{155}$Lu

In this chapter, excited states in the odd-$A$ nucleus $^{155}$Lu, $Z = 71$ and $N = 84$, are observed and nucleon configurations associated with these states are discussed. The $^{155}$Lu nucleus is located two neutrons above the $N = 82$ shell closure and in close proximity to the proton drip line. Nucleons are expected to occupy the proton $h_{11/2}$, $d_{3/2}$, $s_{1/2}$ and neutron $f_{7/2}$, $h_{9/2}$, $i_{13/2}$ orbitals.

Previous work has confirmed the existence of three $\alpha$-decaying states in $^{155}$Lu [27–29] of which the ground state is thought to be of spin and parity $3/2^+$ based on the odd proton occupying the $d_{3/2}$ orbital [30]. A low-lying $\alpha$-decaying isomer of spin and parity $11/2^-$ is based on the odd proton occupying the $h_{11/2}$ orbital [31]. A high-spin isomer of spin and pairty $25/2^-$ is based on the $[\pi h_{11/2} \otimes \nu h_{9/2} f_{7/2}]_{25/2^-}$ configuration. Excited states above the $11/2^-$ and $25/2^-$ $\alpha$-decaying states have been observed in previous work using the RDT technique [4, 32]. A level scheme of $\alpha$-decaying and excited states in $^{155}$Lu, prior to this work, is shown in Figure 4.1.

In this work, an experiment was performed that allows for a significant revision of the previous level scheme. The experiment was performed at the Accelerator Lab-

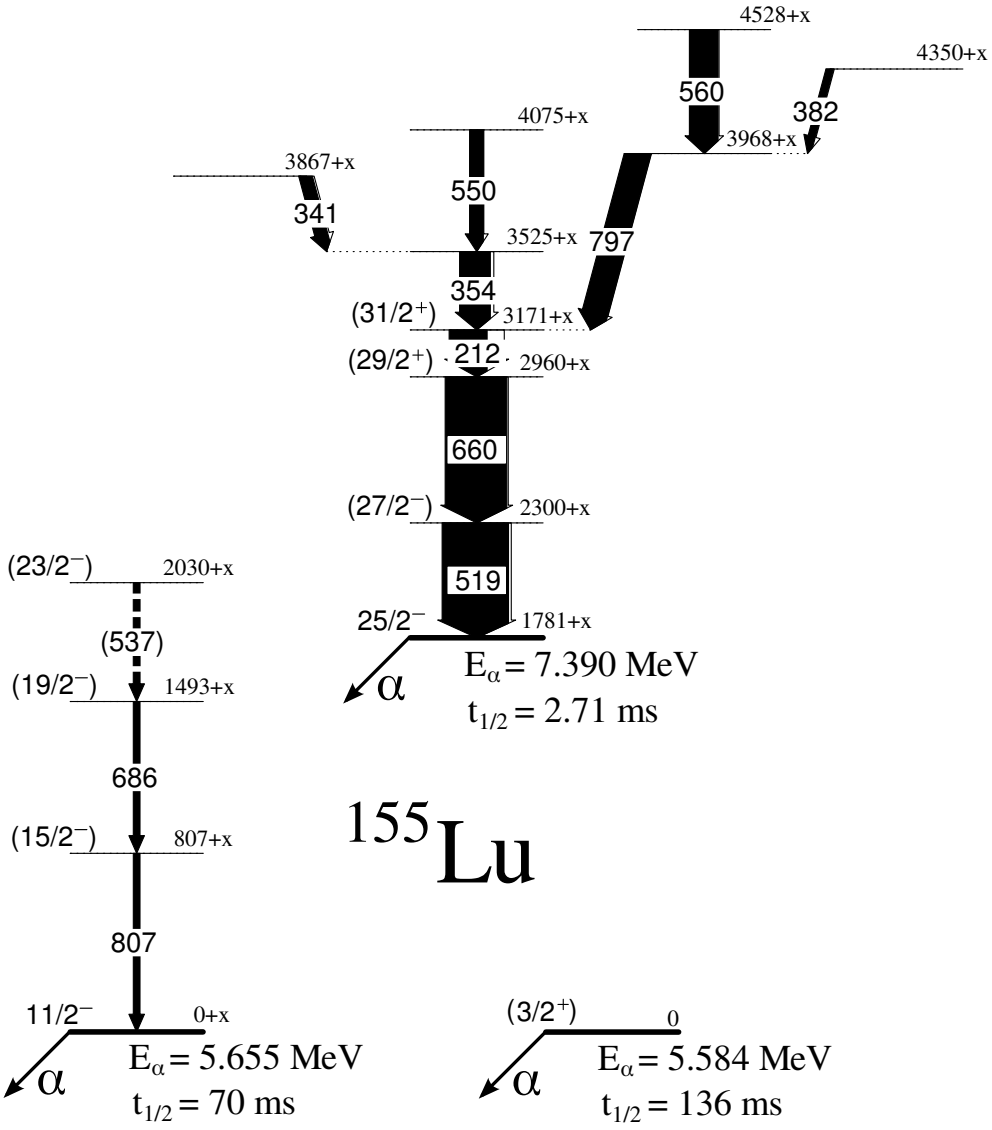


Figure 4.1: Previous level scheme for $^{155}$Lu [4, 27–30, 32, 33].

oratory at the University of Jyväskylä using the apparatus described in Chapter 3. An accelerated $^{58}Ni^{11+}$ beam has been produced, with a beam energy of 255 MeV, and projected onto an enriched $^{102}$Pd target of thickness $\sim$1 mg cm$^{-2}$. The reaction

$$^{102}\mathrm{Pd}(^{58}\mathrm{Ni},\alpha\mathrm{p})^{155}\mathrm{Lu}^{*}$$

is one of a number of possible reaction channels and it produces $^{155}$Lu nuclei in excited states. These nuclei will emit prompt $\gamma$ rays at the target position and $\alpha$ decay at the focal plane as previously described. The beam energy used in this experiment is preferable to that of previous $\gamma$-ray spectroscopy experiments [4, 32, 34, 35] for populating excited states in $^{155}$Lu.

The RDT technique has been employed to identify $\gamma$-ray transitions feeding the known $\alpha$-decaying states. A revised level scheme has been constructed and single-particle configurations have been assigned. Previous studies of isotone chains in this region have revealed a lowering in excitation energy of states built on configurations that include a neutron in the $h_{9/2}$ orbital as the proton occupation of the $h_{11/2}$ orbital increases [4, 36–39]. The revised $^{155}$Lu level scheme and single-particle configurations are compared with neighbouring $N = 84$ isotones and systematic trends are discussed.

A number of challenges are presented in the study of $^{155}$Lu in this experiment, particularly with regard to the identification of the nucleus itself. The gas-filled nature of the RITU separator prevents identification using the $A/q$ ratio and the RDT technique is very much relied upon for the identification of reaction products. However, two of the three known $^{155}$Lu $\alpha$ decays lie in an energy region dominated by the $\alpha$ decays of stronger reaction channels. Similarities between the energies and decay times of the $^{155}$Lu $\alpha$ decays and those of stronger reaction channels result in correlated $^{155}$Lu $\gamma$-ray spectra being contaminated. Careful consideration of background and contamination effects is required to extract $^{155}$Lu $\gamma$-rays.

## 4.1 Results

Gamma rays associated with $^{155}$Lu can be obtained using the RDT technique by correlating with the known $\alpha$ decays. The energies and half-lives of the three known $\alpha$ decays in $^{155}$Lu are displayed in Table 4.1 along with possible contaminants, which are similar in energy.

| Nucleus | $E_\alpha$ (keV) | $t_{1/2}$ (ms) | $J_i^\pi \rightarrow J_f^\pi$ | $b_\alpha$ (%) |
|---|---|---|---|---|
| $^{155}Lu_{(3/2^+)}$ | 5584(5) | 136(9) | $(3/2^+) \rightarrow (1/2^+)$ | |
| $^{155m1}Lu_{(11/2^-)}$ | 5655(5) | 70(1) | $(11/2^-) \rightarrow (11/2^-)$ | 81(9) |
| $^{155m2}Lu_{(25/2^-)}$ | 7390(8) | 2.71(3) | $(25/2^-) \rightarrow (25/2^-)$ | |
| Nucleus | $E_\alpha$ (keV) | $t_{1/2}$ (ms) | Data affected | $b_\alpha$ (%) |
| $^{156m1}$Lu | 5565(4) | 198(2) | $^{155}Lu_{(3/2^+)}$ | 98(9) |
| $^{157}$Hf | 5729(4) | 115(1) | $^{155}Lu_{(3/2^+)}$, $^{155m1}Lu_{(11/2^-)}$ | 95(5) |
| $^{159m1}$Ta | 5599(5) | 554(16) | $^{155}Lu_{(3/2^+)}$ | 73(14) |

Table 4.1: Known $\alpha$ decays from $^{155}$Lu and possible contaminants [27–30, 40].

Observing decays preceded by a recoil at these energies in the DSSDs, Figure 4.2, reveals that peaks corresponding to the decays from the $^{155}Lu_{(3/2^+)}$ and $^{155m1}Lu_{(11/2^-)}$ states are not clearly visible and are contaminated in energy by decays from more strongly populated channels. The decay of the $^{155m2}Lu_{(25/2^-)}$ state is clearly visible and does not appear to be contaminated by other decays.

From these observations, $\gamma$-ray spectra obtained using the RDT technique of transitions feeding the $^{155}Lu_{(3/2^+)}$ and $^{155m1}Lu_{(11/2^-)}$ states are expected to be strongly contaminated, while the spectrum for the $^{155m2}Lu_{(25/2^-)}$ state is expected to be relatively clean. This indeed proves to be the case, as indicated by the RDT spectra in Figure 4.3, with contamination from $^{157}$Hf present in both the $^{155}Lu_{(3/2^+)}$ and $^{155m1}Lu_{(11/2^-)}$ spectra and from $^{156}$Lu in the $^{155}Lu_{(3/2^+)}$ spectrum. No known contaminants are present in the $^{155m2}Lu_{(25/2^-)}$ spectrum.

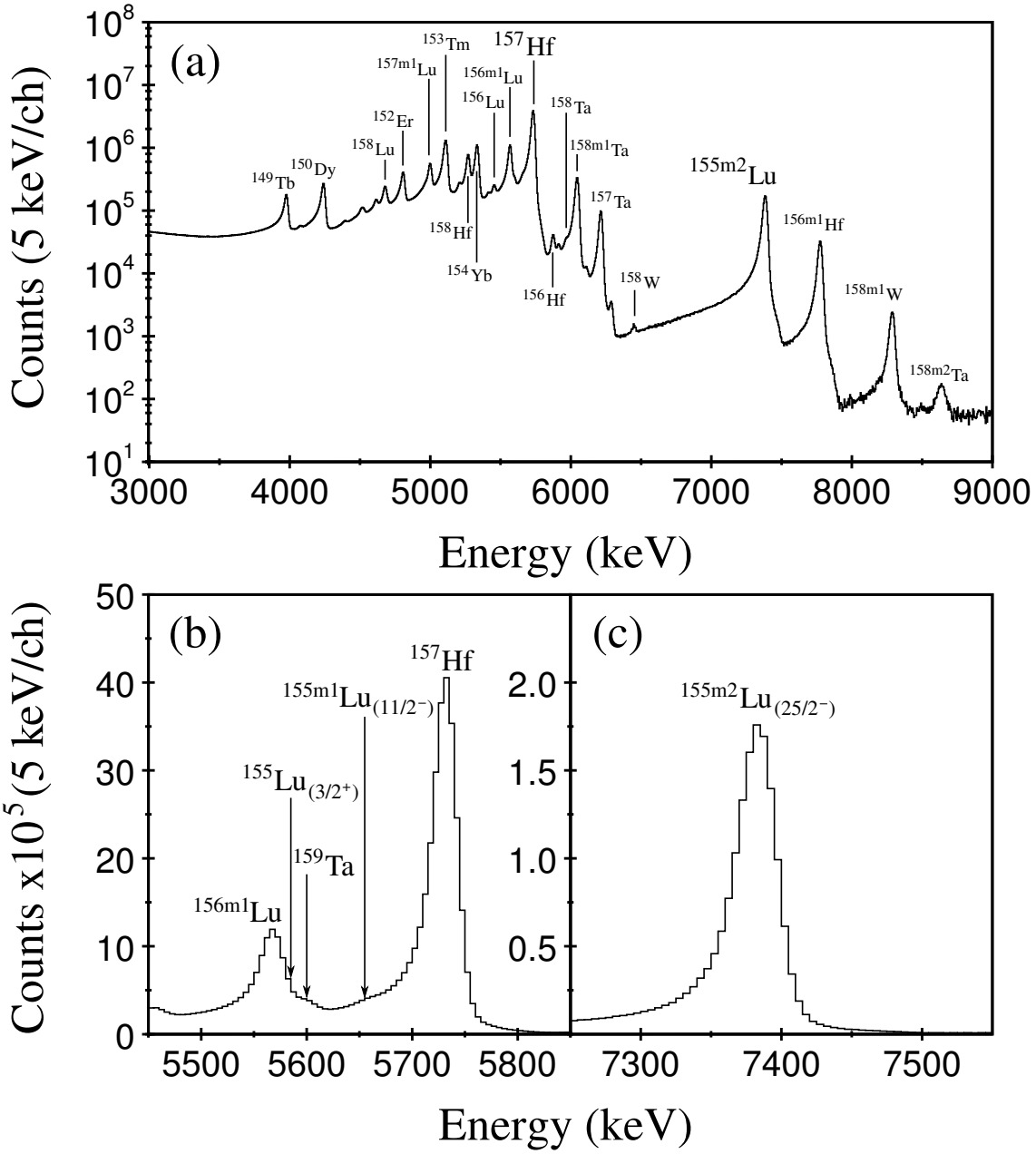


Figure 4.2: **(a)** Energy spectra of decays occurring within 700 ms of a recoil implantation in the same DSSD pixel. **(b)** The same spectrum expanded around the $^{155}\mathrm{Lu}_{(3/2^+)}$ and $^{155m1}\mathrm{Lu}_{(11/2^-)}$ $\alpha$ decays. **(c)** The same spectrum expanded around the $^{155m2}\mathrm{Lu}_{(25/2^-)}$ decay.

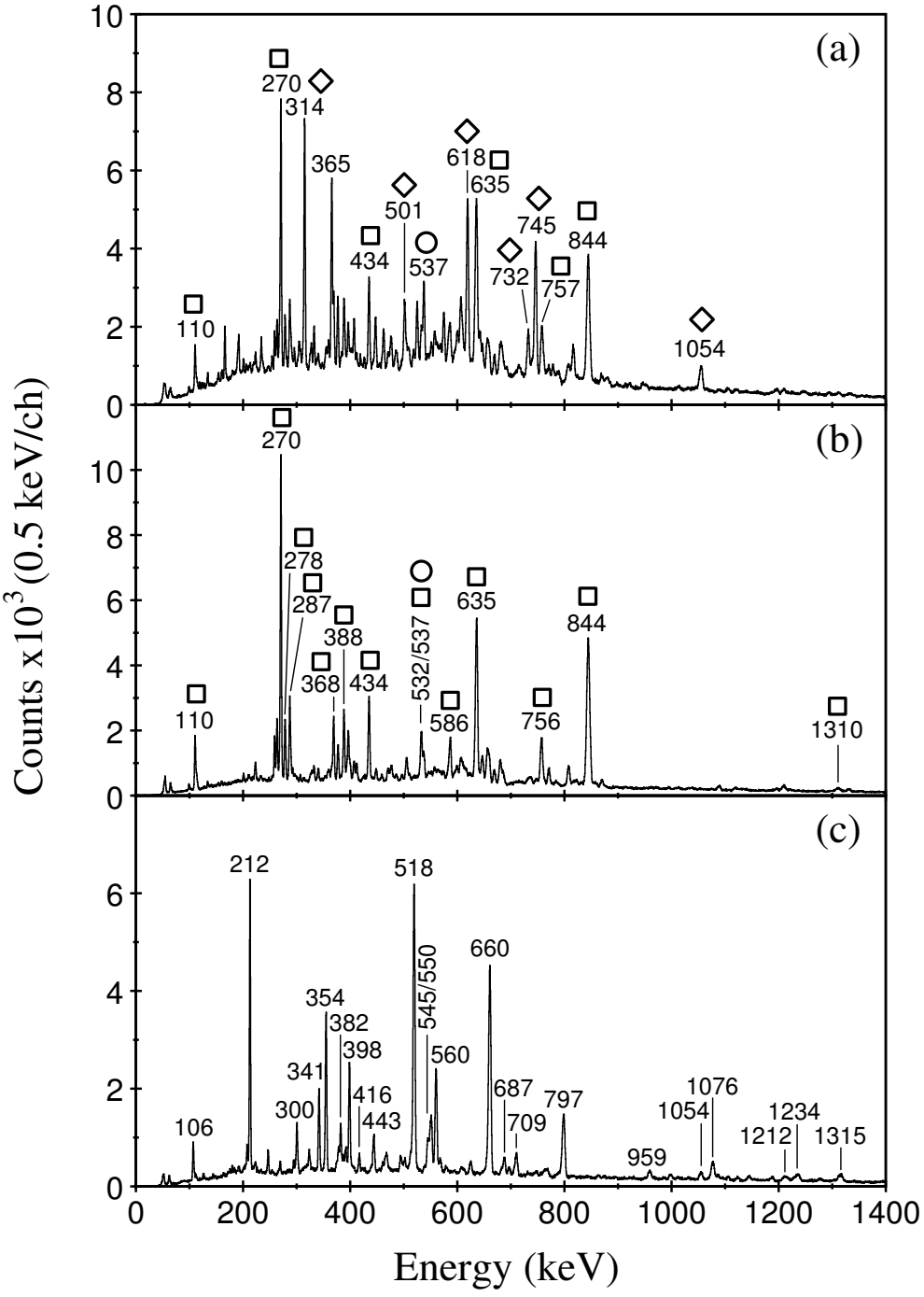


Figure 4.3: Energy spectra of $\gamma$-ray transitions detected at the target position and correlated with recoils identified using the RDT technique on **(a)** the $^{155}\mathrm{Lu}_{(3/2^+)}$ state using a correlation time of 680 ms, **(b)** the $^{155m1}\mathrm{Lu}_{(11/2^-)}$ state using a correlation time of 350 ms and **(c)** the $^{155m2}\mathrm{Lu}_{(25/2^-)}$ state using a correlation time of 14 ms. Spectra in (a) and (b) are contaminated by $^{157}$Hf (squares), $^{156}$Lu (diamonds) and $^{157}$Lu (circles).

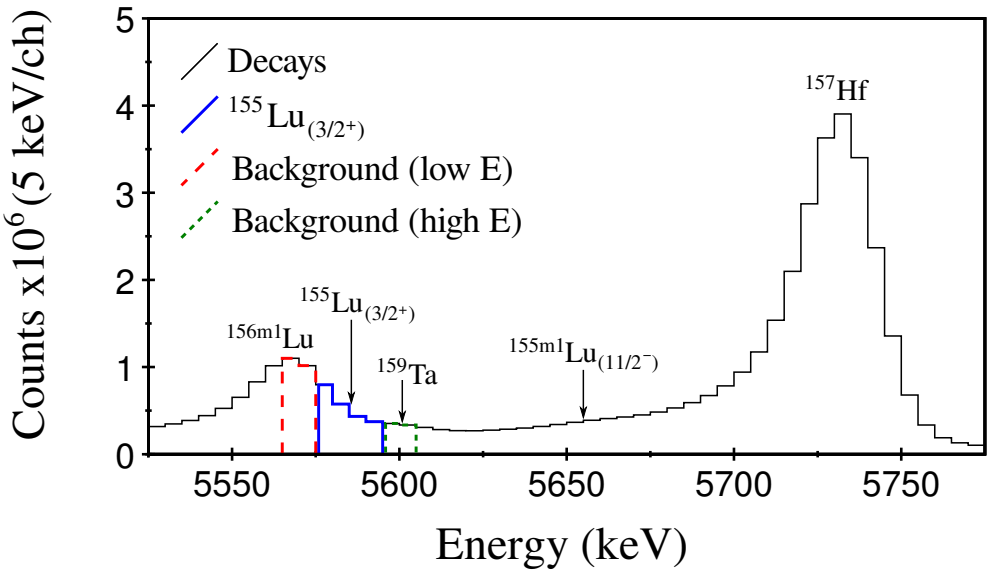


Figure 4.4: Energy spectrum of decays occurring within 680 ms of a recoil implantation in the same DSSD pixel with the energy conditions for the $^{155}$Lu$_{(3/2^+)}$ state and its background components included. The correlated $\gamma$-ray transitions are displayed in Figure 4.5.

### 4.1.1 Transitions feeding the $(3/2^+)$ isomer

As indicated in Figure 4.3(a), $\gamma$-ray transitions feeding the $^{155}$Lu$_{(3/2^+)}$ state cannot be obtained by simply employing the RDT technique due to contamination from other reaction products with similar $\alpha$ decay properties. Indeed, contamination can be expected from $^{156}$Lu, $^{157}$Hf, $^{159}$Ta and $^{155m1}$Lu$_{(11/2^-)}$. The absence of a clearly observable $\alpha$-decay peak suggests that the $^{155}$Lu$_{(3/2^+)}$ state is rather weakly populated in this reaction.

The number of contaminants leads to a rather complex $\gamma$-ray background whose individual components are difficult to select. In order to overcome this, a narrow gate has been used over the energy range for which the $^{155}$Lu$_{(3/2^+)}$ $\alpha$-decay peak will be at its most intense. Correlations with background contaminants have been made over a narrow energy range either side of the $^{155}$Lu gate. The energy conditions for $^{155}$Lu$_{(3/2^+)}$ and the accompanying background are shown in Figure 4.4 and the $\gamma$-ray

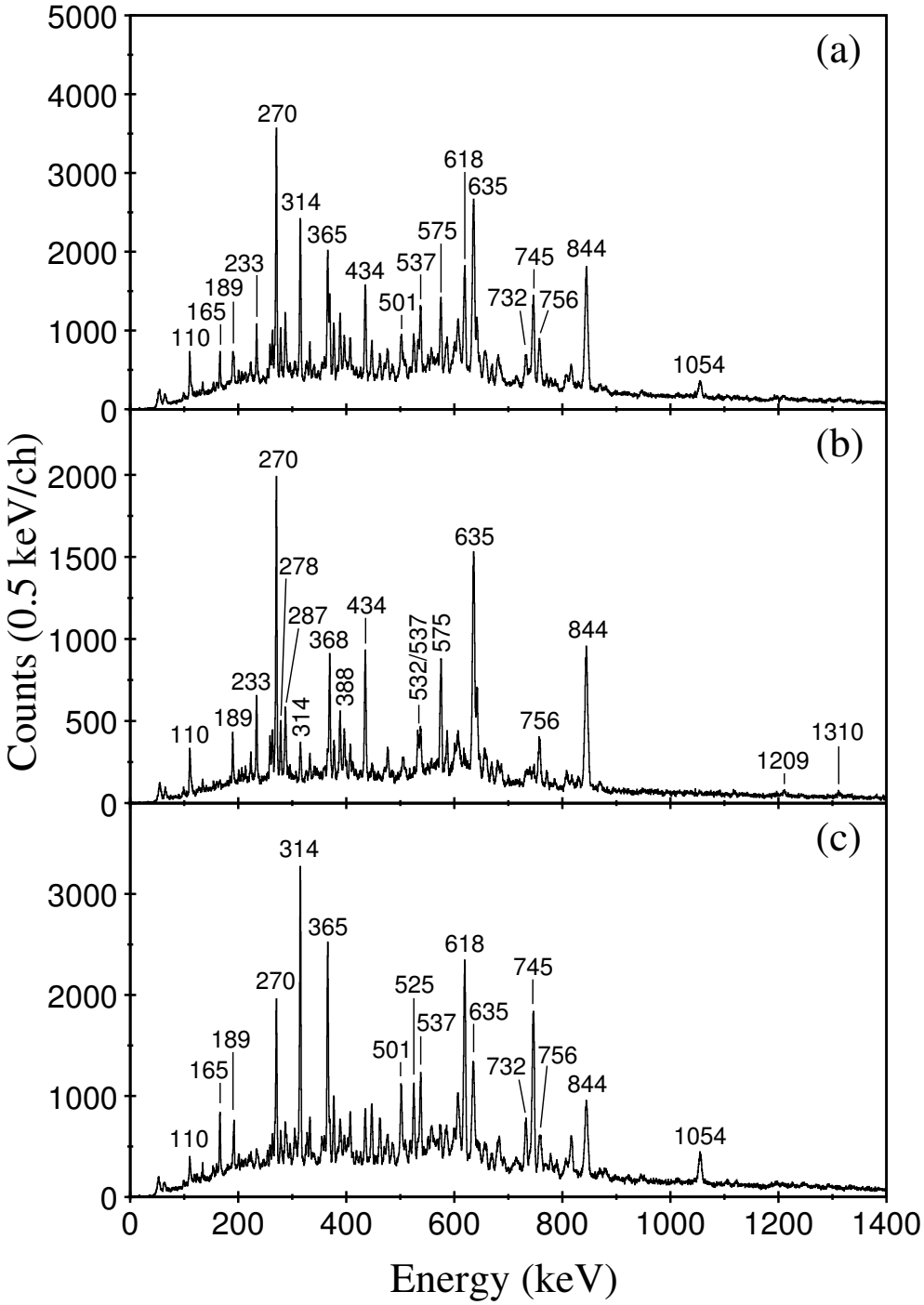


Figure 4.5: Energy spectra of $\gamma$ rays obtained using the RDT technique for the gates shown in Figure 4.4 each with a correlation time of five $^{155}$Lu$_{(3/2^+)}$ half-lives (680 ms). **(a)** The $^{155}$Lu$_{(3/2^+)}$ gate. **(b)** The high-energy background gate. **(c)** The low-energy background gate. All spectra contain transitions from $^{157}$Hf, $^{156}$Lu and $^{157}$Lu, which constitute the majority of the background in the $^{155}$Lu$_{(3/2^+)}$ tagged spectrum.

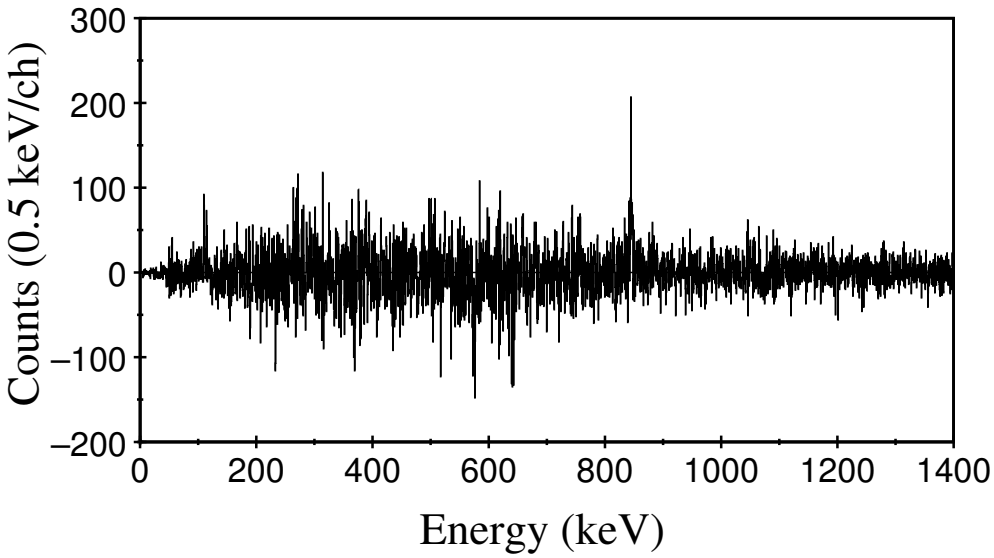


Figure 4.6: Energy spectrum of transitions feeding the $^{155}$Lu$_{(3/2^+)}$ state, Figure 4.5(a), with the background components, Figure 4.5(b) and (c), normalised and subtracted. No clear $\gamma$-ray peaks remain. The feature at 844 keV is only one channel wide and appears strongly in the background spectra.

spectra corresponding to these conditions are shown in Figure 4.5. The low-energy and high-energy background spectra have been normalised to the intensities of the low-energy half and high-energy half of the $^{155}$Lu$_{(3/2^+)}$ energy gate, respectively.

Following the subtraction of the normalised background spectra from the $^{155}$Lu$_{(3/2^+)}$ tagged spectrum, no $\gamma$-ray peaks can be seen, as shown in Figure 4.6. The only notable feature is an apparent peak at 844 keV, however, this peak features strongly in the background and as the majority of the intensity resides in a single channel it is not considered to be a true peak. As such, no transitions have been observed feeding the $^{155}$Lu$_{(3/2^+)}$ state. It is likely that states feeding the $^{155}$Lu$_{(3/2^+)}$ state were not strongly populated in this experiment.

### 4.1.2 Levels above the $(11/2^-)$ isomer

As with the $^{155}$Lu$_{(3/2^+)}$ state, tagging directly on decays from the $^{155m1}$Lu$_{(11/2^-)}$ state produces a $\gamma$-ray spectrum that is dominated by contaminants, obscuring transitions

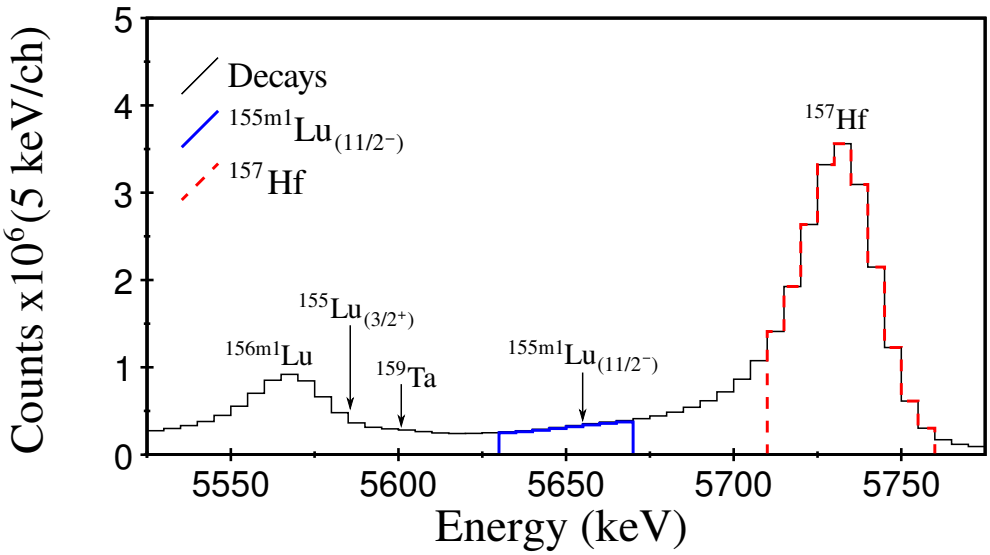


Figure 4.7: Energy spectrum of decays occurring within 350 ms of a recoil implantation in the same DSSD pixel with the energy conditions for the $^{155m1}$Lu$_{(11/2^-)}$ state and the $^{157}$Hf contaminant included. The correlated $\gamma$ rays are displayed in Figure 4.8.

feeding the $^{155m1}$Lu$_{(11/2^-)}$ state, see Figure 4.3(b). The tagged $^{155m1}$Lu$_{(11/2^-)}$ spectrum is predominantly contaminated by $^{157}$Hf. This scenario is favourable to that of the $^{155}$Lu$_{(3/2^+)}$ state as an accurate representation of the background can be easily obtained, allowing for a wider $^{155m1}$Lu$_{(11/2^-)}$ energy gate to be used.

The background can be selected with an energy condition around the $^{157}$Hf $\alpha$-decay peak, as shown in Figure 4.7, which excludes the $^{155m1}$Lu$_{(11/2^-)}$ $\alpha$ decay. The correlated spectra are shown in Figure 4.8. Normalising peaks in the correlated background spectrum to the contaminant $^{157}$Hf $\gamma$-ray transitions in the $^{155m1}$Lu$_{(11/2^-)}$ spectrum allows for the entire $^{157}$Hf background to be normalised and subtracted from the correlated $^{155m1}$Lu$_{(11/2^-)}$ $\gamma$-ray spectrum. The effect of such treatment on the contaminated $^{155m1}$Lu$_{(11/2^-)}$ data, normalising the 636 keV peaks to each other, is shown in Figure 4.8(c). Immediately apparent is the over-subtraction of the strongest $^{157}$Hf transitions. This suggests that there is another component to the 636 keV peak resulting in the incorrect normalisation and over-subtraction of

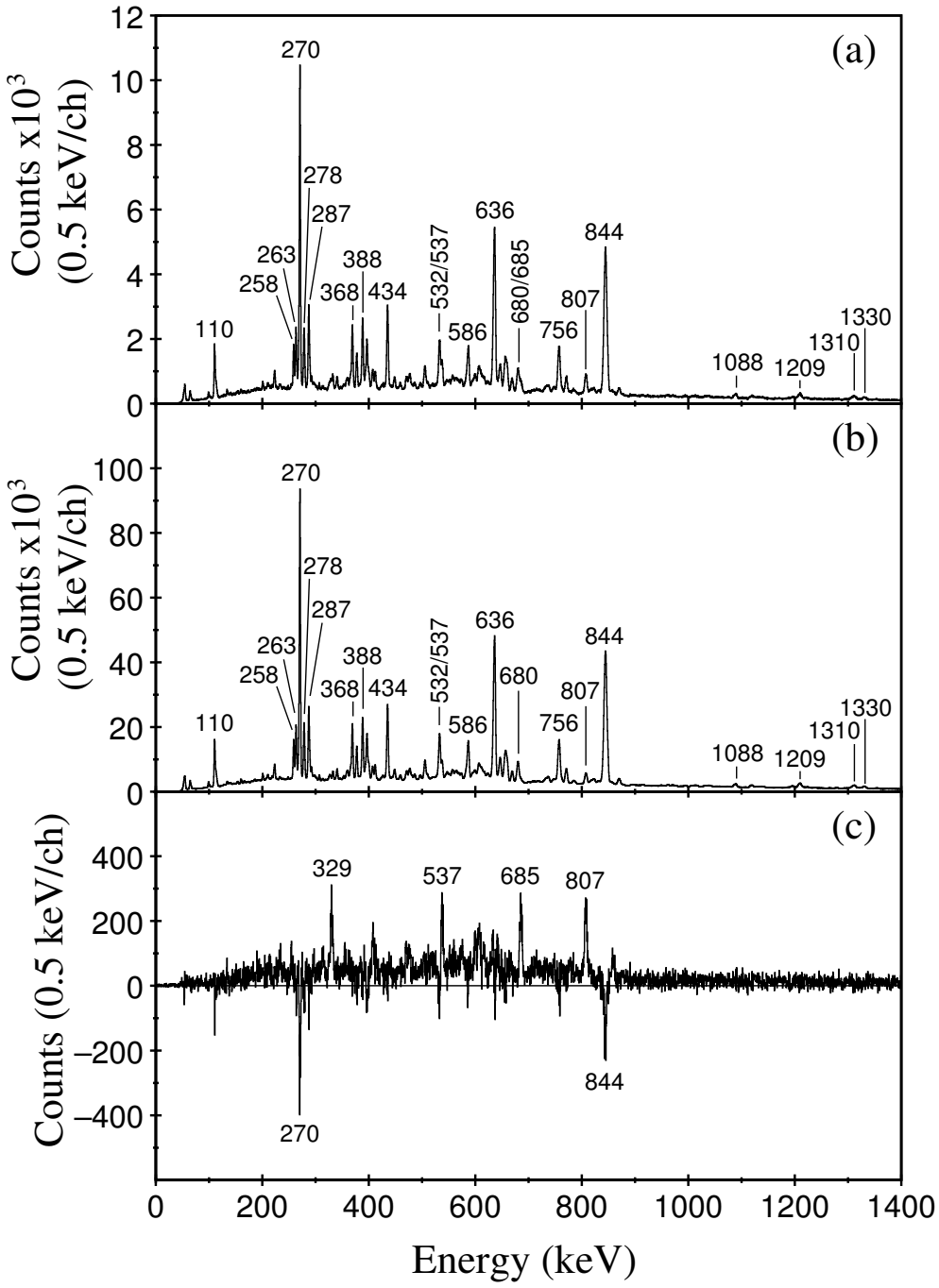


Figure 4.8: Energy spectra of $\gamma$ rays obtained using the RDT technique tagging on decays from **(a)** the $^{155m1}\mathrm{Lu}_{(11/2^-)}$ state with a correlation time of 350 ms and **(b)** the $^{157}\mathrm{Hf}_{7/2^-}$ state with a correlation time of 350 ms. **(c)** A difference spectrum of (b) normalised to the 636 keV $^{157}$Hf transition in (a) and subtracted. Over-subtraction suggests that another source of contamination is present.

the $^{157}$Hf contamination.

While it is possible that a 636 keV transition feeds the $^{155m1}\mathrm{Lu}_{(11/2^-)}$ state, a transition of that energy is also present in the decay of $^{157}$Lu, the strongest reaction channel in this experiment, introducing the possibility that miscorrelated transitions contaminate the $^{155m1}\mathrm{Lu}_{(11/2^-)}$ data. This argument is reinforced by the presence of a 537 keV transition, also present in $^{157}$Lu, in the subtracted spectrum.

As described in Section 3.4.7, a miscorrelation spectrum can be obtained by observing the $\gamma$-ray transitions associated with recoils that enter a DSSD pixel and are followed, within the RDT correlation time, by another recoil. As there are now two background spectra, the different contributions of each must be determined in order to perform an effective subtraction. This could be performed by normalising peaks in the background spectra to those in the tagged spectrum, however, as the $^{157}$Hf peaks are also present in the miscorrelation spectrum this is not possible as the relative contributions to the peaks are not known.

To determine the contributions of each background component a comparison between the ratio of intensities of the 270 and 636 keV transitions can be made. The ratios are quite different as the miscorrelation spectrum contains 636 keV transitions from $^{157}$Lu in addition to those from $^{157}$Hf. From the equation

$$\frac{I_{tagged}(270)}{I_{tagged}(636)} = \frac{A(I_{contaminant}(270)) + I_{miscorrelation}(270)}{A(I_{contaminant}(636)) + I_{miscorrelation}(636)}, \tag{4.1}$$

where $I_{tagged}(keV)$, $I_{contaminant}(keV)$ and $I_{miscorrelation}(keV)$ are the intensities of peaks in the tagged, contaminant and miscorrelation spectra, respectively, and $A$ is a coefficient which controls the contaminated background relative to the miscorrelated background, determining the value of $A$ enables the relative contributions of the background spectra to be obtained.

Upon determining the relative contributions of the two background components,

| $E_\gamma$ (keV) | I | $J_i^\pi$ | $\rightarrow$ | $J_f^\pi$ |
|---|---|---|---|---|
| 328.7(2) | 323(23) | $(23/2^-)$ | $\rightarrow$ | $(19/2^-)$ |
| 684.8(3) | 818(76) | $(19/2^-)$ | $\rightarrow$ | $(15/2^-)$ |
| 806.7(3) | ≡1000 | $(15/2^-)$ | $\rightarrow$ | $(11/2^-)$ |

Table 4.2: Energies and efficiency corrected relative intensities of transitions feeding the $^{155m1}\mathrm{Lu}_{(11/2^-)}$ state.

a relative background spectrum can be produced using

$$S_{background} = A(S_{contaminant}) + S_{miscorrelation}, \tag{4.2}$$

where $S_{background}$ is the relative background spectrum, $S_{contaminant}$ and $S_{miscorrelation}$ are contaminant and miscorrelation spectra, respectively, and $A$ is as in Equation 4.1. Normalising the 636 keV peak in this compound background spectrum to the 636 keV peak in the unsubtracted $^{155m1}\mathrm{Lu}_{(11/2^-)}$ spectrum enables an improved background subtraction, as shown in Figure 4.9.

By carefully considering the background effects present in the tagged spectrum it has been possible to obtain a clean spectrum of transitions feeding the $^{155m1}\mathrm{Lu}_{(11/2^-)}$ state, Figure 4.9(c). Three transitions are clearly visible. The previously published 537 keV transition is not present in this spectrum. As this work used the same choices of beam and target, it is highly likely that a miscorrelated transition originating from $^{157}$Lu was wrongly assigned to $^{155}$Lu.

The energies and relative intensities of the extracted transitions are displayed in Table 4.2. Projections of these transitions on a $\gamma$-$\gamma$ coincidence matrix, Figure 4.10, indicate that these three transitions are all in coincidence with each other. The measured intensities of these transitions provide a basis for their ordering in a revised level scheme, Figure 4.11.

Although measurements of multipolarities were not possible on these transitions, comparison with neighbouring $N = 84$ odd-A isotones $^{151}$Ho [38] and $^{153}$Tm [39]

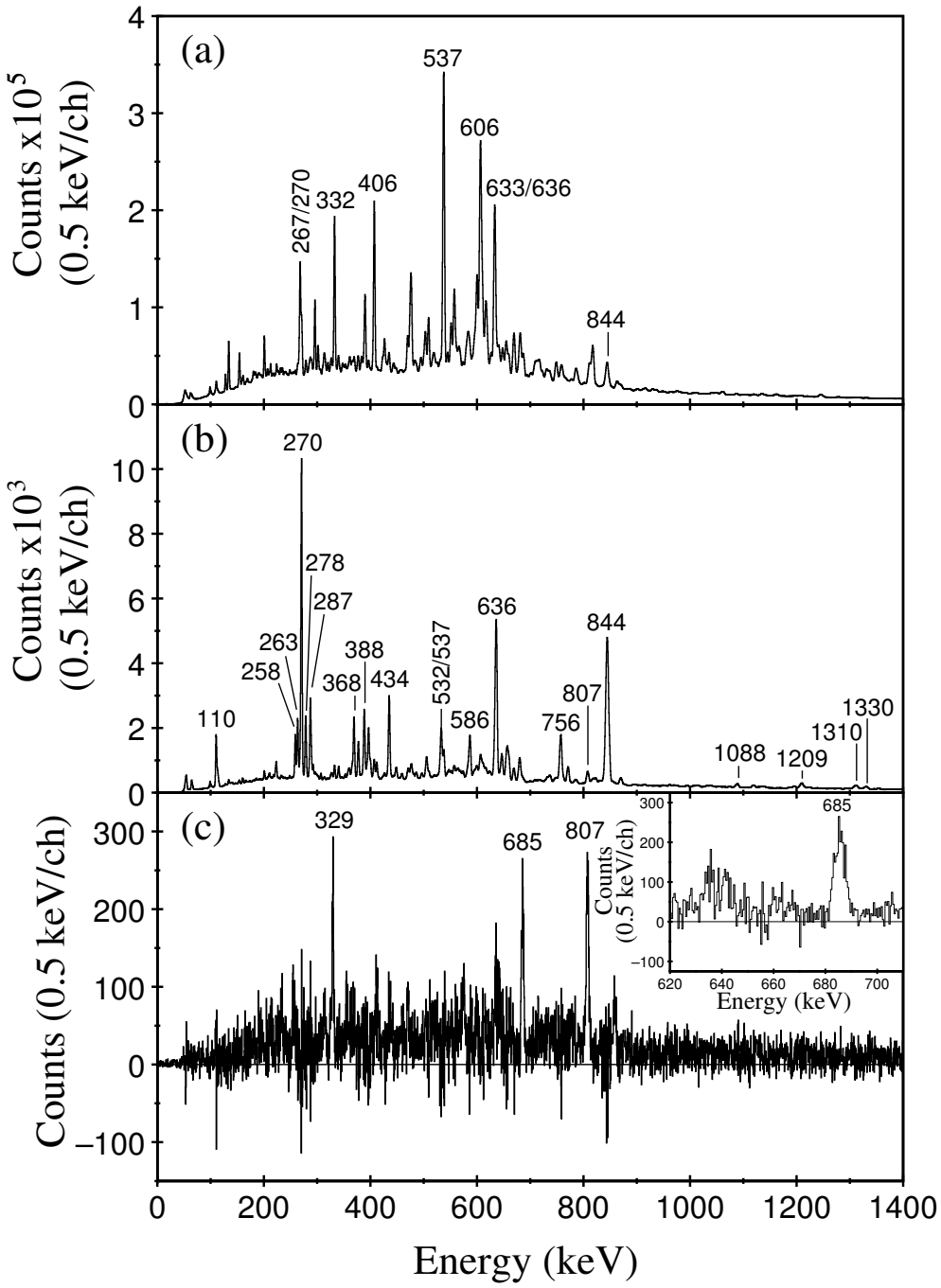


Figure 4.9: Energy spectra of $\gamma$ rays. **(a)** A miscorrelation spectrum, obtained by collecting $\gamma$ rays associated with a recoil followed by a recoil within the $^{155m1}\mathrm{Lu}_{(11/2^-)}$ RDT time window of 350 ms. **(b)** A compound background spectrum comprised of a $^{157}$Hf contamination spectrum and the miscorrelation spectrum shown in (a) with the appropriate relative contributions, with the 636 keV peak normalised to that in the tagged $^{155m1}\mathrm{Lu}_{(11/2^-)}$ spectrum. **(c)** The tagged $^{155m1}\mathrm{Lu}_{(11/2^-)}$ spectrum in Figure 4.8(a) with (b) subtracted. The resulting difference spectrum reveals transitions feeding the $^{155m1}\mathrm{Lu}_{(11/2^-)}$ state. The 537 keV transition previously reported [32] is not present. **(inset)** An expansion of (c) to highlight the feature at 656 keV. Lack of width indicates that it is not a true peak.

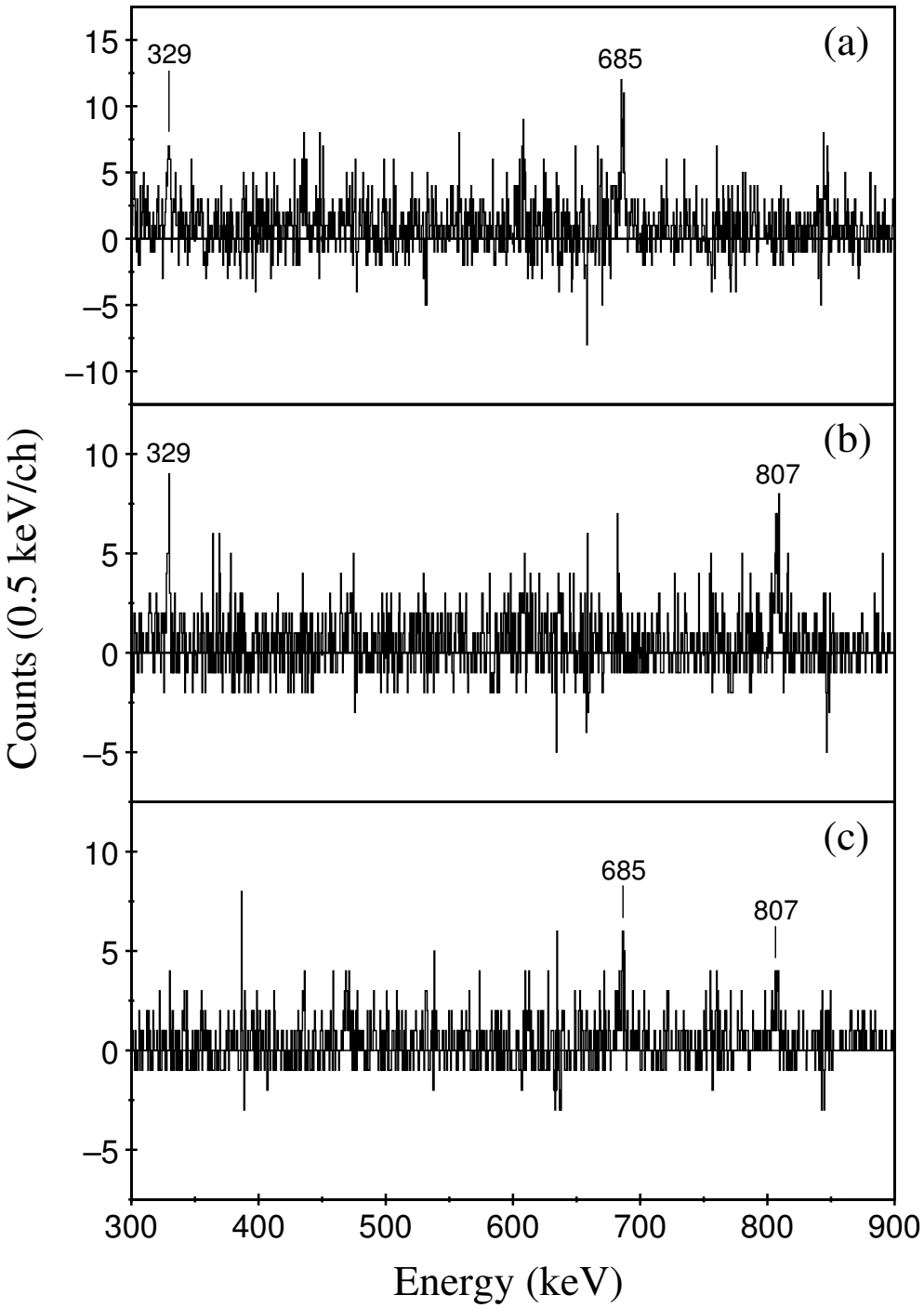


Figure 4.10: Gamma-ray coincidence spectra generated from a $^{155m1}\mathrm{Lu}_{(11/2^-)}$ $\alpha$-decay correlated matrix. **(a)** Spectrum in coincidence with the 807 keV transition. **(b)** Spectrum in coincidence with the 685 keV transition. **(c)** Spectrum in coincidence with the 329 keV transition.

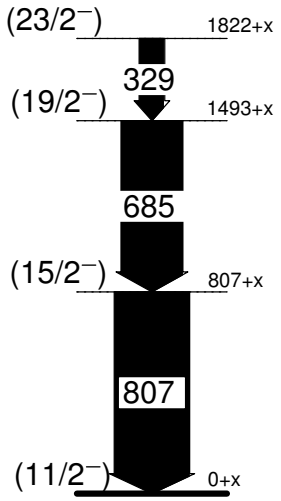


Figure 4.11: Transitions feeding the $^{155m1}\mathrm{Lu}_{(11/2^-)}$ state.

suggests that all three are of E2 character, bringing the nucleus to a fully aligned $[\pi h_{11/2} \otimes \nu(f_{7/2})^2]_{(23/2^-)}$ configuration. This will be discussed further in Section 4.2.

### 4.1.3 Levels above the $(25/2^-)$ isomer

The excitation energy of the $\alpha$-decaying $^{155m2}\mathrm{Lu}_{(25/2^-)}$ state itself is known relative to the $^{155m1}\mathrm{Lu}_{(11/2^-)}$ state [4] based on the assumption that both states $\alpha$ decay to the $^{151}\mathrm{Tm}_{(11/2^-)}$ state directly. Such a decay from the $^{155m2}\mathrm{Lu}_{(25/2^-)}$ state would be expected to incur large structural changes, hindering the decay. A comparison of the reduced decay width $\delta^2$, as described in Section 2.4, with a number of hindered and unhindered decays in this region of the nuclear chart makes it possible to deduce the angular momentum carried away from the nucleus during the decay process. This is shown in Figure 4.12.

An angular momentum change of 8 units incurs a $\delta^2$ for the $^{155m2}\mathrm{Lu}_{(25/2^-)}$ $\alpha$ decay consistent with that of other hindered decays in this region of the nuclear chart. This is consistent with either a state of spin $(25/2^-)$ or $(27/2^-)$ decaying to the $^{151}\mathrm{Tm}_{(11/2^-)}$ state directly. As such, the difference in the Q-value between $\alpha$ decays from the $^{155m1}\mathrm{Lu}_{(11/2^-)}$ and $^{155m2}\mathrm{Lu}_{(25/2^-)}$ states gives the relative excitation energy of the $^{155m2}\mathrm{Lu}_{(25/2^-)}$ state.

The $^{155m2}\mathrm{Lu}_{(25/2^-)}$ state is particularly well suited to the RDT technique, having a short half-life relative to the implantation rate and an energy that is not overlapped by other $\alpha$ decays. The result is a clean RDT $\gamma$-ray spectrum of transitions feeding the $^{155m2}\mathrm{Lu}_{(25/2^-)}$ state which contains very few contaminants or miscorrelations, as shown in Figure 4.3(c).

Statistics are significantly greater than in previous work and coincidence analysis has been used to produce the revised level scheme shown in Figure 4.13. Gamma-ray coincidence spectra are shown in Figures 4.14, 4.15, 4.16 and 4.17. The energies and relative intensities of the observed transitions are tabulated in Table 4.3.

The two lowest lying transitions in the revised level scheme agree with the previously published work [4, 32], however, at higher excitation energies there are significant deviations. The placement of the 212 keV in the previously published work

| $E_\gamma$ (keV) | $I_\gamma$ | $J_i^\pi$ | $\rightarrow$ | $J_f^\pi$ | Angular intensity ratio $\frac{I(157.6^o)}{I(94.16)}$ |
|---|---|---|---|---|---|
| 106.3(1) | 165(3) | $(31/2^+)$ | $\rightarrow$ | $(29/2^+)$ | 0.78(6) |
| 246.0(2) | 45(1) | | | | |
| 268.4(2) | 22(1) | | | | |
| 212.1(2) | 498(3) | (37/2) | $\rightarrow$ | (35/2) | 0.72(2) |
| 299.8(2) | 108(2) | | | | 0.86(7) |
| 322.8(8) | 38(2) | | | | |
| 341.1(2) | 172(2) | | | | 0.73(4) |
| 354.2(2) | 355(3) | | | | 0.91(3) |
| 377.4(2) | 17(2) | | | | |
| 381.5(2) | 64(2) | | | | |
| 397.9(2) | 245(3) | | | | 0.81(4) |
| 416.2(2) | 37(2) | | | | 0.73(14) |
| 443.3(2) | 100(2) | | | | 0.96(9) |
| 513.0(2) | 50(2) | | | | |
| 518.5(2)* | ≡1000(5) | $(27/2^-)$ | $\rightarrow$ | $(25/2^-)$ | 0.86(2) |
| 544.7(2) | 119(2) | | | | |
| 550.2(2)* | 231(3) | | | | |
| 559.5(2) | 353(4) | | | | 0.65(3) |
| 659.7(2)* | 1004(5) | $(29/2^+)$ | $\rightarrow$ | $(27/2^-)$ | 0.77(2) |
| 681.9(5) | 20(2) | | | | |
| 687.0(3) | 84(2) | | | | |
| 696.0(3) | 36(2) | | | | |
| 709.2(3) | 116(3) | | | | 0.67(7) |
| 797.5(3) | 403(4) | (35/5) | $\rightarrow$ | $(31/2^+)$ | 0.95(4) |
| 958.5(3) | 66(3) | | | | 1.27(28) |
| 997.5(4) | 28(2) | | | | |
| 1054.2(4) | 50(3) | | | | |
| 1076.2(4) | 148(4) | | | | |
| 1122.4(4) | 24(3) | | | | |
| 1144.1(4) | 33(2) | | | | |
| 1186.1(6) | 21(3) | | | | |
| 1212.0(4) | 64(3) | | | | |
| 1233.5(4) | 91(3) | | | | |
| 1314.5(4) | 110(3) | | | | |

* Doublet

Table 4.3: Transition energies $E_i$, efficiency corrected relative intensities $I_\gamma$ and angular intensity ratios from $\gamma$-ray singles data correlated with the $\alpha$ decay of the $^{155m2}$Lu$_{(25/2^-)}$ state. Angular intensity ratios of transitions in $^{157}$Hf are 0.81(1) for a dipole ($9/2^- \rightarrow 7/2^-$) and 0.93(4) for a quadrupole ($13/2^- \rightarrow 9/2^-$, $17/2^- \rightarrow 13/2^-$ and $21/2^- \rightarrow 17/2^-$). Lack of distinction between dipole and quadrupole transitions render multipolarity assignments inconclusive.

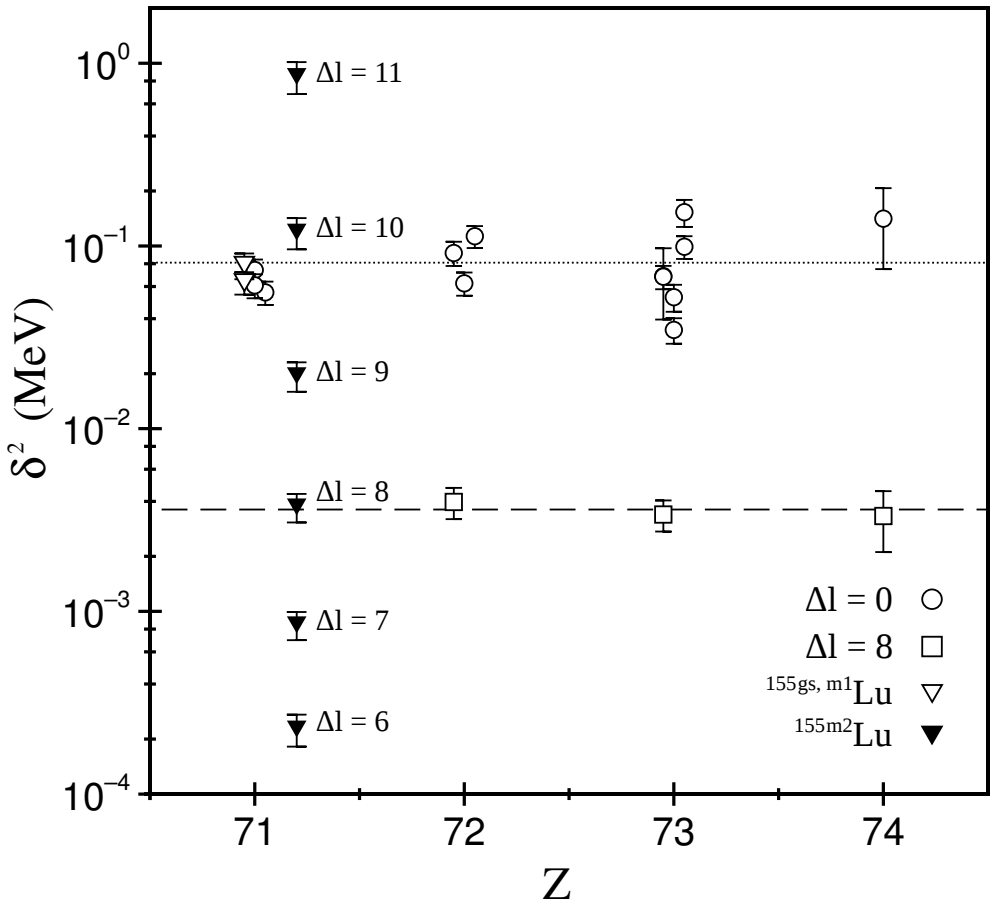


Figure 4.12: Reduced decay width $\delta^2$ as a function of proton number. Values of $\delta^2$ for the $^{155m2}\mathrm{Lu}_{(25/2^-)}$, carrying different angular momenta, have been calculated using the method described in Chapter 2. Known decays carrying $\Delta l = 0, 8$ have been used to obtain a reference for favoured and hindered decays respectively. A value of $\Delta l = 8$ for the $^{155m2}\mathrm{Lu}_{(25/2^-)}$ state is consistent with other hindered decays in the region of the nuclear chart.

has been contested based on the coincidences shown in Figure 4.15, which indicate that although the 1076 keV transition is coincident with 798 keV transition, it is not coincident with the 212 keV transition. The arrangement proposed in this work places the 798 keV transition such that it is fed by both the 212 and 1076 keV transitions. This is reinforced by the absence of a 545 keV peak in coincidence with the 212 keV transition and has the effect of placing the 300, 354, 443 and 709 keV transitions rather rigidly.

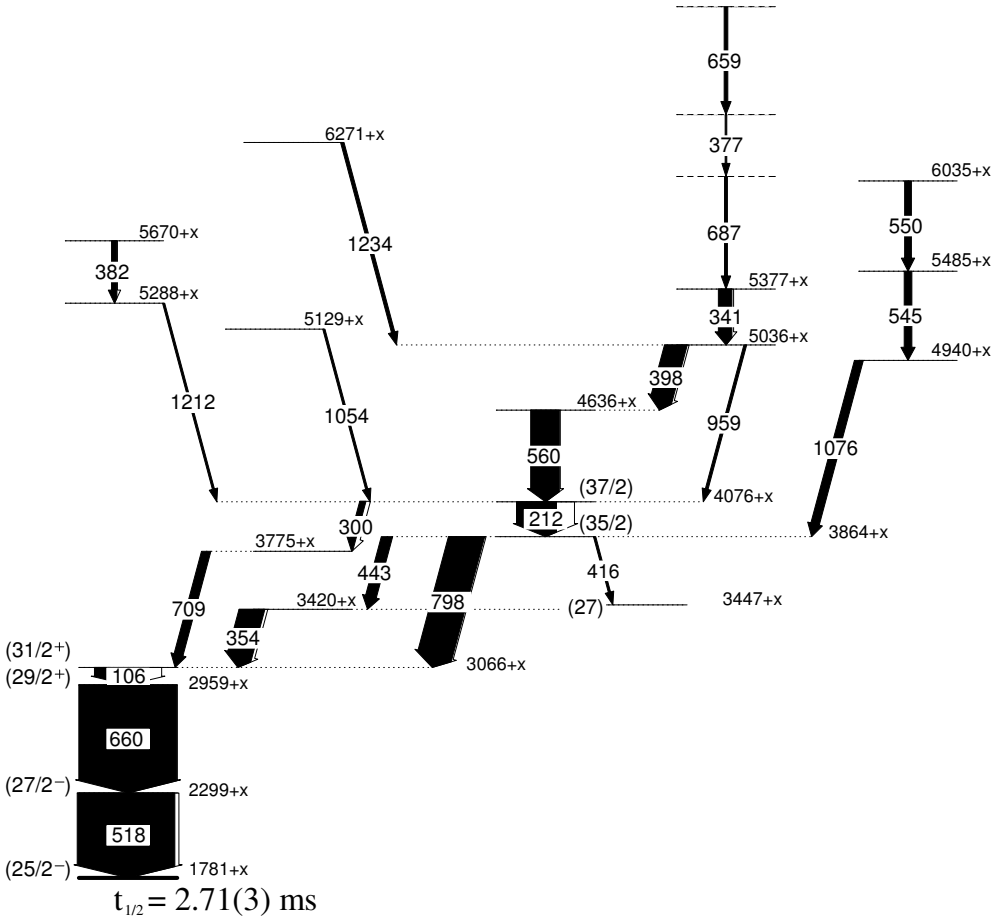


Figure 4.13: A level scheme of transitions feeding the $^{155m2}\mathrm{Lu}_{(25/2^-)}$ state.

In order to satisfy coincidences with the 382 keV transition, the placement of the 106 keV transition is limited to the lower part of the level scheme. The lifetime for a state emitting a transition of this energy with E2 multipolarity would be expected to far exceed the the time that the nucleus will be at the target position, limiting this transition to be of a dipole nature. Furthermore, the internal conversion corrected intensity for an E1 transition is considerably lower than would be required of a transition in the most intense decay path, lower in the level scheme than the 560 keV transition. Based on these expected values, shown in Table 4.4, the 106 keV transition is assigned an M1 multipolarity and placed above the 660 keV transition.

The structure immediately above the 212 keV transition has been deduced from

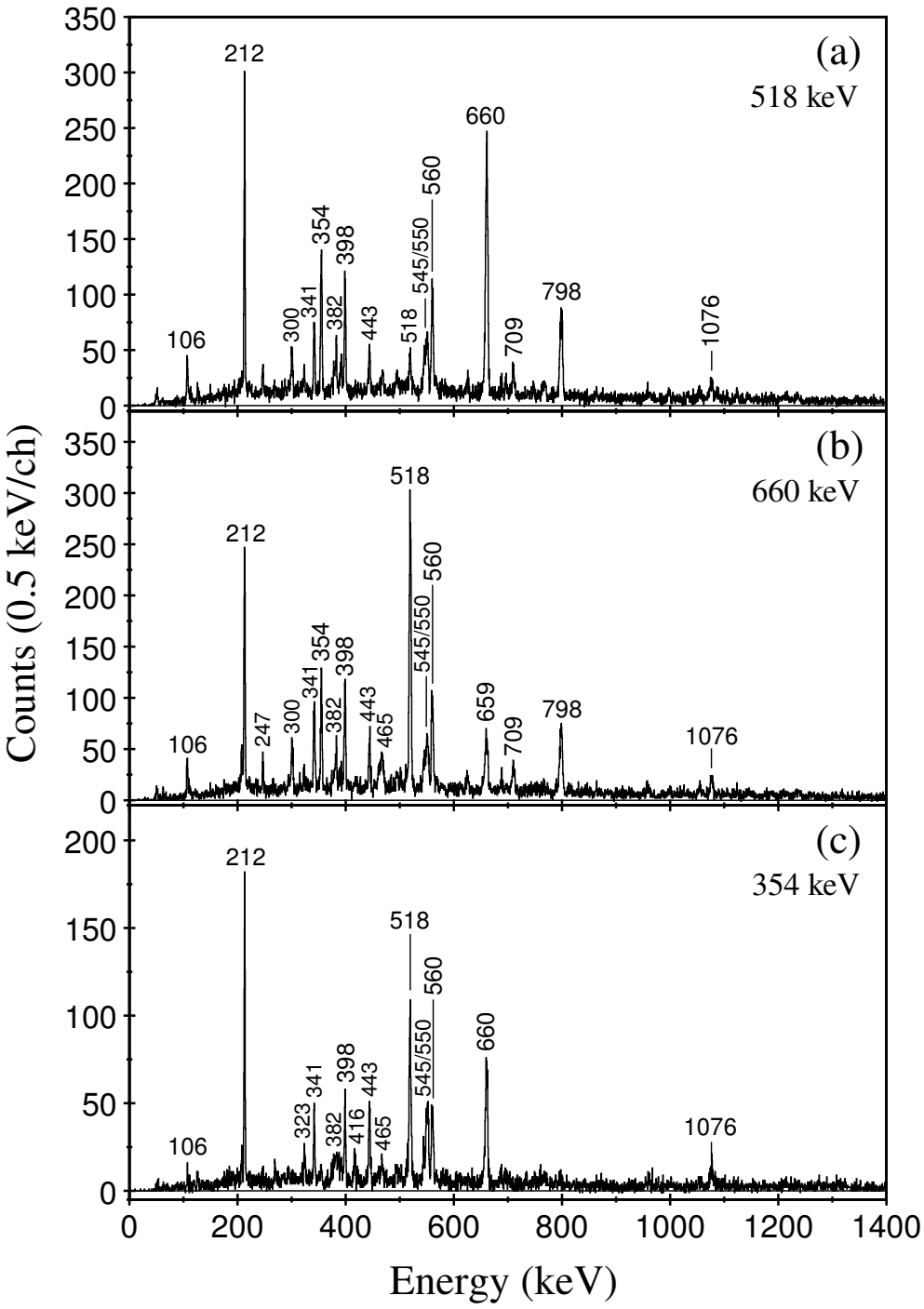


Figure 4.14: Gamma-ray coincidence spectra generated from a $^{155m2}\mathrm{Lu}_{(25/2^-)}$ $\alpha$-decay correlated matrix. **(a)** Spectrum in coincidence with the 518 keV transition. **(b)** Spectrum in coincidence with the 660 keV transition. **(c)** Spectrum in coincidence with the 354 keV transition.

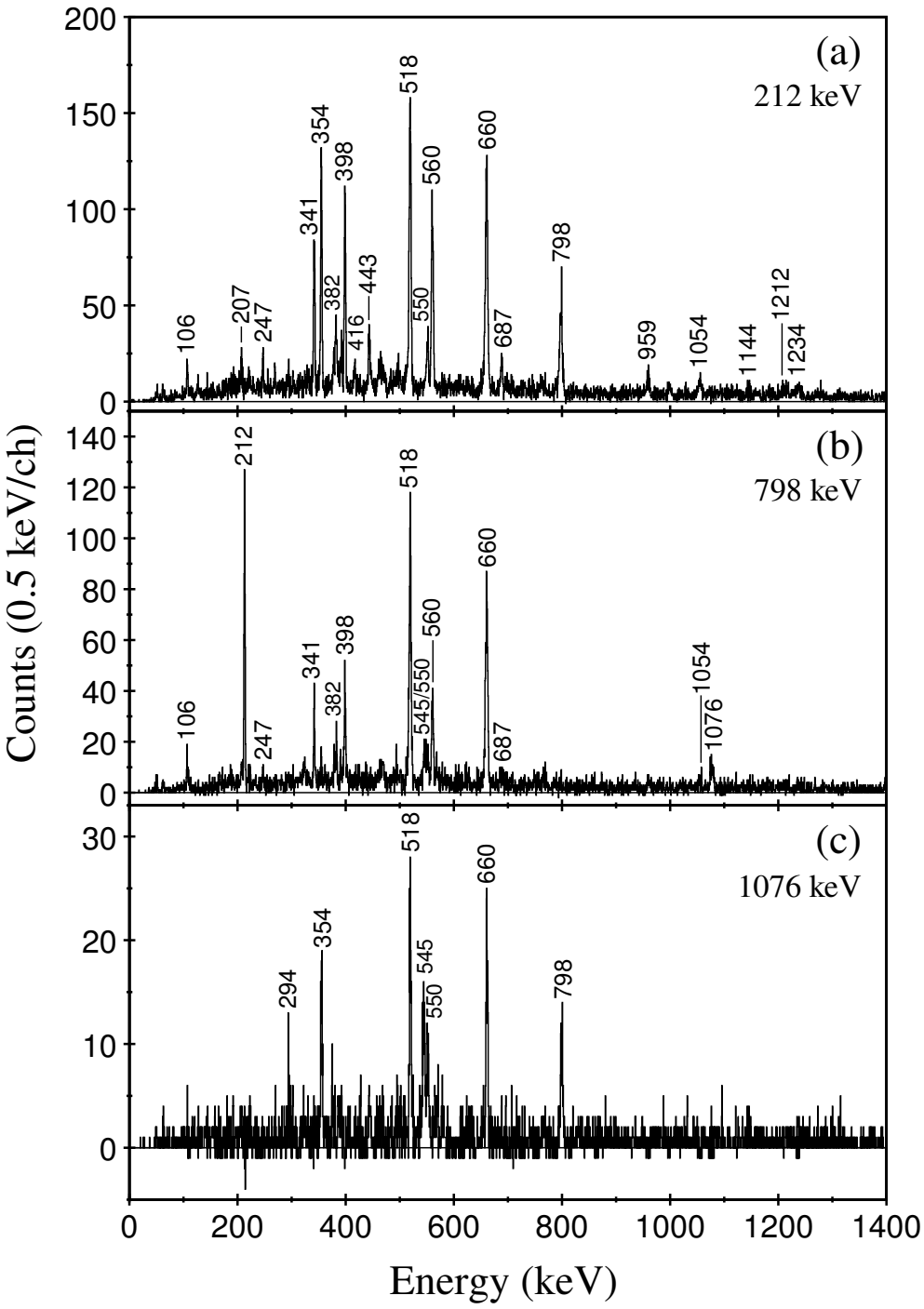


Figure 4.15: Gamma-ray coincidence spectra generated from a $^{155m2}\mathrm{Lu}_{(25/2^-)}$ $\alpha$-decay correlated matrix. **(a)** Spectrum in coincidence with the 212 keV transition. **(b)** Spectrum in coincidence with the 798 keV transition. **(c)** Spectrum in coincidence with the 1076 keV transition.

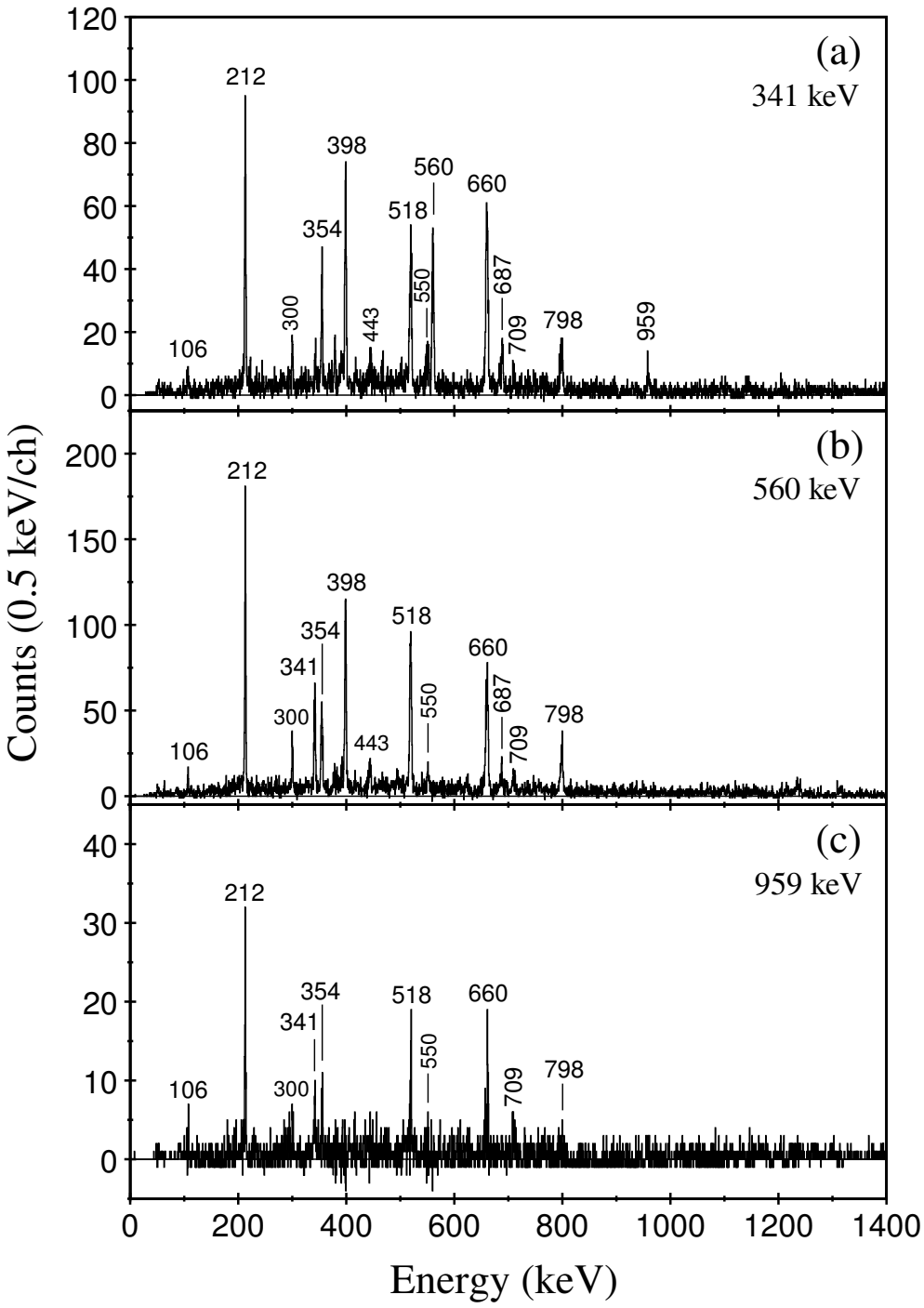


Figure 4.16: Gamma-ray coincidence spectra generated from a $^{155m2}\mathrm{Lu}_{(25/2^-)}$ $\alpha$-decay correlated matrix. **(a)** Spectrum in coincidence with the 341 keV transition. **(b)** Spectrum in coincidence with the 560 keV transition. **(c)** Spectrum in coincidence with the 959 keV transition.

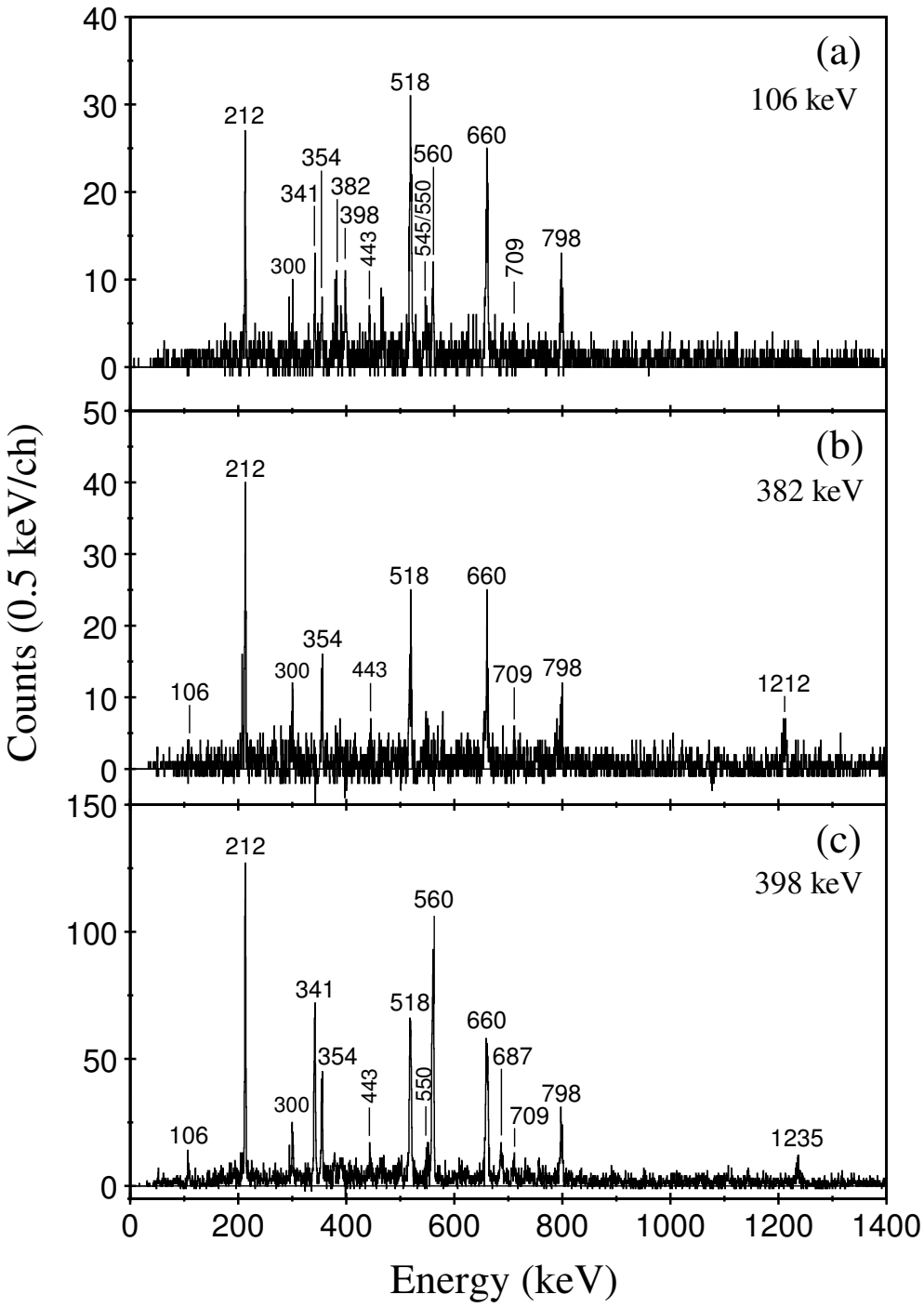


Figure 4.17: Gamma-ray coincidence spectra generated from a $^{155m2}\mathrm{Lu}_{(25/2^-)}$ $\alpha$-decay correlated matrix. **(a)** Spectrum in coincidence with the 106 keV transition. **(b)** Spectrum in coincidence with the 382 keV transition. **(c)** Spectrum in coincidence with the 398 keV transition.

| Multipolarity | Internal conversion coefficient | I(Icc corrected) | Weisskopf $T_{1/2}$ (s) |
|---|---|---|---|
| n/a | No internal conversion | 165 | n/a |
| E1 | 0.3 | 215 | $1.90\times10^{-13}$ |
| **M1** | 3.1 | **678** | $1.83\times10^{-11}$ |
| E2 | 2.7 | 608 | $8.02\times10^{-7}$ |
| M2 | 27.4 | 4683 | $7.71\times10^{-5}$ |
| E3 | 49.9 | 8399 | 5.13 |
| M3 | 200.2 | 33198 | $4.94\times10^{2}$ |

Table 4.4: Table of internal conversion [41] and efficiency corrected intensities and Weisskopf estimates for the 106 keV transition. Weisskopf estimates limit it to having a dipole nature. Coincidences with the 382 and 398 keV transitions require that it resides at lower excitation energy than either transition with more intensity than would accompany an E1 transition. As such, the 106 keV has been assigned an M1 multipolarity and has been placed according to its internal conversion corrected intensity.

the coincidence spectra shown in Figure 4.16 and Figure 4.17, which indicate that the 959 keV transition by-passes the 398 and 560 keV transitions.

Angular intensity ratios have been obtained for a number of transitions feeding the $^{155m2}\mathrm{Lu}_{(25/2^-)}$ state and compared with known transitions of known multipolarity in $^{157}$Hf [42]. The ratio of $\gamma$-ray peaks in RDT singles spectra recorded in detectors at angles of $157.6^o$ and $94.16^o$ have been used to obtain the angular intensity ratios. The uncertainties in the majority of these measurements make them insufficient for meaningful multipolarity assignments. As such, consultation of systematic trends, as discussed in Section 4.2, proves to be the most reliable way of assigning multipolarities in this work.

## 4.2 Discussion

The spectroscopy performed in Section 4.1 has led to the revision of the published $^{155}$Lu level scheme. A number of configurations associated with these levels will be deduced and their impact on the evolution of nuclear structure will be discussed in

this section.

### 4.2.1 Nucleon configurations of low-lying states

The $^{155}$Lu nucleus has seven valence protons ($Z = 71$) and two valence neutrons ($N = 84$). Low-lying states in $^{155}$Lu are based on the coupling of these valence particles. The available proton orbitals are $3s_{1/2}$, $2d_{3/2}$ and $1h_{11/2}$. Prior to this work, the 5584 and 5655 keV $\alpha$ decays have been assigned to states built on protons in the $d_{3/2}$ and $h_{11/2}$ orbitals, respectively [31]. It has been suggested that the $[\pi d_{3/2}]_{3/2^+}$ configuration is the ground state and the $[\pi h_{11/2}]_{11/2^-}$ state is a metastable state at higher excitation energy [30, 43]. States above the $^{155}$Lu$_{(3/2^+)}$ and $^{155m1}$Lu$_{(11/2^-)}$ states are likely to be based on the coupling of the odd proton to an aligned neutron pair. No transitions have been observed feeding the $^{155}$Lu$_{(3/2^+)}$ state, in this work or previously, and so nothing can be confirmed with regard to the behaviour of a possible $\pi d_{3/2} \otimes \nu(f_{7/2})^2$ configuration.

Transitions feeding the $^{155m1}$Lu$_{(11/2^-)}$ state have been reported [4, 32] and were considered to depopulate levels of spins and parities $(15/2^-)$, $(19/2^-)$ and $(23/2^-)$, corresponding to $\pi h_{11/2} \otimes \nu(f_{7/2})^2$ configuration. However, of these three transitions only two have been confirmed in this and other work [4], thus the fully aligned $[\pi h_{11/2} \otimes \nu(f_{7/2})^2]_{23/2^-}$ state had not been observed prior to this work. The origin of the unconfirmed transition has been proven to be miscorrelated $\gamma$ rays from $^{157}$Hf.

In this work, for the first time, a third transition in the cascade feeding the $^{155m1}$Lu$_{(11/2^-)}$ state has been observed. The absence of angular distributions to determine the multipolarities of these low-lying transitions prevents experimental verification of the spins and parities assigned to these states. Some perspective regarding these assignments can be obtained by comparing this data with neighbouring $N = 84$ odd-$A$ nuclei.

Energy level systematics of the $N = 84$ isotones are shown in Figure 4.18. The

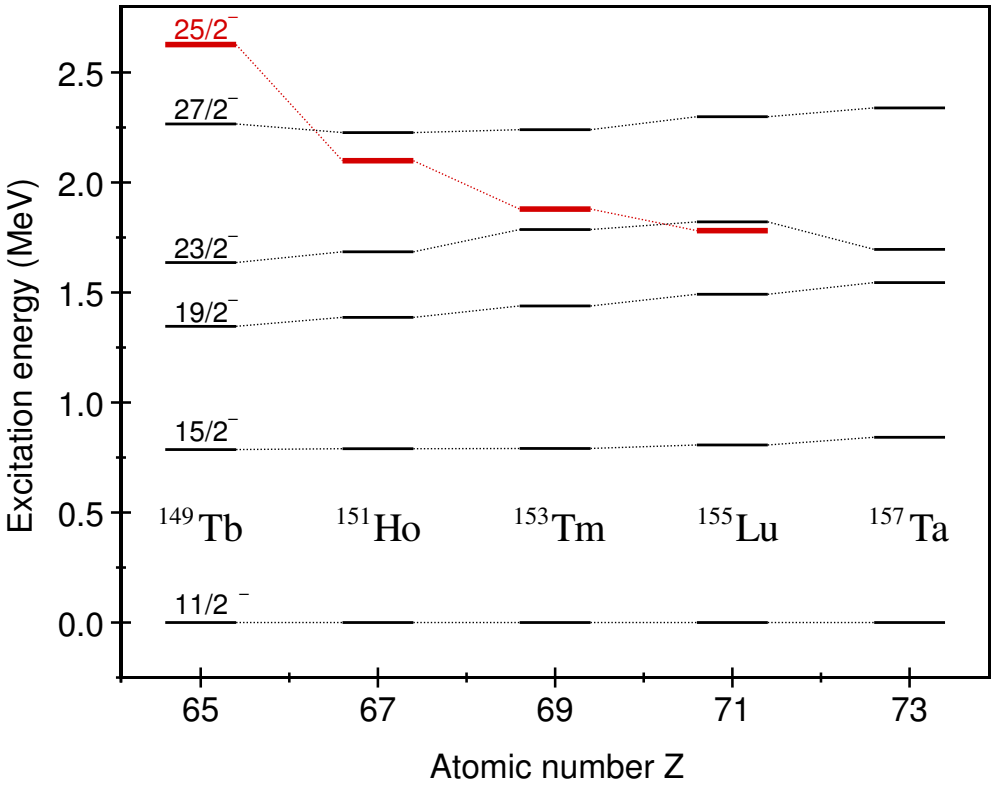


Figure 4.18: Systematics of odd-$A$ $N = 84$ isotones neighbouring $^{155}$Lu, relative to the $11/2^-$ state. The $25/2^-$ state decreases in excitation energy with increasing $Z$ [37, 39, 44, 45].

excitation energies of the $15/2^-$, $19/2^-$ and $23/2^-$ states, relative to the $11/2^-$ state, are constant across the isotones, which is indicative of a common underlying structure. This suggests that these spin and parity assignments can be applied to the corresponding states in $^{155}$Lu. These states are expected to be based on the $\pi h_{11/2} \otimes \nu(f_{7/2})^2$ configuration, which is fully aligned at $23/2^-$. No additional transitions feeding this structure have been observed. The excitation energy of the $(23/2^-)$ state is higher than that of the $(25/2^-)$ state. The $(25/2^-)$ state is a spin trap.

### 4.2.2 The $(25/2^-)$ isomer configuration

The $^{155m2}\mathrm{Lu}_{(25/2^-)}$ isomer is considered to be a spin isomer based on its deduced excitation energy relative to the $(23/2^-)$ state. Weisskopf estimates for M3 and E4 $\gamma$-ray multipolarities yield lifetimes of order $\sim$500 ms and $\sim$6 s, respectively. This enables $\alpha$ decay to compete with $\gamma$-ray emission resulting in the $\alpha$-decaying isomeric state observed.

The spin and parity of this state has not been unambiguously verified. Measurements of the $\delta^2$ in Section 4.1.3 suggest that $\Delta l = 8$ for the $\alpha$ decay. A parity change is not expected between the initial and final states of this decay and so $\Delta l = 8$ would be expected for either $^{155}\mathrm{Lu}_{27/2^-} \rightarrow ^{151}\mathrm{Tm}_{11/2^-}$ or $^{155}\mathrm{Lu}_{25/2^-} \rightarrow ^{151}\mathrm{Tm}_{11/2^-}$.

As with the low-lying states, the excited states in the isotones can provide insights into the structures in $^{155}$Lu. In this particular case, the excitation energies of the $^{155m2}\mathrm{Lu}_{(25/2^-)}$ isomer and the next excited state follow the trends of the isotones remarkably well if their spins and parities are taken to be $25/2^-$ and $27/2^-$, respectively, as shown in Figure 4.18.

A particularly interesting feature of Figure 4.18 is the lowering in excitation energy of the $25/2^-$ state relative to the $27/2^-$ state with increasing proton number, which is eventually responsible for its isomerism in $^{155}$Lu. This has been discussed in previous work on the $N = 84$ isotones $^{151}$Ho and $^{153}$Tm [38, 39] with the view that both the $25/2^-$ and $27/2^-$ states are of a $\pi h^n_{11/2} \otimes \nu f_{7/2} h_{9/2}$ configuration where the proton seniority $n = 1$ for the $27/2^-$ state (with magnetic substate occupation $m = +11/2$) and $n = 3$ for the $25/2^-$ state ($m = +11/2$, $+9/2$ and $-11/2$). The lowering in excitation energy of the $25/2^-$ state has been attributed to a strong $[\pi h_{11/2}, \nu h_{9/2}]_{1^+}$ interaction [38,39], which will be discussed further in Section 4.2.3.

### 4.2.3 Systematic trends of low-lying states across $N = 84$ isotones

A number of features present in the systematic trends shown in Figure 4.18 enable conclusions to be drawn regarding the evolution of single-particle structure approaching the proton drip line. The rather constant excitation energies of states based on the $\pi h_{11/2} \otimes \nu(f_{7/2})^2$ with increasing $Z$ is indicative of both a neutron dominance of single-particle structures and only limited interaction between the $f_{7/2}$ neutrons and $h_{11/2}$ protons.

The lowering in energy of the $(25/2^-)$ state, in the $\pi h^3_{11/2} \otimes \nu f_{7/2} h_{9/2}$ configuration, with increasing $Z$ can be attributed to the inclusion of additional protons into the system. As no proton pairs are broken in order to achieve this state, and as the $f_{7/2}$ neutrons appear to interact very poorly with the $h_{11/2}$ protons, an interaction between the $h_{9/2}$ neutron and $h_{11/2}$ protons is an appropriate mechanism to account for this lowering in excitation energy. A $[\pi h_{11/2}, \nu h_{9/2}]_{1^+}$ interaction has been suggested to account for the lowering of states in $N = 83$ isotones [36] and this interpretation has been adopted for $N = 84$ isotones [38, 39] to account for the lowering of the $(25/2^-)$ state. The interaction between the $h_{9/2}$ neutron and protons in the $h_{11/2}$ orbital is strong due to their overlapping wavefunctions [46]. This interaction is more probable with increasing proton number.

The $[\pi h_{11/2}, \nu h_{9/2}]_{1^+}$ interaction is rather specific and, in the case of the $(25/2^-)$ state, the possibility of other interactions between the $h_{9/2}$ neutrons and $h_{11/2}$ protons is presented. In particular, the $[\pi(h_{11/2})_{9/2}, \nu h_{9/2}]_{0^+}$ coupling would allow for an identical population of $m$-substates. However, the trend displayed by the $(27/2^-)$ state, in the $\pi h_{11/2} \otimes \nu f_{7/2} h_{9/2}$ configuration, is rather constant, similar to the low-lying $\pi h_{11/2} \otimes \nu(f_{7/2})^2$ states for which the protons and neutrons interacted only weakly. The interaction lowering the $(25/2^-)$ state with increasing $Z$ must not be

present in the $(27/2^-)$ state.

A possible explanation for the trend of the $(27/2^-)$ state is that the assigned configuration is incorrect and the $h_{9/2}$ neutron orbital is not populated, resulting in the removal of the strong interaction between the $h_{11/2}$ protons and $h_{9/2}$ neutrons. However, alternative configurations are difficult to construct and a $(27/2^-)$ state in the $\pi h_{11/2} \otimes \nu f_{7/2} h_{9/2}$ configuration would still be expected to exist elsewhere in the level scheme. The solution presented by introducing a specific strong $[\pi h_{11/2}, \nu h_{9/2}]_{1^+}$ interaction is that configurations facilitating this interaction will be blocked for certain states.

No protons are required to occupy the $+11/2$ substate of the $h_{11/2}$ orbital in order to generate the spin of the $(25/2^-)$ state, so a $[\pi h^2_{11/2}]_{0^+}$ pair may occupy the $m = +11/2$ and $m = -11/2$ substates, enabling the strong $[\pi h_{11/2}, \nu h_{9/2}]_{1^+}$ interaction with the $h_{9/2}$ neutron, thus lowering the energy of the state. The $(27/2^-)$ state requires that a proton occupies the $+11/2$ substate and couples parallel to the $h_{9/2}$ neutron in order to obtain the required spin.

A consequence of this is that a $[\pi h^2_{11/2}]_{0^+}$ pair cannot occupy the $m = +11/2$ and $m = -11/2$ substates as the $m = +11/2$ substate is already occupied. A spin of $27/2$ cannot be generated if the $-11/2$ substate is occupied without an additional $+11/2$ contribution, thus the $[\pi h_{11/2}, \nu h_{9/2}]_{1^+}$ interaction is cannot occur, preventing the lowering of the state. It is important to note that the blocking experienced by the $27/2^-$ states is a result of employing this specific interaction. The $[\pi(h_{11/2})_{9/2}, \nu h_{9/2}]_{0^+}$ interaction considered earlier would not be prevented by this blocking and so the constant trend of the $27/2^-$ states would not be explained. Including the $[\pi h_{11/2}, \nu h_{9/2}]_{1^+}$ interaction makes it possible to write the configurations of the $(25/2^-)$ and $(27/2^-)$ states as $[\pi(h^2_{11/2})_{10^+} \otimes \nu(f_{7/2})_{7/2^-} \otimes (\pi h_{11/2}, \nu h_{9/2})_{1^+}]_{25/2^-}$, in which the $1^+$ contribution is anti-aligned with the other contributions, and $[\pi h_{11/2} \otimes \nu f_{7/2} h_{9/2}]_{27/2^-}$.

### 4.2.4 Configurations above the $(25/2^-)$ isomer

The level scheme above the $^{155m2}\mathrm{Lu}_{(25/2^-)}$ isomer has been significantly revised in this work. Although the spins and parities of the states remain tentative, the assignments are limited by the multipolarities of transitions, which must allow for them to be in prompt coincidence at the target position.

As previously discussed, the $(25/2^-)$ isomer is considered to be in the $\pi h_{11/2}^3 \otimes \nu f_{7/2} h_{9/2}$ configuration, while the $(27/2^-)$ is in the fully-aligned $\pi h_{11/2} \otimes \nu f_{7/2} h_{9/2}$ configuration. States immediately above this are likely to be based on further neutron excitation as higher angular momentum orbitals are not available to individual protons and the energies required to break a proton pair ($\sim$800-1500 keV [45,47–49]) are not observed.

The $(29/2^+)$ and $(31/2^+)$ states have been assigned positive parities based on the likelihood that neutron occupation of the $i_{13/2}$ orbital is responsible for states at higher spin. These spin and parity assignments can be constructed with a $\pi h_{11/2} \otimes \nu f_{7/2} i_{13/2}$ configuration, which has been adopted in the $N = 84$ isotones $^{151}$Ho and $^{153}$Tm [38, 39]. A comparison of the energies of these states relative to the $27/2^-$ states across $N = 84$ isotones is shown in Figure 4.19.

Relative to the rather constant excitation energies of the $27/2^-$ states, the $(29/2^+)$ and $(31/2^+)$ states appear to decrease in excitation energy with increasing $Z$, reminiscent of the behaviour of the $25/2^-$ state. This behaviour is indicative of a configuration in which the $h_{9/2}$ neutron orbital is occupied and the $[\pi h_{11/2}, \nu h_{9/2}]_{1^+}$ interaction is present and so the $\pi(h_{11/2}^3)_{9/2} \otimes \nu h_{9/2} i_{13/2}$ configuration should not be discounted as a mechanism for obtaining the $(29/2^+)$ and $(31/2^+)$ states, which can be written $[\pi(h_{11/2}^2)_{10^+} \otimes \nu(i_{13/2})_{13/2^+} \otimes (\pi h_{11/2}, \nu h_{9/2})_{1^+}]_{31/2^+}$.

Similarities in the relative excitation energies between higher angular momentum states in $^{153}$Tm and in $^{155}$Lu may indicate that similar configurations account for structures in both isotones, however, the number of observed states in $^{153}$Tm,

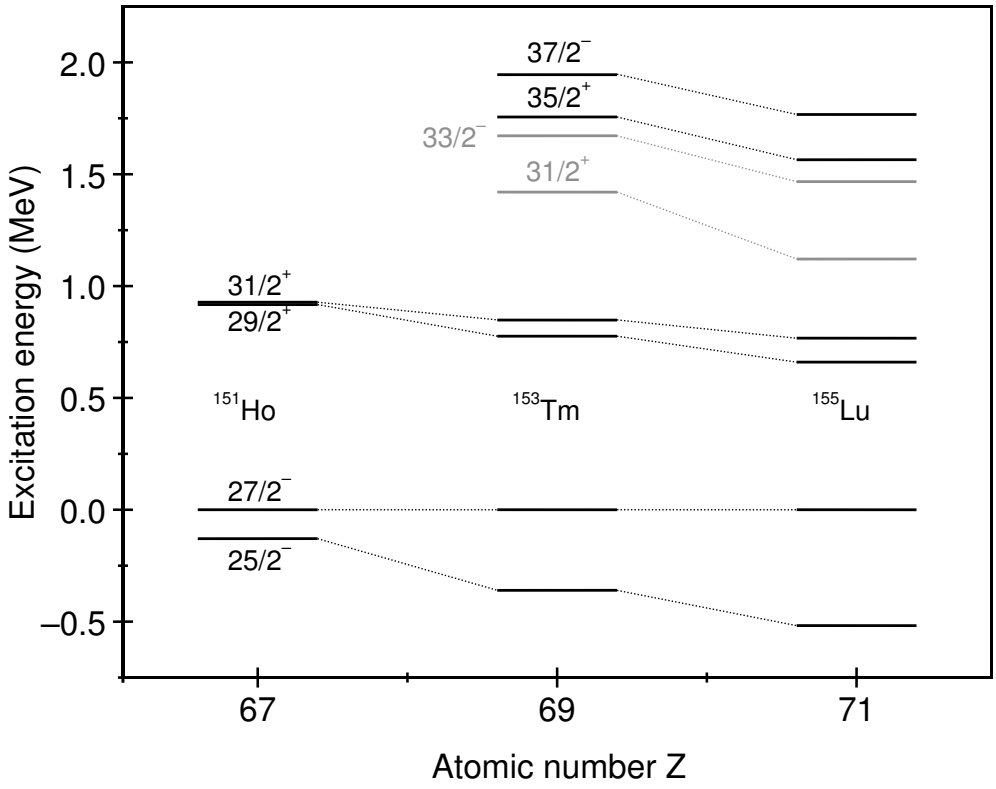


Figure 4.19: Systematics of odd-$A$ $N = 84$ isotones neighbouring $^{155}$Lu. States above $25/2^-$ are shown relative to the excitation energy of the $27/2^-$ state. States shown in grey occupy weaker decay paths to those shown in black.

combined with the absence of strong spin and parity arguments in this work make it difficult to compare states with the confidence that they are constructed from similar configurations.

The strongest decay paths observed in $^{155}$Lu, above the $(25/2^-)$ state, are shown in Figure 4.19 and are compared to levels in the strongest decay paths in $^{153}$Tm. Similarities between the $^{155}$Lu states, (35/2) and (37/2), and the $^{153}$Tm states, $35/2^+$ and $37/2^-$, suggests that they are analogous, sharing similar nucleon configurations. Configurations of states in $^{153}$Tm have been assigned based on comparisons with shell model calculations. These assignments are $[\pi h^4_{11/2} d_{3/2} \otimes \nu f^2_{7/2}]_{35/2^+}$ and $[\pi h^5_{11/2} \otimes \nu f_{7/2} h_{9/2}]_{37/2^-}$. Both cases require proton pair breaking to achieve these spins. The observation that these states are lower in $^{155}$Lu may be indicative of further

interactions between nucleons in the $\pi h_{11/2}$ and $\nu h_{9/2}$ orbitals.

The levels between $(31/2^+)$ and $(37/2)$ in $^{155}$Lu are unlikely to be based on the excitation of the remaining $f_{7/2}$ neutron into the $i_{13/2}$ orbital as they have no means of generating the required spin. As such, states above the $(31/2^+)$ state are considered to be constructed by breaking a proton pair, as expected in $^{153}$Tm.

## 4.3 Conclusions

Excited states in $^{155}$Lu have been populated in a fusion evaporation reaction and the RDT technique has been employed to identify $\gamma$-ray transitions from these states, selecting them from a large background originating from other reaction channels. These transitions have enabled a level scheme to be constructed and single-particle configurations to be assigned, as shown in Figure 4.20. No transitions have been confirmed to feed the $(3/2^+)$ state. Three transitions have been confirmed to feed the $(11/2^-)$ state including the 329 keV transition, which has been observed for the first time in this work. These transitions have been ordered based on intensity arguments and complement the constant systematic trends of the isotones, suggesting a configuration of $\pi h_{11/2} \otimes \nu(f_{7/2})^2$ maximally aligned at $23/2^-$. The identification of the $(23/2^-)$ state confirms spin isomerism as source of the $(25/2^-)$ state's long lifetime.

The level scheme above the $(25/2^-)$ isomer has been revised significantly over previous work. The absence of reliable angular distributions limits confidence in the assignment of the spins of these states, which in turn limits comparisons between isotones to states. Occupation of the $i_{13/2}$ neutron orbital has been deduced as the most likely mechanism of achieving spins up to $31/2$ and this is consistent with configurations assigned to the isotones.

States at higher excitation energy are considered to require proton pair breaking.

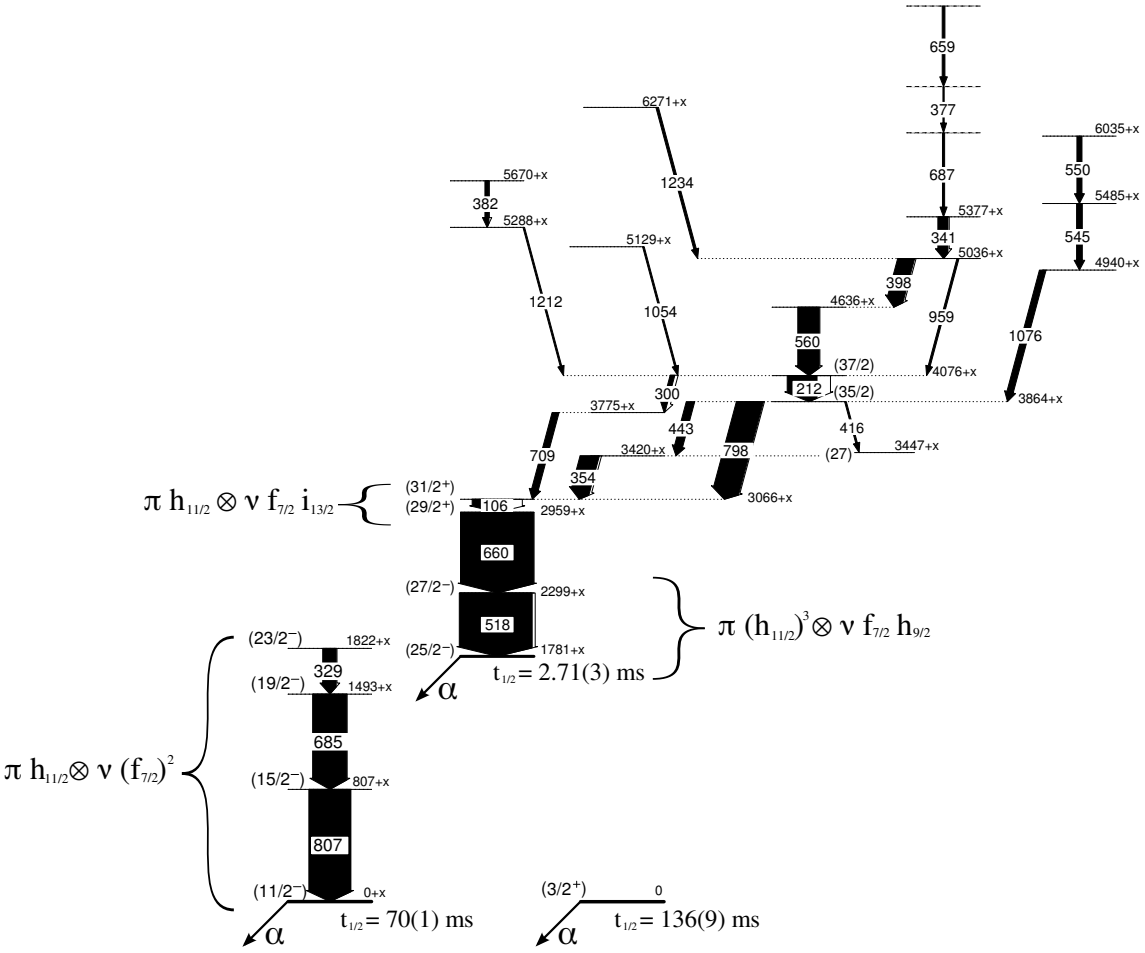


Figure 4.20: Level scheme of excited states in $^{155}$Lu based on analysis in this work.

Precise nucleon configurations of these states have not been resolved in this work.

The single particle structures observed in this work demonstrate a range of phenomena that evolve with increasing proton number. The structures based on the $\pi h_{11/2} \otimes \nu(f_{7/2})^2$ configurations are very robust to changes in the proton occupancy of the $h_{11/2}$ orbital. Such consistency across the isotones shows that very little interaction occurs between the $h_{11/2}$ protons and $f_{7/2}$ neutrons.

Structures based on the $\pi h_{11/2} \otimes \nu f_{7/2} h_{9/2}$ configuration may differ significantly with increasing proton number. The lowering in excitation energy of the $(25/2^-)$ state demonstrates a particular sensitivity of $h_{9/2}$ neutrons to the protons in the $h_{11/2}$ orbital, with the interaction strengthening as protons are added to the system. The

absence of such changes in the $(27/2^-)$ state is an indication that not all couplings of the $h_{11/2}$ protons and $h_{9/2}$ neutrons experience this strong attraction.

# Chapter 5

# First observation of excited states and radioactive decays in $^{158}$Ta

In this chapter, excited states in the proton unbound doubly-odd nucleus $^{158}$Ta, $Z = 73$ and $N = 85$, are observed for the first time. A level scheme is constructed and single-particle configurations are assigned and discussed. A new isomer with $\alpha$-decay and $\gamma$-ray branches is also observed at high spin. The $^{158}$Ta nucleus is located three neutrons above the $N = 82$ shell closure and lies beyond the proton drip line [5]. Nucleons are expected to occupy the proton $h_{11/2}$, $d_{3/2}$ and $s_{1/2}$ and neutron $f_{7/2}$, $h_{9/2}$ and $i_{13/2}$ orbitals.

Previous studies of $\alpha$-decay chains originating from $^{166}$Ir have confirmed the existence of two $\alpha$-decaying states in $^{158}$Ta [50]. The ground state is assigned a spin and parity of $(2^-)$ based on the $[\pi d_{3/2} \otimes \nu f_{7/2}]_{2^-}$ configuration and a low-lying $\alpha$-decaying isomer is assigned a spin and parity of $(9^+)$ based on the $[\pi h_{11/2} \otimes \nu f_{7/2}]_{9^+}$ configuration, analogous to $^{166}$Ir. No other states in $^{158}$Ta have been observed prior to this work.

In this work, an experiment has been performed that will enable a level scheme of excited states in $^{158}$Ta to be constructed for the first time. The experiment was

performed at the Accelerator Laboratory at the University of Jyväskylä using the apparatus described in Chapter 3. An accelerated $^{58}Ni^{11+}$ beam has been produced, with a beam energy of 255 MeV, and projected onto an enriched $^{102}$Pd target of thickness $\sim$1 mg cm$^{-2}$. The reaction

$$^{102}\mathrm{Pd}(^{58}\mathrm{Ni,pn})^{158}\mathrm{Ta}^{*}$$

produces $^{158}$Ta nuclei in excited states. It is one of many possible reaction channels. These nuclei emit $\gamma$ rays at the target position and $\alpha$ decay at the focal plane as previously described. A number of $\gamma$-ray transitions are also emitted at the focal plane.

Correlations with $\gamma$ rays in $^{158}$Ta, at both the target position and the focal plane, are made using the RDT technique to observe excited states above the known $\alpha$-decaying states. A high-spin isomer with both $\alpha$-decay and $\gamma$-ray branches is observed for the first time and is used to make correlations with the associated $\gamma$-ray transitions at the target position.

Previous studies of $N = 85$ isotones have revealed a lowering in excitation energy of states built on the $\pi h_{11/2} \otimes \nu h_{9/2}$ configuration relative to states built on the $\pi h_{11/2} \otimes \nu f_{7/2}$ configuration with increasing proton number [4]. In particular, the difference in excitation energy between the $9^+$ and $10^+$ states decreases as the proton number increases. Similar phenomena have been observed in other isotone chains in this region of the nuclear chart [36, 39]. The constructed $^{158}$Ta level scheme and assigned nucleon configurations are compared with neighbouring $N = 85$ isotones and systematic trends are discussed. These trends are interesting as they demonstrate the effects of adding an individual proton into a nuclear system at the extremes of stability.

There are a number of considerations that must be made in the study of $^{158}$Ta. The two known $\alpha$ decays in $^{158}$Ta are only $\sim$70 keV apart placing them close enough to each other that the lower energy $\alpha$ decay is located in the low energy tail of the

higher energy $\alpha$ decay, resulting in contamination. Another consideration is that as the energy difference between the $9^+$ and $10^+$ states decreases as the proton number increases [4], the difference expected in $^{158}$Ta is less that 111 keV, which is the difference observed in $^{157}$Hf. The detection efficiency of the JUROGAM spectrometer in this energy region falls significantly with decreasing transition energy. This may hinder measurements of the energy difference between these states in $^{158}$Ta in this work.

## 5.1 Results

Gamma-ray spectroscopy can be performed using both the JUROGAM array and the GREAT spectrometer, allowing for spectroscopy of transitions emitted at the target position and of transitions emitted at the focal plane. The RDT technique makes it possible to separate transitions belonging to $^{158}$Ta from the high $\gamma$-ray background using its characteristic $\alpha$ decays to select a specific reaction channel. The decays observed in this experiment are shown in Figure 4.2.

### 5.1.1 Identification of $^{158}$Ta $\gamma$ rays

The two known $\alpha$ decaying states in $^{158}$Ta [40, 50] are tentatively assigned spins and parities of $(2^-)$ and $(9^+)$ and their properties are listed in Table 5.1. Spectra of $\gamma$ rays correlated with the $\alpha$ decays from the $(2^-)$ and $(9^+)$ states are shown in Figure 5.1.

| Nucleus | $E_\alpha$ (keV) | $t_{1/2}$ (ms) | $J_i^\pi \rightarrow J_f^\pi$ |
|---|---|---|---|
| $^{158}$Ta$_{(2^-)}$ | 5969(8) | 46(4) | $(2^-) \rightarrow (2^-)$ |
| $^{158m1}$Ta$_{(9^+)}$ | 6046(4) | 35(1) | $(9^+) \rightarrow (9^+)$ |

Table 5.1: Known $\alpha$ decays from $^{158}$Ta [40, 50].

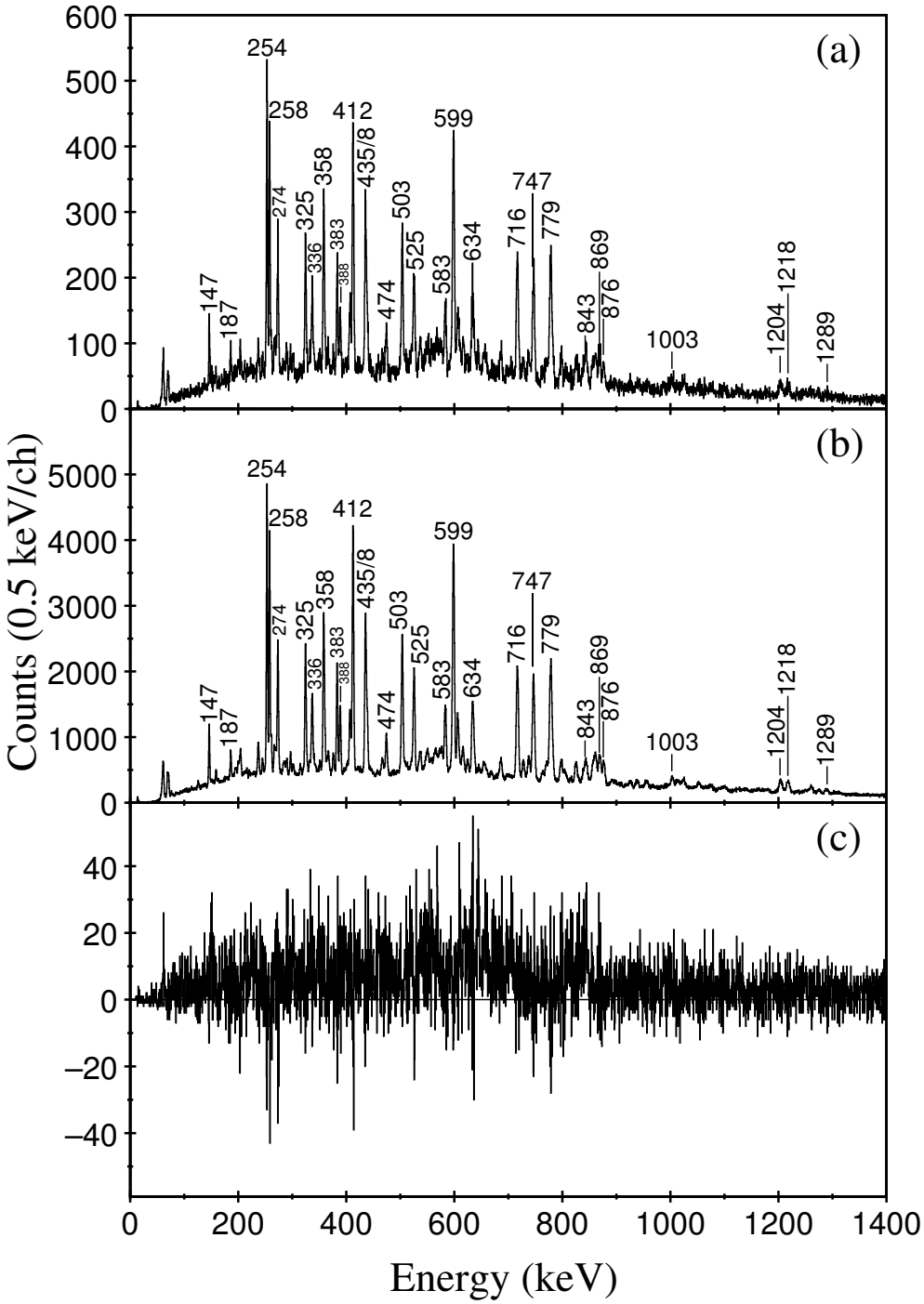


Figure 5.1: Energy spectra of $\gamma$ rays obtained using the RDT technique tagging on decays from **(a)** the $(2^-)$ state with a 230 ms correlation time and **(b)** the $(9^+)$ state with a 175 ms correlation time. **(c)** A difference spectrum in which (b) is normalised and subtracted from (a). No clear features remain.

The spectra in Figure 5.1 indicate that tagging on either $\alpha$ decay will return the same $\gamma$ rays. Possible explanations for this observation are that both decays originate from the same state, that both states are fed by the same transitions, with a linking transition between them, or that contamination occurs in the RDT process.

No linking transition between the two $\alpha$ decaying states is observed, as indicated by the absence of features in Figure 5.1(c). Previous work on decays from $^{166}$Ir [50] indicates that both decays originate from separate states as they belong to separate decay chains. This reinforces the expectation that an unobserved linking transition between the two states would not exist.

This leaves the most probable explanation for the similarities between the tagged spectra to be contamination during the RDT process. This is further supported by the proximity of the $\alpha$-particle energies to each other. The $\alpha$ decay from the $^{158}\mathrm{Ta}_{(2^-)}$ state has a relatively low intensity due to the favourable population of higher spin states when using fusion evaporation reactions. It resides in the low-energy tail of the $\alpha$ decay from the $^{158m1}\mathrm{Ta}_{(9^+)}$ state, which results in contamination peaks from the $^{158m1}\mathrm{Ta}_{(9^+)}$ decay correlation dominating the spectrum.

In order to remove the contaminant peaks from the tagged $^{158}\mathrm{Ta}_{(2^-)}$ spectrum, the tagged $^{158m1}\mathrm{Ta}_{(9^+)}$ spectrum can be treated as a background spectrum. Normalising a peak in the background spectrum to a peak in the contaminated $^{158}\mathrm{Ta}_{(2^-)}$ spectrum and subtracting has the effect of removing the contaminant peaks. Due to the absence of well defined peaks in Figure 5.1(c), no transitions have been placed upon the $^{158}\mathrm{Ta}_{(2^-)}$ state.

In addition to the $\gamma$ rays observed at the target position, isomer-delayed transitions have been observed in the focal plane germanium detectors, see Figure 5.2(a), which makes it possible to deduce that there is an isomeric state present. This isomeric state is long-lived enough for recoiling nuclei to reach the focal plane before

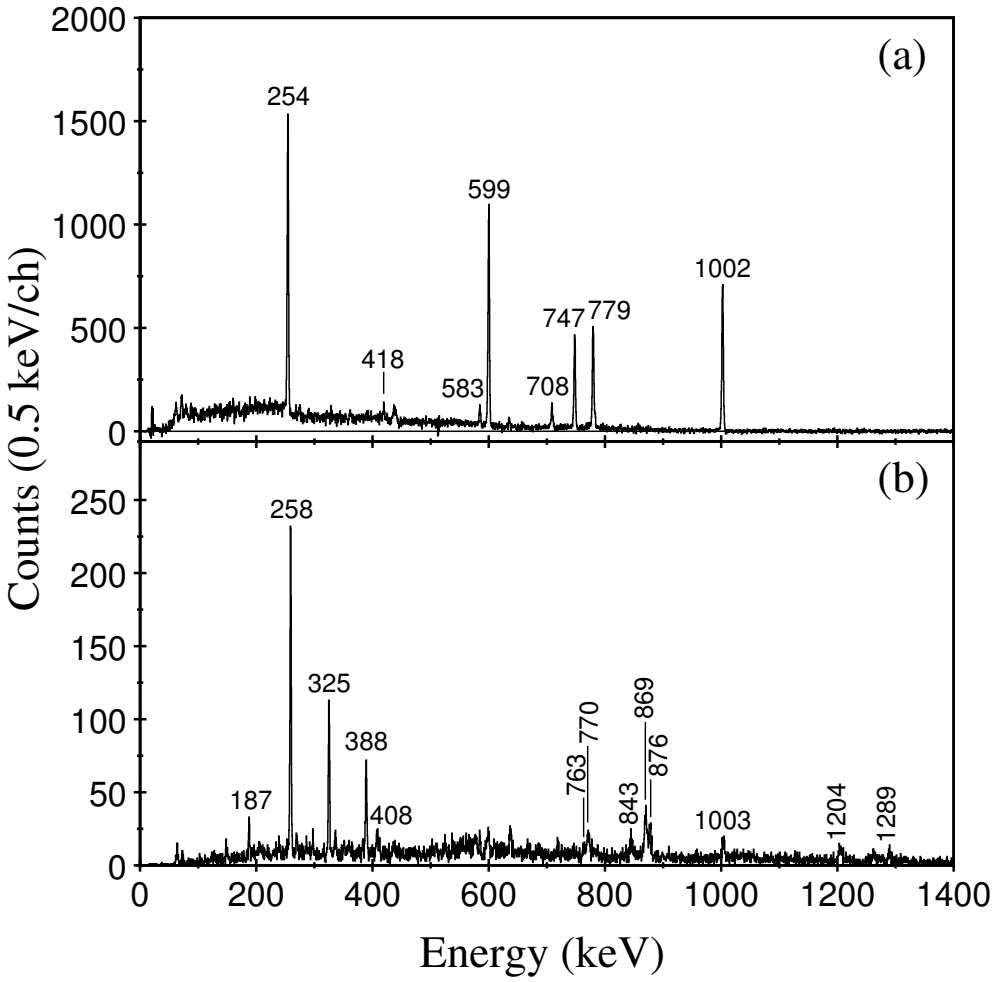


Figure 5.2: **(a)** Energy spectra of $\gamma$ rays from the focal plane clover detector detected within 30 $\mu$s of the implantation of a recoil identified by the $^{158m1}$Ta$_{(9^+)}$ decay. A background subtraction has been performed by subtracting data collected for 30 $\mu$s of an uncorrelated DSSD event for every identified event. **(b)** Energy spectra of $\gamma$ rays from the target position correlated with both a recoil identified by the $^{158m1}$Ta$_{(9^+)}$ decay and $\gamma$-ray transitions observed at the focal plane in (a), isolating transitions feeding the high-spin isomeric state.

they decay. Decay paths that do not populate this isomer are present, allowing for a number of transitions to appear both at the target position and the focal plane.

Transitions seen exclusively at the target position must not follow decays from the isomeric state. Transitions seen exclusively at the focal plane must follow the decay of the isomeric state. Transitions seen at both positions must be placed in such a way that they occur in both decay paths that depopulate the isomer and

decay paths that bypass the isomer.

Transitions that feed the high-spin isomer can be identified by specifying that both the $\alpha$ decay from the $^{158m1}\text{Ta}_{(9^+)}$ state and a delayed transition following the high-spin isomeric state are observed. These transitions are shown in Figure 5.2(b).

### 5.1.2 Transitions below the high-spin isomer

The presence of a new high-spin isomeric state above the $(9^+)$ state provides an opportunity to specifically study the structures at the base of the level scheme. The half-life of this state has been obtained by measuring the time differences between implanted recoils in the DSSDs and identified $^{158}$Ta $\gamma$ rays in the focal plane clover detector. A decay curve fitted to these data is shown in Figure 5.3 and yields a measured half-life of $t_{1/2} = 6.1(1)$ $\mu$s.

Detailed structural information can be obtained for this region of the level scheme using coincidence analysis, as described in Section 3.4.6, which allows for common decay paths between $\gamma$ rays to be identified. Each decay path by which the nucleus de-excites reveals important structural information.

Coincidence analysis at the target position can be performed using fold 2 or higher coincidences from the JUROGAM spectrometer. At the focal plane no such array exists, however, $\gamma$-ray coincidences can still be obtained between the clover and planar detectors and between the individual clover crystals in the GREAT spectrometer.

As the majority of the $\gamma$ rays observed at the focal plane lie above the energy range of the planar detector, coincidences between the individual crystals of the clover detector have been used to establish the majority of the level scheme below the new high-spin isomer. A selection of these coincidences are shown in Figure 5.4.

The gated spectra shown in Figure 5.4 indicate that the 746 and 779 keV transitions are not in coincidence with each other but they are coincident with the 254,

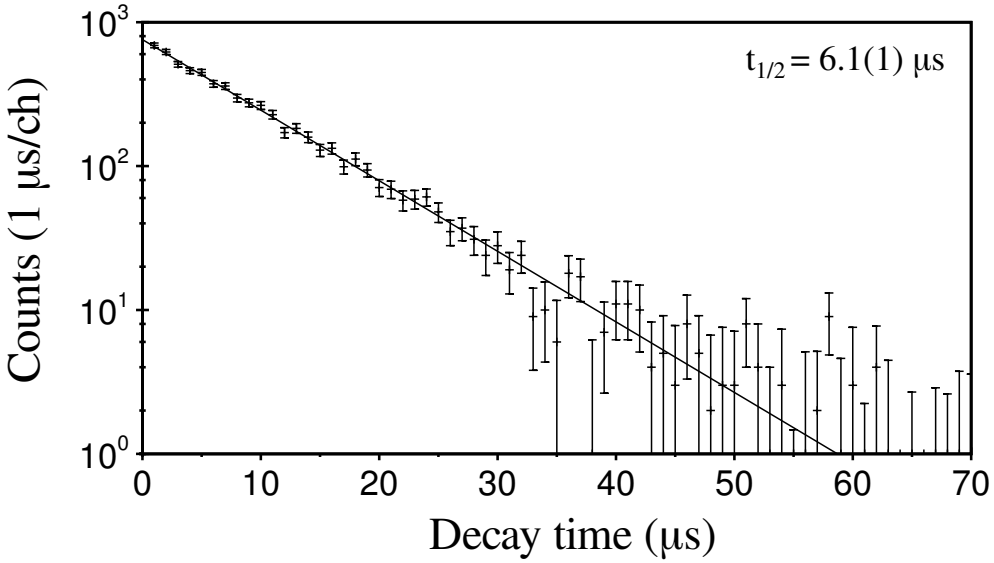


Figure 5.3: The time between recoil implantation and 1002 keV $\gamma$ ray detection at the focal plane. The fitted half-life is 6.1(1) $\mu$s.

599 and 1002 keV transitions. A consequence of this is that a level scheme is difficult to construct without introducing an unobserved transition to account for the energy difference between parallel 746 and 779 keV transitions. The most likely explanations for such a transition to go unobserved are that it resides in an energy region of low detection efficiency or that it has a high internal conversion coefficient resulting in a diminished $\gamma$-ray peak intensity.

Coincidences between the clover and planar detectors reveal a possible candidate for such a transition. A comparison of the known tantalum X-ray intensity ratio between the $K_\alpha$ and $K_\beta$ peaks with ratios obtained from the planar detector has identified a discrepancy, as shown in Figure 5.5. Coincidences in the planar detector, with a 746 keV transition detected in the clover detector, reveal a spectrum in which the intensity ratio of the $K_\alpha$ to the $K_\beta$ is inconsistent with known data due to a significantly larger $K_\beta$ peak intensity. This inconsistency is not observed in coincidence with the 779 keV transition, indicated in Table 5.2, thus the possibility is presented that a 66 keV $\gamma$-ray transition exists in coincidence with the 746 keV

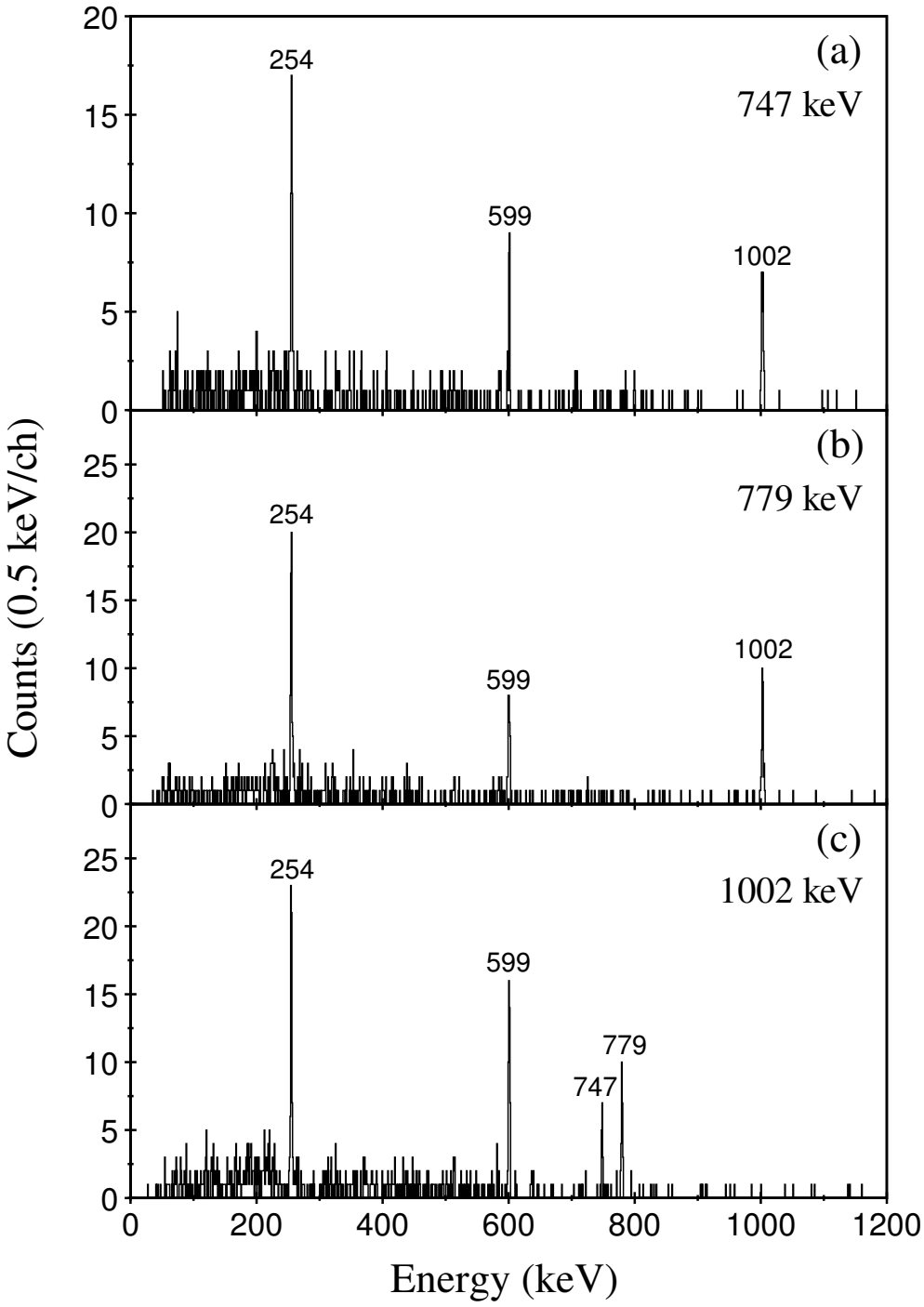


Figure 5.4: Gamma-ray coincidences between focal plane clover crystals that occur within 50 ns of each other detected within 30 $\mu$s of implantation of a recoil identified by the $\alpha$ decay from the $^{158m1}\mathrm{Ta}_{(9^+)}$ state which occurs within a correlation time of 175 ms of the recoil implantation. **(a)** Spectrum in coincidence with the 747 keV gate. **(b)** Spectrum in coincidence with the 779 keV gate. **(c)** Spectrum in coincidence with the 1002 keV gate. The 747 and 779 keV transitions do not appear in coincidence.

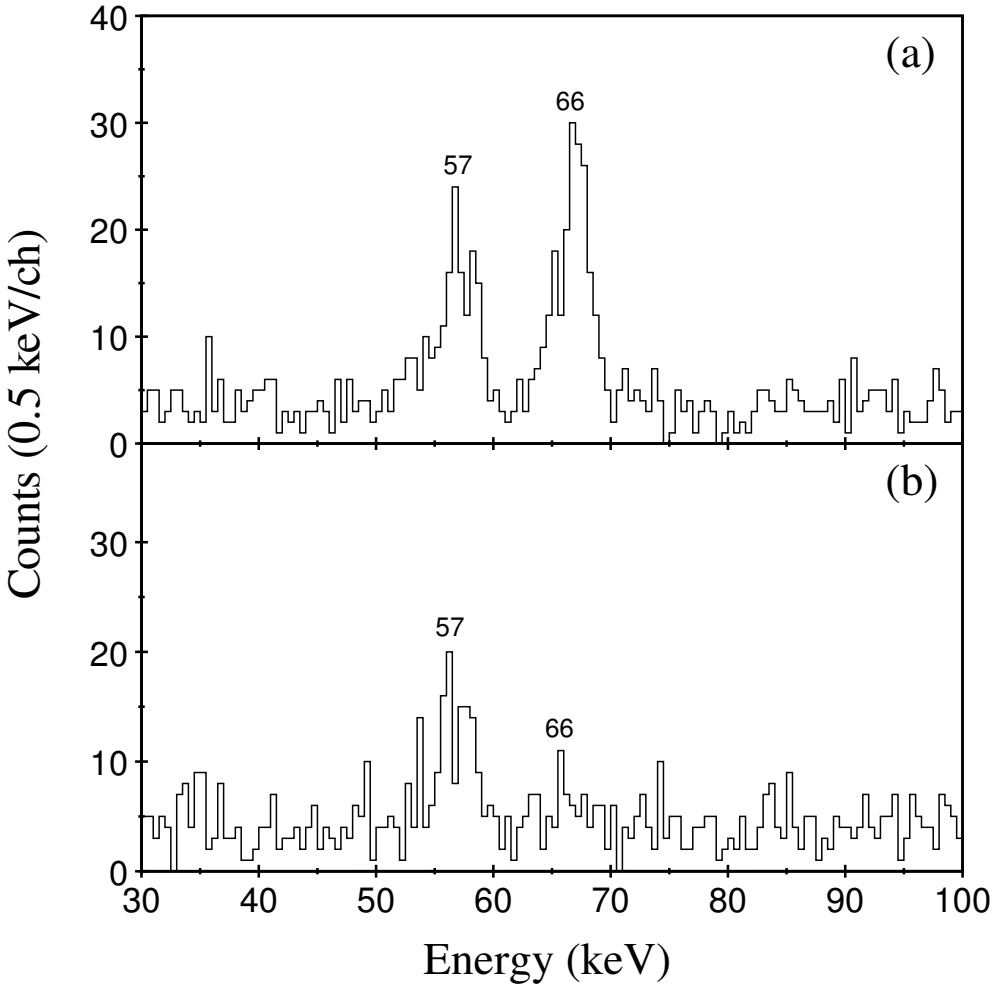


Figure 5.5: Energy spectra of tantalum X-rays in the focal plane planar detector detected within 50 ns coincidence of transitions detected in the focal plane clover detector and within 30 ms of implantation of a recoil identified by the $\alpha$ decay from the $^{158m1}$Ta$_{(9^+)}$ state which occurs within a correlation time of 175 ms of the recoil implantation. **(a)** X-rays in coincidence with a 747 keV transition reveal an intense K$_\beta$ peak, indicating the presence of a 66 keV $\gamma$-ray transition overlapping the K$_\beta$ peak. **(b)** X-rays in coincidence with a 779 keV transition show no such irregularity. The intensity balance between the K$_\alpha$ and K$_\beta$ lines is as expected for tantalum.

transition, which overlaps the K$_\beta$ X-ray peak.

If the 66 keV transition is placed in coincidence with the 746 keV transition in a branch parallel to the 779 keV transition then there remains an energy difference of 34 keV between the two decay paths. Experimentally this presents a problem as the efficiency of the planar detector at such low energies would result in poor

| | Intensity (%) | | Intensity ratio |
|---|---|---|---|
| | $K_\alpha$ | $K_\beta$ | $K_\alpha/K_\beta$ |
| Ta X-rays [2] | 75.1 ± 1.2 | 19.8 ± 0.2 | 3.8 ± 0.1 |
| | Intensity | | Intensity ratio |
| | $K_\alpha$ | $K_\beta$ | $K_\alpha/K_\beta$ |
| 747 gated | 111.7 ± 13.0 | 158.6 ± 15.3 | 0.7 ± 0.1 |
| 779 gated | 91.0 ± 12.4 | 27.5 ± 10.5 | 3.3 ± 1.3 |

Table 5.2: Expected relative X-ray intensities are compared to those measured in coincidence with 747 and 779 keV $\gamma$-ray transitions at the focal plane. The ratio of the $K_\alpha$ to $K_\beta$ peaks in coincidence with the 747 keV transition is inconsistent with the published data. Significant additional strength in the $K_\beta$ peak is indicative of a 66 keV $\gamma$-ray transition in coincidence with the 747 keV transition.

statistics for the detection of a 34 keV transition [51]. Additionally, consultation of theoretical internal conversion coefficients [41] suggests that the intensity of such a transition in $^{158}$Ta would be reduced by a factor of 18 assuming an M1 transition. Although a 34 keV transition is neither observed, nor expected to be observed, it is expected to exist in order to complete the observed level scheme.

Ordering the transitions observed at the focal plane cannot be easily achieved using the focal plane data alone. Due to the constraint that all transitions are fed by decays from the high-spin isomer, unobserved side-feeding has little effect here and so the intensities of all transitions are consistent with each other. However, this nucleus affords the opportunity to study these transitions at both the focal plane and the target position.

If a decay path does not feed the high-spin isomeric state, the transitions at the base of the level scheme are observed at the target position rather than the focal plane. In this scenario, unobserved side feeding has the effect of increasing the intensities of transitions from states at lower excitation energies. This makes it possible to order transitions below the high-spin isomer based on their relative intensities at the target position. Intensities at the target position reveal that the

| $E_\gamma$ (keV) (Clover) | $I_\gamma$ (Clover) | Assigned multipolarity | $I_\gamma$ (Clover, Icc corrected) | $I_\gamma$ (JUROGAM) | Weisskopf $T_{1/2}$ (s) |
|---|---|---|---|---|---|
| 254.0(6) | 811(52) | (E2) | 922(59) | 630(14) | $1.04\times10^{-8}$ |
| 418.4(7) | 73(8) | (M2) | 94(10) | | $8.37\times10^{-8}$ |
| 583.4(8)* | 68(9) | (M1) | 71(9) | 228(7) | $1.12\times10^{-13}$ |
| 598.8(8) | ≡1000 | (E2) | 1013(75) | ≡1000 | $1.43\times10^{-10}$ |
| 707.6(9) | 114(10) | (E3) | 117(11) | | $8.89\times10^{-6}$ |
| 746.8(9) | 509(41) | (E2) | 513(42) | 584(15) | $4.75\times10^{-11}$ |
| 778.5(4) | 651(54) | (E2) | 656(54) | 818(22) | $3.82\times10^{-11}$ |
| 1001.6(11) | 1174(112) | (E3) | 1185(113) | | $7.82\times10^{-7}$ |

* Doublet

Table 5.3: Table of $\gamma$-ray transitions observed at the focal plane. Intensities have been relative efficiency corrected. Multipolarities are assigned based on the arguments presented in Section 5.1.5. The internal conversion corrected [41] intensities of delayed transitions, which are in coincidence, are consistent with each other. The variations in intensity of transitions detected at the target position is due to different side feeding contributions. Greater intensity at the target position places a transition further down the decay scheme. Intensities of parallel transitions must be combined to determine on their position.

parallel 747 and 779 keV transitions lie closer to the base of the level scheme, fed by the 599 keV transition which is in turn fed by the 254 keV transition. Although the parallel 747 and 779 keV transitions can be placed at lower excitation energies, the exact arrangement including the 66 keV and possible 34 keV transitions cannot be experimentally verified.

The possibility has been explored that discrepancies between the target position and focal plane ratio of intensities of the 747 and 779 keV transitions may yield evidence for their ordering, however, the ratio of target position and focal plane intensities for these transitions are consistent with each other, thus no evidence for their ordering has been obtained.

Based on their observation solely at the focal plane, the 418, 708 and 1002 keV transitions are all expected to decay directly from the high-spin isomeric state. Indeed, the absence of coincidences between any of these decays indicate that they reside in parallel decay paths. Note that while a transition of low intensity similar

in energy to the 1002 keV transition is observed at the target position, its intensity at the focal plane relative to other transitions present at both the target position and focal plane is disproportionate and so a transition of similar energy is expected to exist elsewhere in the level scheme, as discussed in Section 5.1.3.

While the 418 keV decay path is able to rejoin the level scheme via the 584 keV transition, no such transition is observed corresponding to the 708 keV decay path. This appears to leave the 708 keV transition disconnected, with no observable $\gamma$-ray transitions capable of linking it to the lower part of level scheme. That the 708 keV transition is observed indicates that it must feed the $^{158m1}\mathrm{Ta}_{(9^+)}$ $\alpha$-decaying state therefore it is considered that an E0 transition, which does not incur $\gamma$-ray emission, is present in order to link the 708 keV transition to the level scheme.

Although the GREAT spectrometer contains a silicon PIN diode array capable of detecting electrons such as those emitted during an E0 transition, at the time of the experiment the thresholds were optimised for the detection of higher energy particles, above the energy range of a 294 keV electron.

An alternative to detecting the E0 electron directly is the measurement of the X-rays emitted following the ejection of the electron. Experimental evidence for the existence of an E0 transition would consist of a significant number of additional X-rays in coincidence with the 708 keV transition in comparison to the number of X-rays in coincidence with a transition in a parallel decay path parallel to the E0 transition. In practice this can be done by gating on both the 708 and 1002 keV transitions in the focal plane clover detector and observing the number of X-rays observed in the focal plane planar detector.

Additional relative X-ray intensity observed in coincidence with the 708 keV transition is consistent with the presence of an E0 transition, as shown in Table 5.4. This provides a mechanism by which the 708 keV transition can depopulate the high-spin isomer while at the same time facilitate the population of the $(9^+)$ state.

| Gate energy (keV) | Normalised $I_{X-rays}$ |
|---|---|
| 707.6 | 76(11) |
| 1001.6 | 22(3) |

Table 5.4: $K_\alpha$ intensities from the x-strips, on the front face, of the focal plane planar detector, with the difference in the intensities of the gates accounted for. The X-ray intensities are inconsistent, with a greater quantity of X-rays coincident with the 708 gate.

The assignment of multipolarities to the observed $\gamma$-ray transitions by performing angular distribution measurements at the target position has not been possible due to the lack of distinction between dipole and quadrupole transitions. A possible explanation for this is that sub-nanosecond isomers exist at high-spin causing the nucleus to de-align while emitting $\gamma$ rays at the target position. Such isomers have been observed before in other nuclei in this region such as in $^{152}$Ho [52]. Alternative methods for determining multipolarities have been performed, however, direct measurements have not been possible for a number of transitions.

Initially, Weisskopf estimates make it possible to place limits on possible multipolarities assignments. During the sorting process $\gamma$ rays are required to pass a coincidence time of $\sim$50 ns to be considered coincident and so Weisskopf estimates of the half-life can be used to rule out multipolarities that are likely to exceed the coincidence time. These estimates can also be used to place suitable limits on the multipolarities of decays from the high-spin isomer. However, for lower order multipolarities, dipoles and quadrupoles, Weisskopf estimates can differ from the true half-life by factors of 100 and so more substantial evidence is desirable.

For low-energy transitions internal conversion can have a pronounced effect on the intensity of a $\gamma$-ray transition. The magnitude of this effect is strongly dependent on the multipolarity of the transition and so by comparing the observed intensity of the transition with those of the expected intensities for different multipolarities, the multipolarity can be ascertained.

| Gating transition | | |
|---|---|---|
| Energy (keV) | | Intensity |
| 746.8(4) | | 2118(50) |
| 66 keV transition | | |
| Multipolarity | Icc [41] | Intensity |
| E1 | 1.21 | 818(107) |
| M1 | 3.47 | 2347(306) |
| E2 | 20.97 | 14182(1850) |
| M2 | 70.72 | 47828(6238) |

Table 5.5: Internal conversion and efficiency corrected intensities of the 66 keV transition detected by the focal plane planar detector, within 50 ns of a 747 keV in the focal plane clover detector, for a variety of multipolarities. The efficiency correction is based on a simulated absolute efficiency [51]. Only an M1 is consistent with the intensity of the gating transition.

Only the 66 keV transition is a suitable candidate for this method as it is the only transition with measurable intensity that is low enough in energy to be particularly affected by internal conversion. A comparison between observed and expected gated intensities, shown in Table 5.5, reveals that consistency is only achieved through an M1 multipolarity assignment. This is consistent with the Weisskopf estimates which require that the 66 keV transition be dipole in nature.

The deduced level scheme of excited states below the new high-spin isomer is shown in Figure 5.6. Additional spin assignments are deduced in Section 5.1.5 upon introducing further constraints of the multipolarities.

### 5.1.3 Transitions feeding the high-spin isomer.

The $\gamma$ rays detected at the target position fit in to one of two categories: transitions that feed the high-spin isomer and transitions that by-pass the high-spin isomer. Transitions feeding the high-spin isomer can be obtained by modifying the RDT conditions to include delayed $^{158}$Ta $\gamma$ rays in addition to the $^{158m1}\mathrm{Ta}_{(9^+)}$ $\alpha$ decay. The requirement that delayed $\gamma$-ray transitions, identified in Figure 5.2(a), are observed

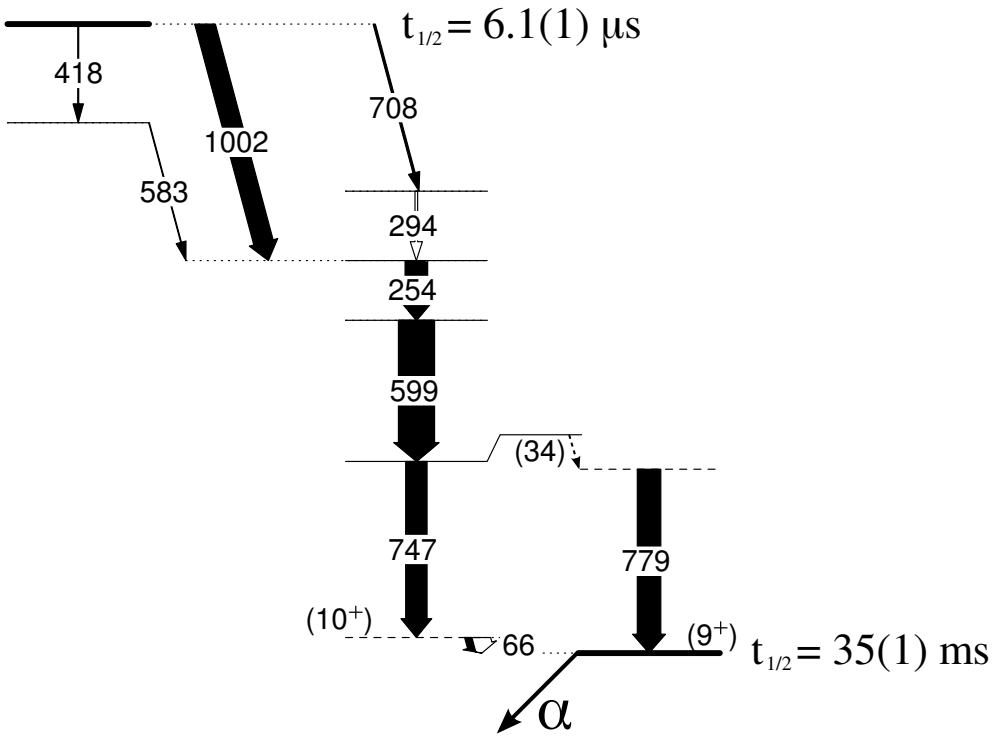


Figure 5.6: Level scheme for $^{158}$Ta below the high-spin isomer.

at the focal plane ensures that only transitions responsible for feeding the high-spin isomer will be observed at JUROGAM.

Correlating with these conditions reveals a clean $\gamma$-ray spectrum of transitions above the high-spin isomer, as shown in Figure 5.7, however, this cleanliness is achieved at the cost of statistics and so coincidence analysis cannot be performed, preventing further structural detail from being ascertained. Having identified a number of transitions feeding the isomer in the clean singles spectrum, a matrix of $\gamma$-ray transitions correlated with the $^{158m1}\mathrm{Ta}_{(9^+)}$ $\alpha$-decaying state can be used for coincidence analysis. Although such a matrix will contain all data at the target position feeding the $^{158m1}\mathrm{Ta}_{(9^+)}$ state, $\gamma$-$\gamma$ coincidences are sufficient to suppress transitions by-passing the isomer. This has the effect of increasing statistics by over a factor of 10 in comparison to correlations with the RDT condition including a focal plane $\gamma$ ray, enabling more detailed spectroscopy of the states above the high-spin

isomer to be performed.

The presence of a 1003 keV transition in these Figure 5.7 introduces the question of whether the 1002 keV transition does indeed depopulate the high-spin isomer as the half-life of the isomer is such that it would not be observed at JUROGAM, however, its presence at the focal plane is particularly distinct. As such, the 1003 keV transition is considered to be a separate transition which resides in the structures feeding the isomer. A level scheme based on this coincidence analysis is shown in Figure 5.8 and is accompanied by evidence in Figure 5.9, Figure 5.10 and Figure 5.11.

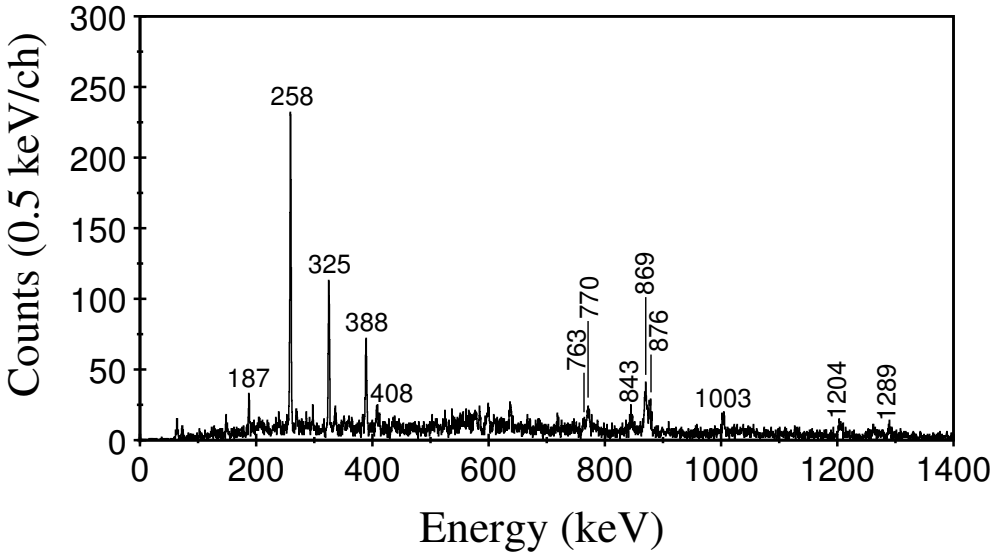


Figure 5.7: Energy spectrum of $\gamma$ rays tagged using the $\alpha$ decay from the $^{158m1}$Ta$_{(9^+)}$ state with a recoil-$\alpha$ correlation time of 175 ms, with the additional condition that a delayed $^{158}$Ta $\gamma$ ray is observed in the focal plane clover detector within 30 $\mu$s of the recoil implantation.

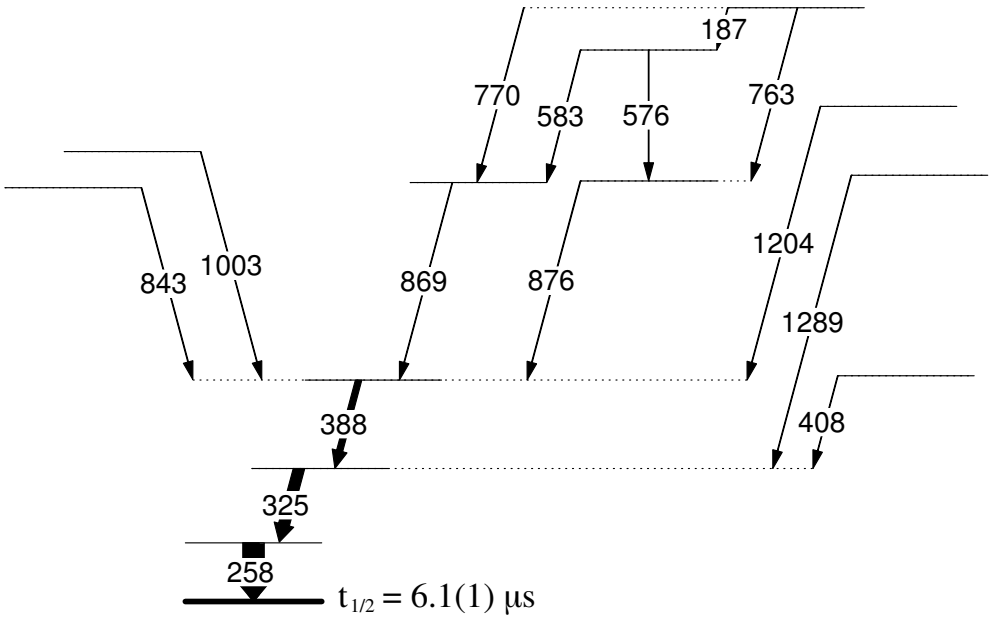


Figure 5.8: Levels above the high-spin isomer in $^{158}$Ta. The 258, 324 and 388 keV transitions have been identified by gating on both the $^{158m1}$Ta$_{(9^+)}$ $\alpha$ decay and a delayed $^{158}$Ta $\gamma$-ray transition. Coincidence analysis has been performed on a $^{158m1}$Ta$_{(9^+)}$ $\alpha$-tagged matrix using these identified transitions to determine the structure above the high-spin isomer.

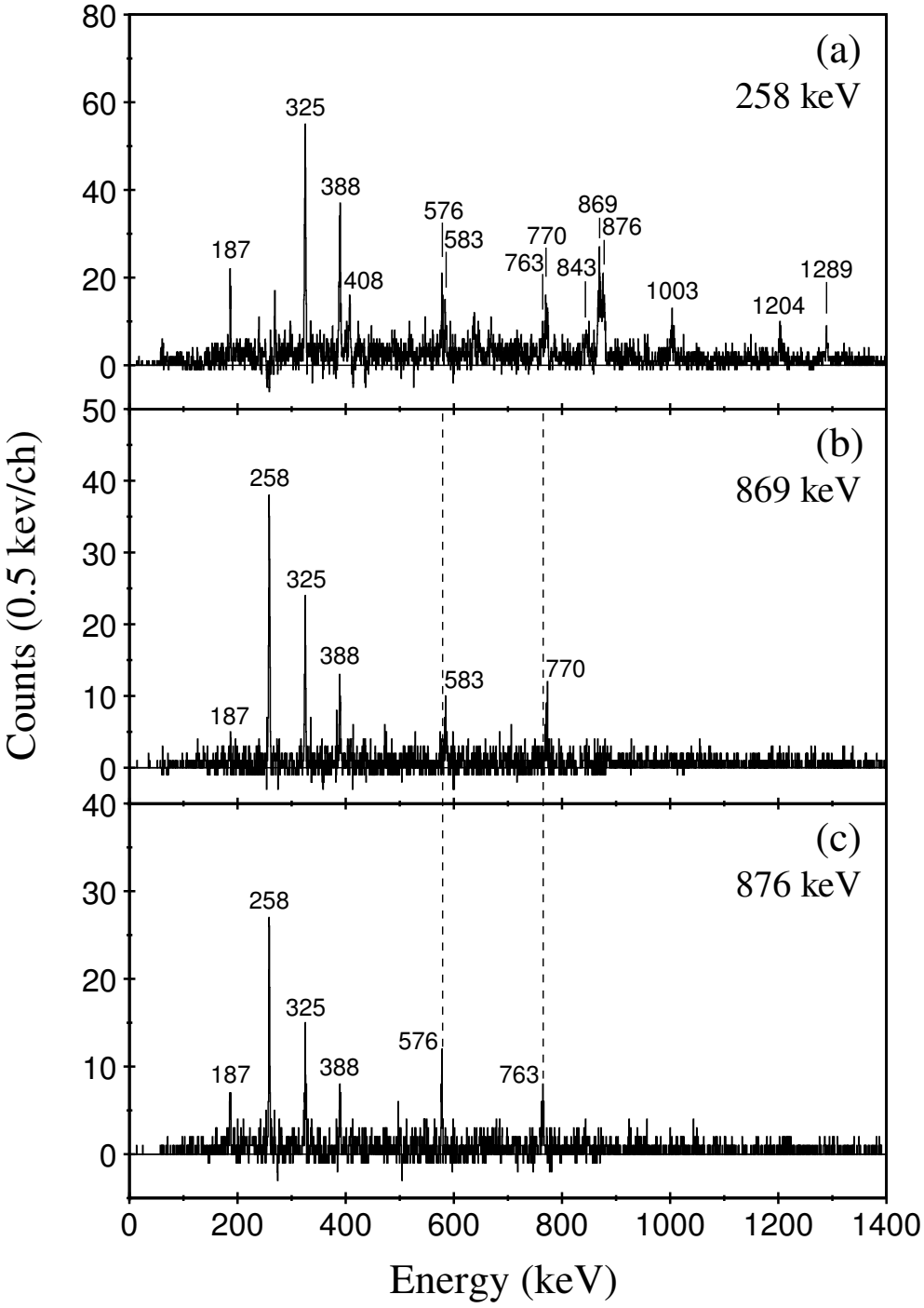


Figure 5.9: Gamma-ray coincidence spectra generated from a $^{158m1}$Ta$_{(9^+)}$ $\alpha$-decay correlated matrix with a recoil-$\alpha$ correlation time of 175 ms. Coincident transitions must occur within 50 ns of each other. A background subtraction accounts for random coincidences. **(a)** Spectrum in coincidence with the 258 keV transition. **(b)** Spectrum in coincidence with the 869 keV transition. **(c)** Spectrum in coincidence with the 876 keV transition.

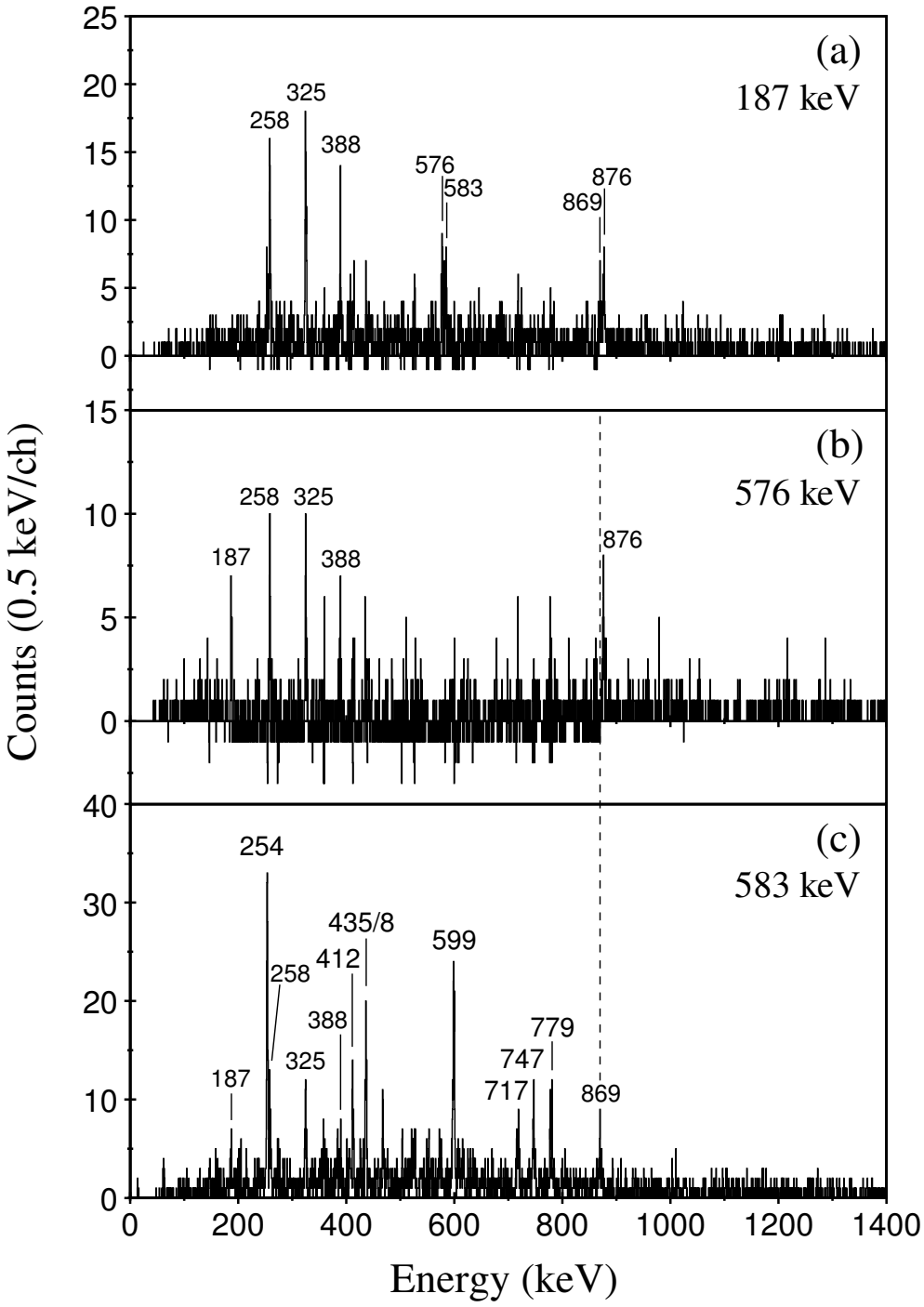


Figure 5.10: Gamma-ray coincidence spectra generated from a $^{158m1}$Ta$_{(9^+)}$ $\alpha$-decay correlated matrix with a recoil-$\alpha$ correlation time of 175 ms. Coincident transitions must occur within 50 ns of each other. A background subtraction accounts for random coincidences. **(a)** Spectrum in coincidence with the 187 keV transition. **(b)** Spectrum in coincidence with the 576 keV transition. **(c)** Spectrum in coincidence with the 583 keV transition without background subtraction. The 583 keV transition is a doublet and so a number of strong $^{158}$Ta transitions appear as false coincidences.

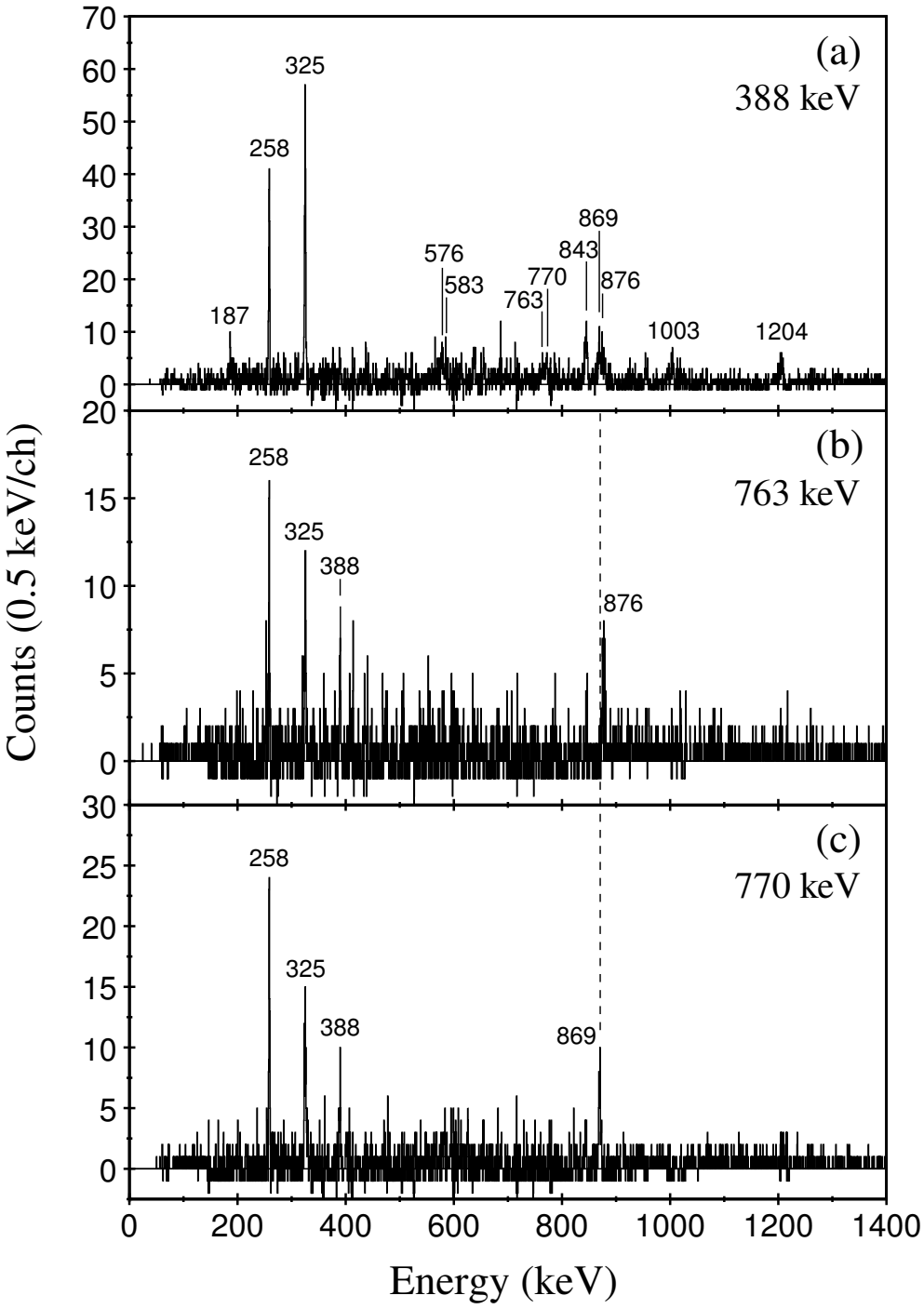


Figure 5.11: Gamma-ray coincidence spectra generated from a $^{158m1}$Ta$_{(9^+)}$ $\alpha$-decay correlated matrix with a recoil-$\alpha$ correlation time of 175 ms. Coincident transitions must occur within 50 ns of each other. A background subtraction accounts for random coincidences. **(a)** Spectrum in coincidence with the 388 keV transition. **(b)** Spectrum in coincidence with the 763 keV transition. **(c)** Spectrum in coincidence with the 770 keV transition.

### 5.1.4 Transitions bypassing the high-spin isomer

It has been possible to study transitions above and below the $^{158m2}$Ta isomer separately from the rest of the data due to the additional selectivity provided by correlating with its decays. Gamma-ray spectroscopy at the focal plane has made it possible to place transitions from states at lower excitation energies with confidence and transitions above the isomer have been established due to the additional selectivity provided by tagging on $\gamma$-ray transitions below the isomer. The remaining transitions observed at the target position are expected to feed the structure below the $^{158m2}$Ta isomer without populating the isomer or the structures above it. The $\alpha$-tagged spectrum shown in Figure 5.1(b) shows $\gamma$ rays observed at the target position feeding the $^{158m1}$Ta$_{(9^+)}$ state, which are collected in Table 5.6.

Coincidences shown in Figure 5.12, Figure 5.13 and Figure 5.14 indicate that the majority of transitions feed the level scheme above the 254 keV transition. An exception to this is the 438 keV transition, which feeds the structure below the $^{158m2}$Ta isomer such that the states depopulated by the 746 and 779 keV transitions are fed.

The strongest transitions by-passing the isomer are 412, 716, 358, 503 and 525 keV, all of which appear to be in coincidence with each other. Although the ordering of these transitions can be attempted using intensity arguments, the relative intensities of transitions in gated spectra suggest that such arguments may not be sufficient to place transitions correctly. In particular, the 503 and 525 keV gated spectra shown in Figure 5.14 show that the coincidences between the 358 and 503 keV transitions, and between the 383 and 525 keV transitions, are relatively strong in comparison to other transitions.

An explanation for this could be the presence of isomers with sub-nanosecond lifetimes in the decay path. Such delays in the decay of certain states may allow the nucleus move away from the focus of JUROGAM, thus transitions above this state

would be more efficiently detected and appear to be in stronger coincidence with each other than with those below. If short-lived isomers in the decay path are indeed responsible for the relative strength of coincidences between the 358 and 503 keV transitions and between the 383 and 525 keV transitions then the placement of the 412 keV transition is brought in to question.

Based on its intensity at the target position the 412 keV transition would be placed at lower excitation energies, however, its intensity in the 503 and 525 keV gated spectra would have to place it between the two pairs of relatively strongly coincident transitions, effectively placing it at higher excitation energies. This would not explain the relative strength of coincidences between the 412 keV transition and those at the base of the level scheme. As such, the probability of short-lived isomers and the placement of transitions detected at the target position have not been resolved in this work.

| $E_\gamma$ (keV) | $I_\gamma$ | Angular intensity ratio $\frac{I(157.6^o)}{I(94.16^o)}$ | $E_\gamma$ (keV) | $I_\gamma$ | Angular intensity ratio $\frac{I(157.6^o)}{I(94.16^o)}$ |
|---|---|---|---|---|---|
| 147.4(4) | 174(6) | 0.67(6) | 615.3(4) | 108(4) | |
| 187.0(4) | 64(3) | | 633.7(4) | 377(10) | 1.12(7) |
| 237.6(4) | 86(3) | | 685.6(4) | 93(4) | |
| 253.6(4) | 630(14) | 0.83(3) | 716.4(4) | 599(15) | 1.04(5) |
| 258.3(4) | 530(12) | 0.67(2) | 727.4(4) | 81(4) | |
| 273.5(4)* | 351(8) | 0.79(4) | 737.6(4) | 121(5) | |
| 324.5(4) | 337(8) | 0.80(4) | 746.8(4) | 584(15) | 0.94(4) |
| 336.7(4) | 204(6) | 0.90(8) | 762.9(5) | 64(7) | |
| 358.3(4) | 490(11) | 0.78(4) | 770.2(5) | 116(7) | |
| 382.8(4) | 290(7) | 0.70(5) | 778.5(4) | 818(22) | 1.03(4) |
| 388.4(4) | 173(5) | 0.97(9) | 797.7(4) | 119(5) | |
| 406.6(4) | 187(5) | 0.67(6) | 804.2(5) | 61(4) | |
| 412.0(4) | 721(16) | 1.11(4) | 825.3(4) | 131(5) | |
| 435.1(4) | 473(12) | | 842.8(5) | 227(8) | |
| 438.4(4) | 173(6) | | 860.2(5) | 364(12) | |
| 466.5(4) | 58(3) | | 869.0(5) | 196(7) | |
| 473.8(4) | 137(4) | 0.91(11) | 876.5(5) | 144(5) | |
| 503.1(4) | 483(11) | 0.82(4) | 1003.3(5) | 107(5) | |
| 524.9(4) | 383(11) | 1.15(7) | 1204.4(5) | 116(5) | |
| 536.2(4) | 73(4) | | 1218.0(5) | 108(5) | |
| 583.2(4)* | 228(7) | 1.09(12) | 1260.3(6) | 69(4) | |
| 598.8(4) | $\equiv$ 1000 | 0.88(3) | 1274.8(7) | 32(3) | |
| 606.1(4) | 253(7) | | 1289.1(6) | 46(4) | |

* Doublet

Table 5.6: Energies and efficiency corrected relative intensities of $\gamma$-ray transitions feeding the $^{158m1}$Ta$_{(9^+)}$ $\alpha$-decaying state. Measured angular intensity ratios are also shown. Angular intensity ratios of transitions in $^{157}$Hf are 0.81(1) for a dipole ($9/2^- \rightarrow 7/2^-$) and 0.93(4) for a quadrupole ($13/2^- \rightarrow 9/2^-$, $17/2^- \rightarrow 13/2^-$ and $21/2^- \rightarrow 17/2^-$). Poor separation between dipole and quadrupole transitions prevents conclusive multipolarity assignments.

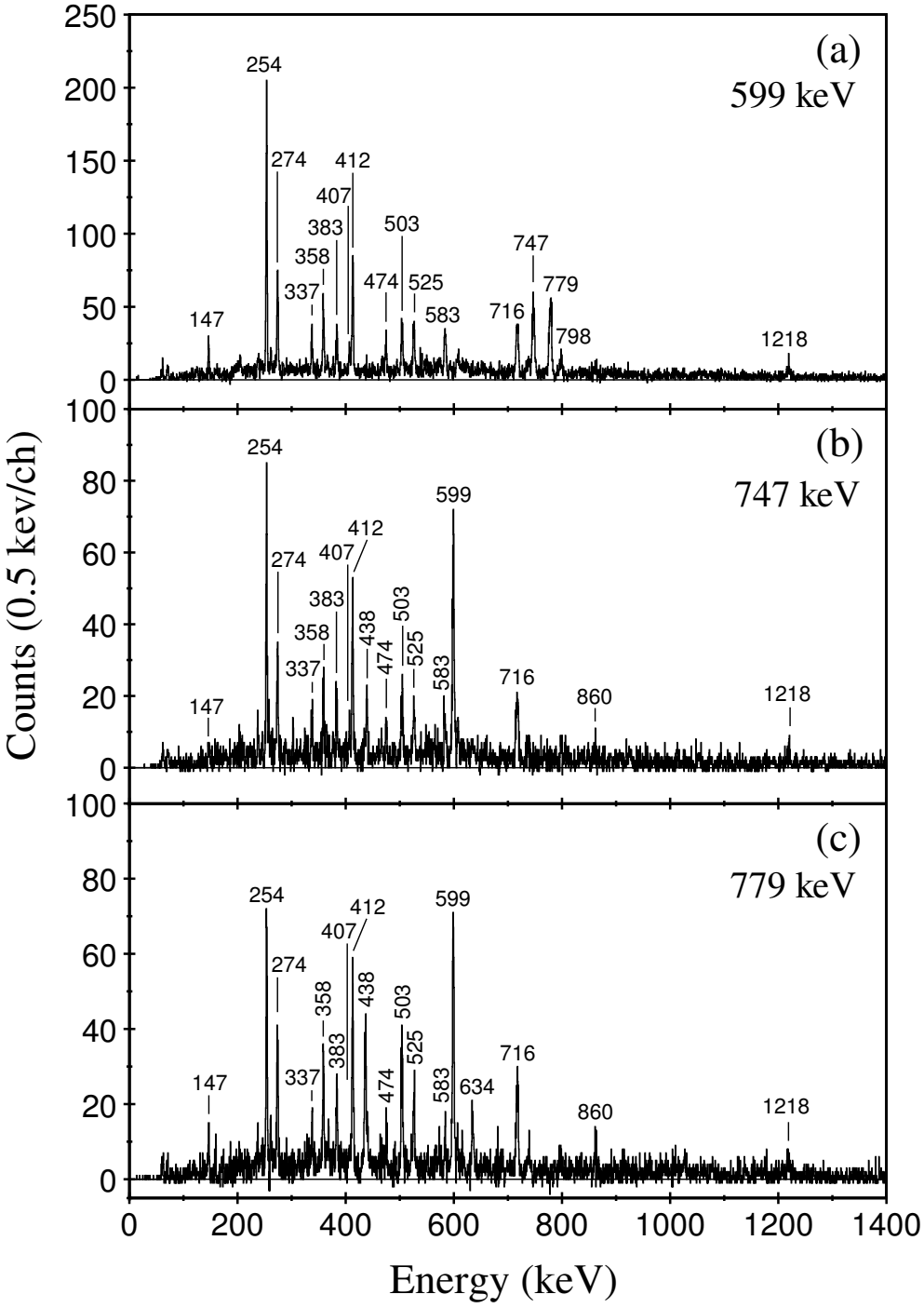


Figure 5.12: Gamma-ray coincidence spectra generated from a $^{158m1}$Ta$_{(9^+)}$ $\alpha$-decay correlated matrix with a recoil-$\alpha$ correlation time of 175 ms. Coincident transitions must occur within 50 ns of each other. A background subtraction accounts for random coincidences. **(a)** Spectrum in coincidence with the 599 keV transition. **(b)** Spectrum in coincidence with the 747 keV transition. **(c)** Spectrum in coincidence with the 779 keV transition.

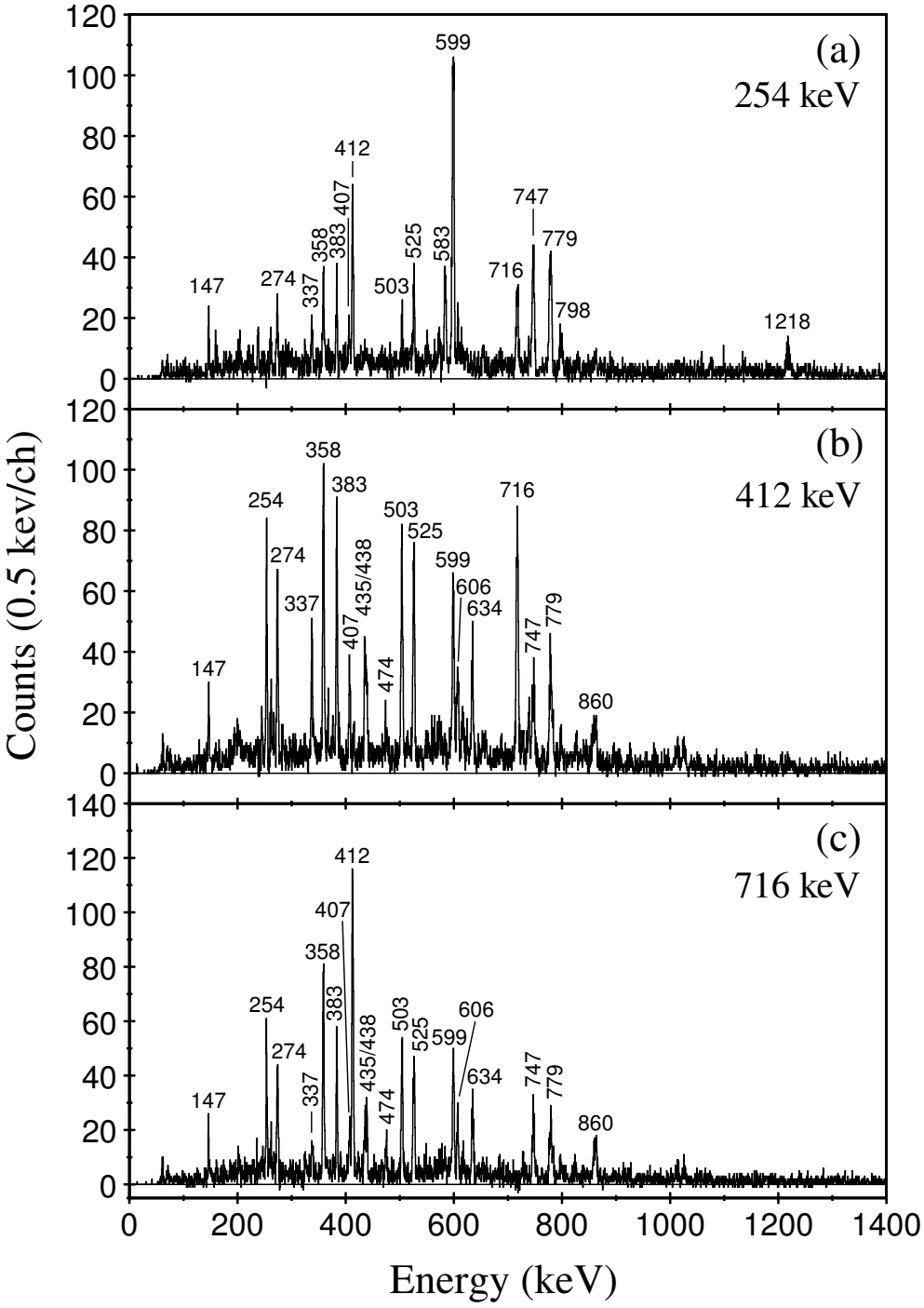


Figure 5.13: Gamma-ray coincidence spectra generated from a $^{158m1}$Ta$_{(9^+)}$ $\alpha$-decay correlated matrix with a recoil-$\alpha$ correlation time of 175 ms. Coincident transitions must occur within 50 ns of each other. A background subtraction accounts for random coincidences. **(a)** Spectrum in coincidence with the 254 keV transition. **(b)** Spectrum in coincidence with the 412 keV transition. **(c)** Spectrum in coincidence with the 716 keV transition.

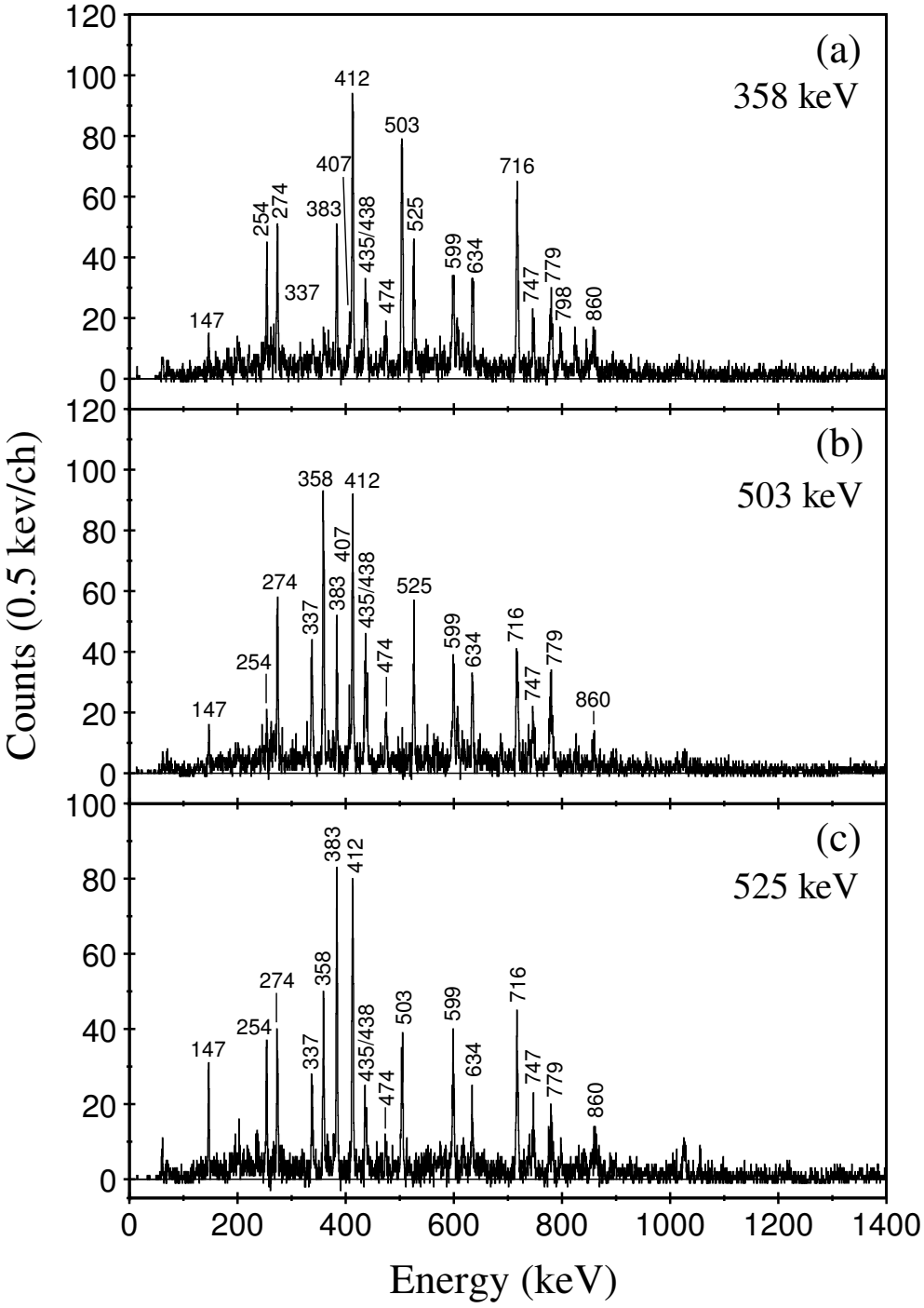


Figure 5.14: Gamma-ray coincidence spectra generated from a $^{158m1}$Ta$_{(9^+)}$ $\alpha$-decay correlated matrix with a recoil-$\alpha$ correlation time of 175 ms. Coincident transitions must occur within 50 ns of each other. A background subtraction accounts for random coincidences. **(a)** Spectrum in coincidence with the 358 keV transition. **(b)** Spectrum in coincidence with the 503 keV transition. **(c)** Spectrum in coincidence with the 525 keV transition.

### 5.1.5 Decays from the high-spin isomer

A new $\alpha$ decay of energy 8644(11) keV and half-life 6.4(4) $\mu$s has been detected in the DSSDs, as shown in Figure 5.15, and has been confirmed to originate from $^{158}$Ta using recoil-$\gamma$ correlations. Gamma-ray transitions correlated with this previously unknown $\alpha$ decay are those of $^{158}$Ta identified in Section 5.1. In particular, similarities between spectra in Figure 5.2(b) and Figure 5.15(c) suggest that this $\alpha$ decay originates from the same high-spin isomer as the delayed $\gamma$-ray transitions observed at the focal plane, the $^{158m2}$Ta state.

A further indication that both the high-spin isomer and this new $\alpha$ decaying state are the same is the consistency between measurements of the half-life. The fitted decay curve shown in Figure 5.15(b) provides a half-life of 6.4(4) $\mu$s, which is consistent with 6.1(1) $\mu$s measured using the $\gamma$ rays. The measured half-life is such that these decays are often lost in the dead time of the DSSDs. Furthermore, the signal in the pulse shaping electronics has often not had time to return to the baseline when these $\alpha$ particles are detected. As such, a baseline correction is required to obtain the true energy and full peak area.

No $\gamma$-ray transitions are observed at the focal plane in coincidence with this $\alpha$ decay which indicates that an isomeric state in $^{154}$Lu is populated directly. Observations of decays following the both the $^{158m1}$Ta$_{(9^+)}$ and $^{158m2}$Ta state $\alpha$ decays show the 5331 keV $\alpha$ decay from $^{154}$Yb, presumably following an unobserved $\beta$ decay from $^{154}$Lu. The associated decay curves are consistent with the half-lives of both the $^{154}$Lu$_{(9^+)}$ $\beta$ decay and $^{154}$Yb $\alpha$ decay, shown in Figure 5.16. While this evidence does not eliminate the possibility of the $^{154}$Lu$_{(2^-)}$ state being populated during this process, the result is consistent with the $\alpha$ decay of the $^{158m2}$Ta state populating the $^{154}$Lu$_{(9^+)}$ state directly. This consistency, combined with the absence of existing decay information for the $^{154}$Lu$_{(2^-)}$ state, leads to the assumption that it is the $^{154}$Lu$_{(9^+)}$ which is populated by the $^{158m2}$Ta $\alpha$ decay.

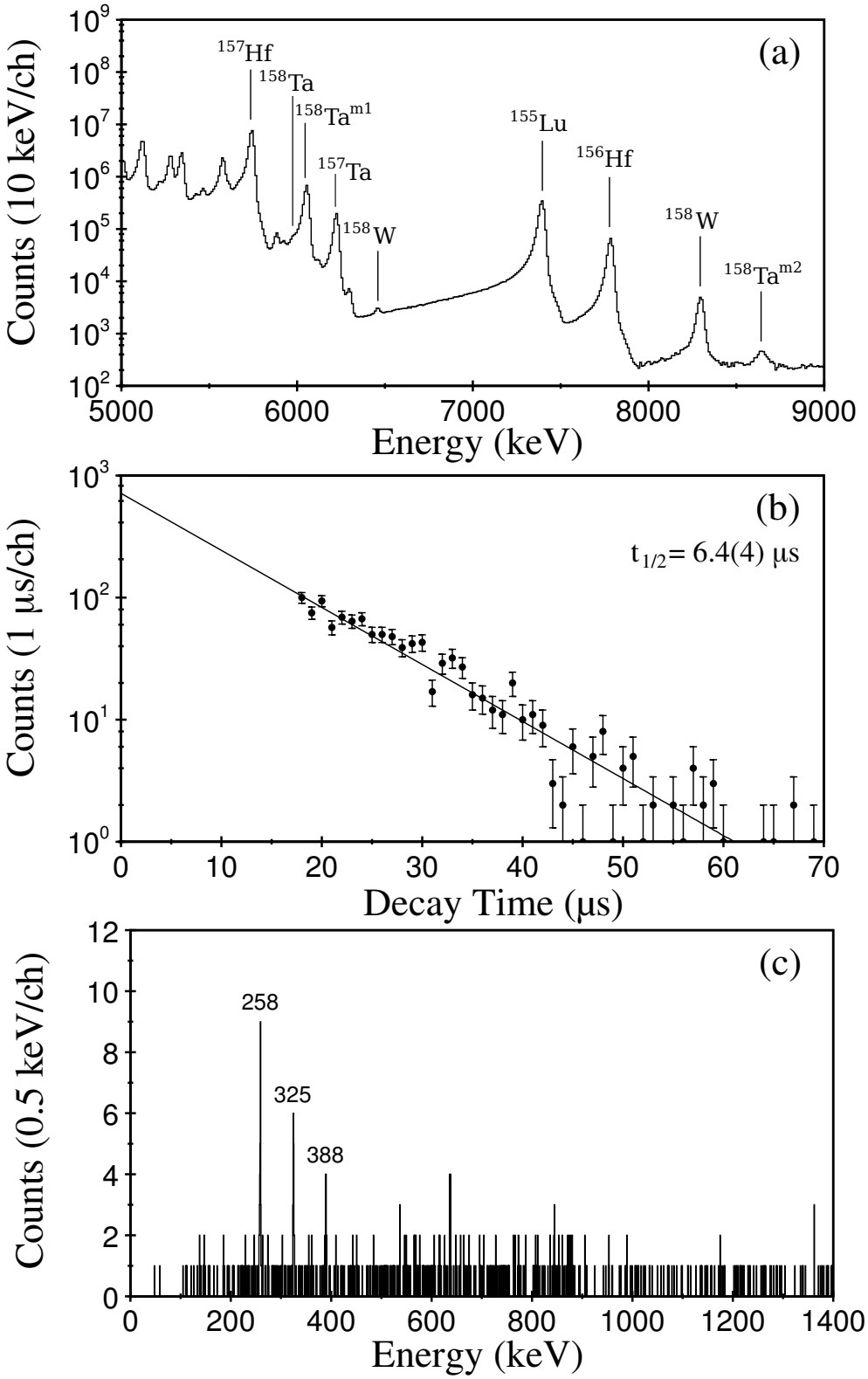


Figure 5.15: **(a)** DSSD energy spectrum of decays preceded by a recoil within a 5 s correlation time. A previously unobserved $\alpha$ decay appears at 8644(11) keV. **(b)** Decay curve of the 8644 keV $\alpha$ decay with a fitted half-life of 6.4(4) $\mu$s. **(c)** JUROGAM energy spectrum of $\gamma$ rays tagged on the 8644 keV $\alpha$ decay with a recoil-$\alpha$ correlation time of 32 $\mu$s.

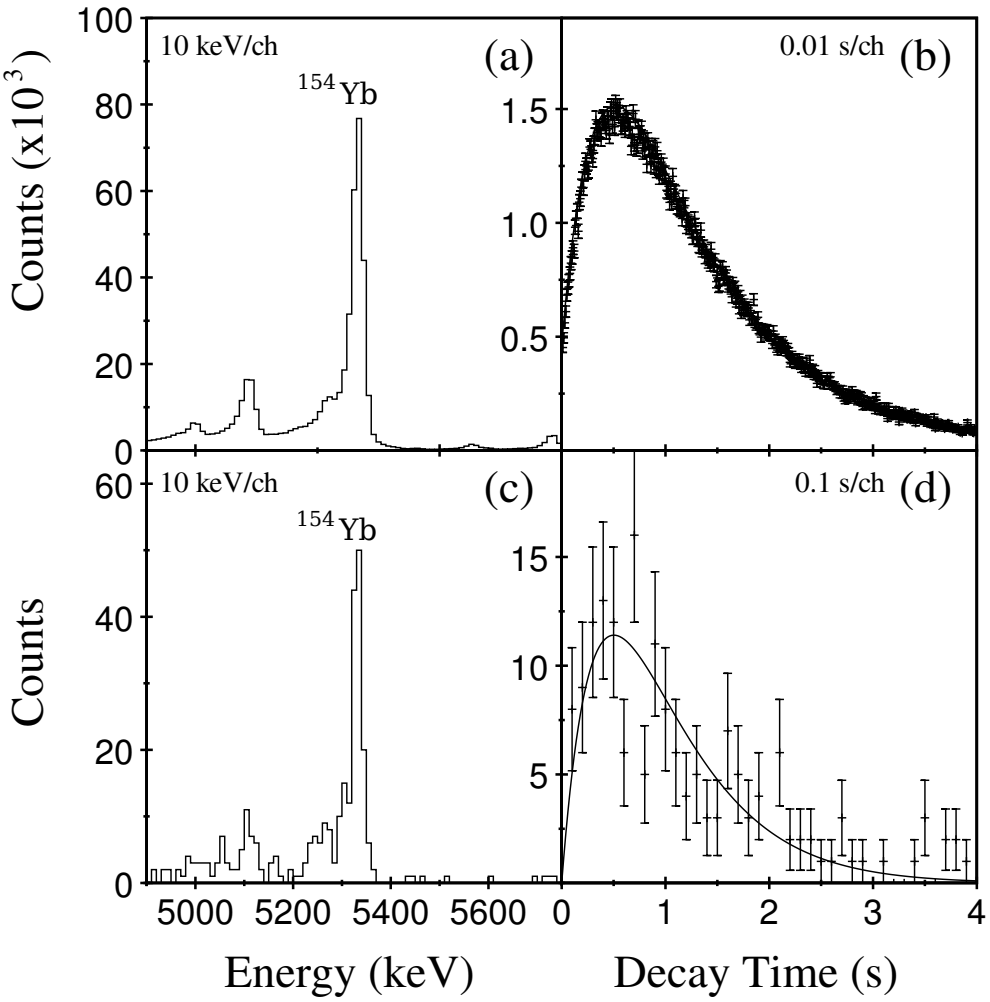


Figure 5.16: **(a)** The energy and **(b)** decay time of decays following the $^{158m1}$Ta$_{(9^+)}$ $\alpha$ decay. **(c)** The energy and **(d)** decay time of decays following the $^{158m2}$Ta $\alpha$ decay. (a) and (c) are obtained from the DSSDs. The 5331 keV $\alpha$ decay from $^{154}$Yb following the $\beta$ decay from $^{154}$Lu is clearly visible in both spectra. (b) and (d) show decay curves tagged on the $^{154}$Yb $\alpha$ decay and are both consistent with the half-lives of the $^{154}$Lu$_{(9^+)}$ $\beta$ decay and $^{154}$Yb $\alpha$ decay.

If the $\alpha$ decays from the $^{158m1}$Ta$_{(9^+)}$ state and the $^{158m2}$Ta state both decay to the $^{154}$Lu$_{(9^+)}$ state, the separate $\alpha$ and $\gamma$ decay branches from the $^{158m2}$Ta state will form a closed Q-value loop in which the energies of both paths are equal. This serves as evidence against the possibility of unobserved $\gamma$-ray transitions in the structure below the $^{158m2}$Ta state and also constrains the spin assignments of states in this section of the decay scheme. Further constraints can be placed on the decay

scheme with knowledge of the reduced decay width $\delta^2$ of the $^{158m2}$Ta $\alpha$ decay. Such calculations require the branching ratio of the $\alpha$ decay to be measured.

Obtaining a branching ratio between the $\alpha$ and $\gamma$ branches directly is difficult as the differences in the geometry, efficiency and dead-time constraints between the DSSDs and the clover detector mean the intensities of transitions depopulating the $^{158m2}$Ta state are not comparable.

An alternative and more effective method of determining the branching ratio is to compare the intensities of the $\alpha$ decays from the $^{158m1}$Ta$_{(9^+)}$ state and the $^{158m2}$Ta state, gating on $\gamma$-ray transitions known to feed the $^{158m2}$Ta state. As the $\gamma$ decays from the $^{158m2}$Ta state populate the $^{158m1}$Ta$_{(9^+)}$ state, the $\alpha$ decay from this state represents the fraction of the $^{158m2}$Ta state that has been depopulated by $\gamma$ rays, as shown in Figure 5.17. This method assumes that all $\gamma$-ray branches depopulating the $^{158m2}$Ta state feed the $^{158m1}$Ta$_{(9^+)}$ state. This simplifies the comparison as now the decay mode and the detector are the same for both the $\alpha$ and $\gamma$ branches, however, a direct comparison between the intensities of the $\alpha$ decays still requires a number of considerations. The half-life of the 8644 keV decay from the high-spin isomer is short enough that the majority of the intensity is lost in the dead time of the detector. While this has a negligible effect on the decay of the 6046 keV decay, its longer half-life increases its vulnerability to miscorrelations with other implantations in the same DSSD pixel. Such miscorrelations will prevent the association with the gating transition, reducing the measured intensity and altering the deduced branching ratio.

The issue of losses in the dead time region can be addressed by extrapolating an exponential decay curve in order to obtain the total intensity, as illustrated in Figure 5.18. Although more than two half-lives of the $^{158m2}$Ta $\alpha$ decay are lost in the dead time, sufficient statistics exist to fit a decay curve making this method of obtaining the total intensity viable.

The possibility of miscorrelations with the decay of the longer lived $^{158m1}$Ta$_{(9^+)}$

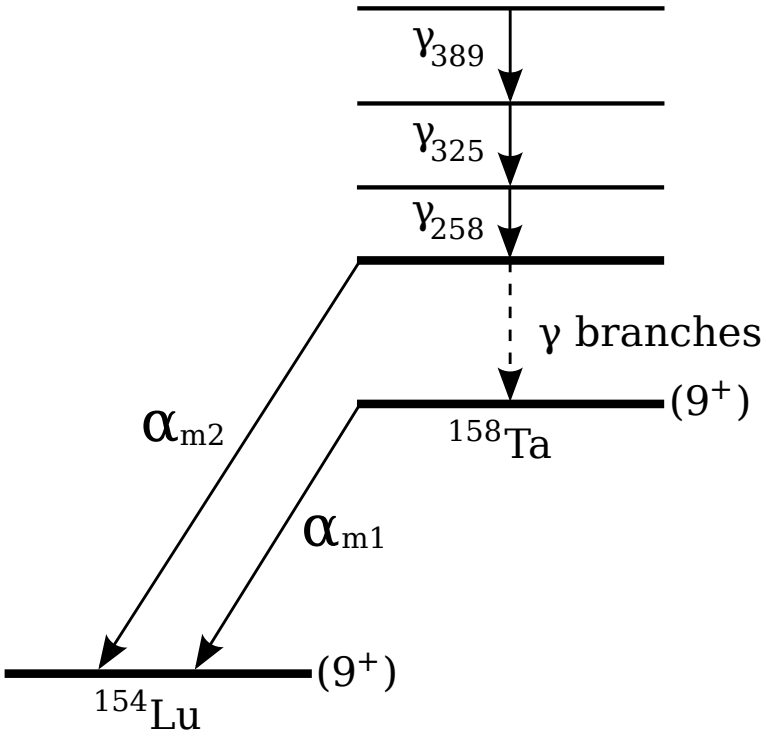


Figure 5.17: A branching ratio for decays from the high spin isomer can be obtained by gating on $\gamma$-ray transitions feeding the $^{158m2}$Ta state and comparing the intensities of the $\alpha$ decays. The fraction depopulating the $^{158m2}$Ta via $\gamma$ rays is represented by the intensity of the $^{158m1}\text{Ta}_{(9^+)}$ $\alpha$ decay.

state is greater than that of the shorter lived $^{158m2}$Ta state, however, the event rate is not sufficient to have a significantly damaging effect with an average event rate of 0.37 Hz for the highest counting pixel in the DSSDs. The deduced branching ratio for the $\alpha$ and $\gamma$ branches of the $^{158m2}$Ta state are shown in Table 5.7.

| | $\alpha_{m1}$ | $\alpha_{m2}$ |
|---|---|---|
| $I_{measured}$ | 58270 ± 250 | 93 ± 12 |
| $I_{corrected}$ | - | 1000 ± 120 |
| $\%_{100}$ | 98.3 ± 0.6 | 1.7 ± 0.2 |

Table 5.7: branching ratios of decays from the high-spin isomer. The $\gamma$-ray branches are represented by $\alpha_{m1}$.

The formation of an $\alpha$ particle to decay from $^{158m2}$Ta state to the $^{154}\text{Lu}_{(9^+)}$ state would be expected to incur large structural changes in the $^{158}$Ta nucleus, hindering

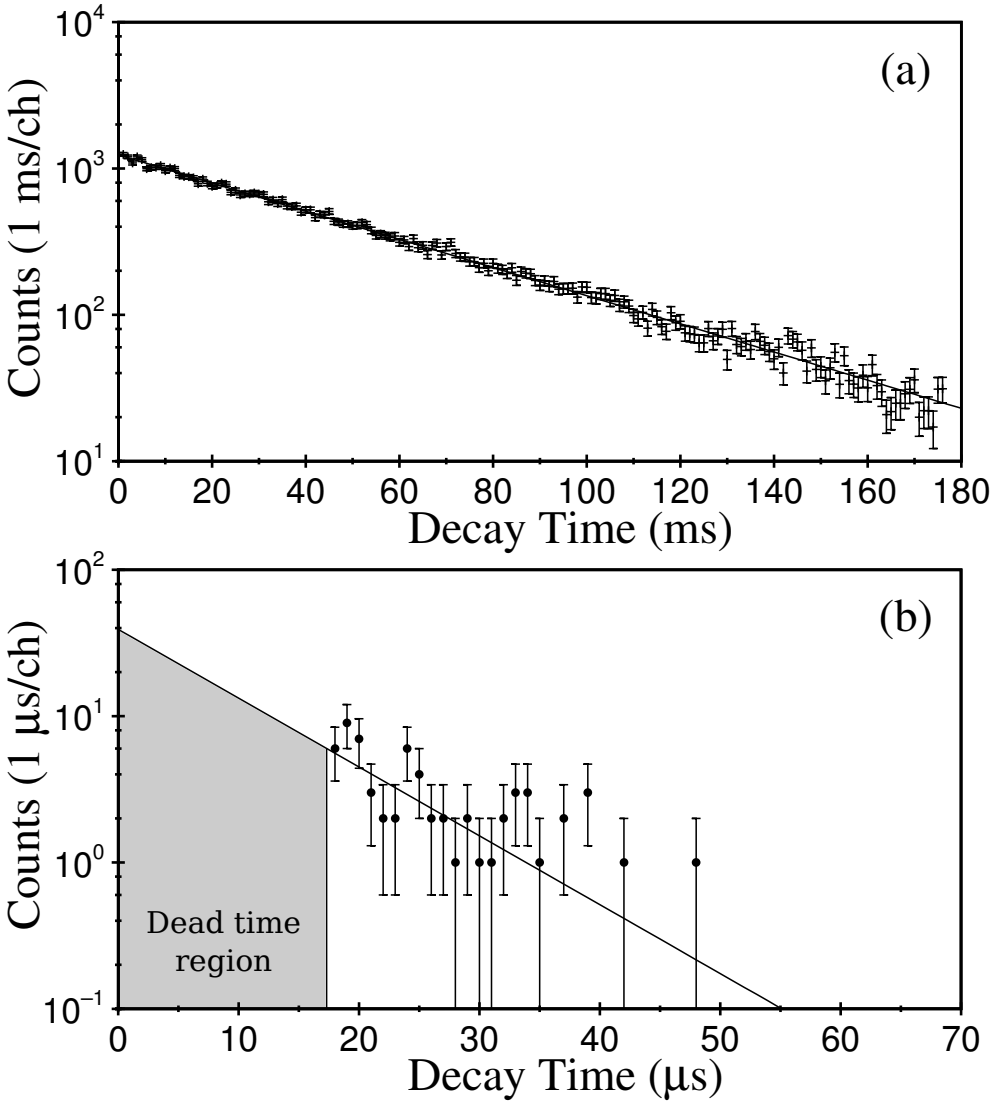


Figure 5.18: Demanding that at least one of the transitions feeding the high-spin isomer is observed results in the following decay curves of **(a)** the 6046 keV $\alpha$ decay, effectively unaffected by dead time, **(b)** the 8644 keV $\alpha$ decay. The half-life is so short that more than two half-lives are lost in the dead time of the DSSDs. Extrapolating the decay curve makes it possible to reconstruct the original intensity.

the decay. A comparison of the decay width $\delta^2$, as described in Section 2.4, with other hindered and unhindered decays in this region of the nuclear landscape makes it possible to deduce the angular momentum carried away from the nucleus by during this process.

The decay width $\delta^2$ for hindered and unhindered decays in $^{155-157}$Lu, $^{156-158}$Hf,

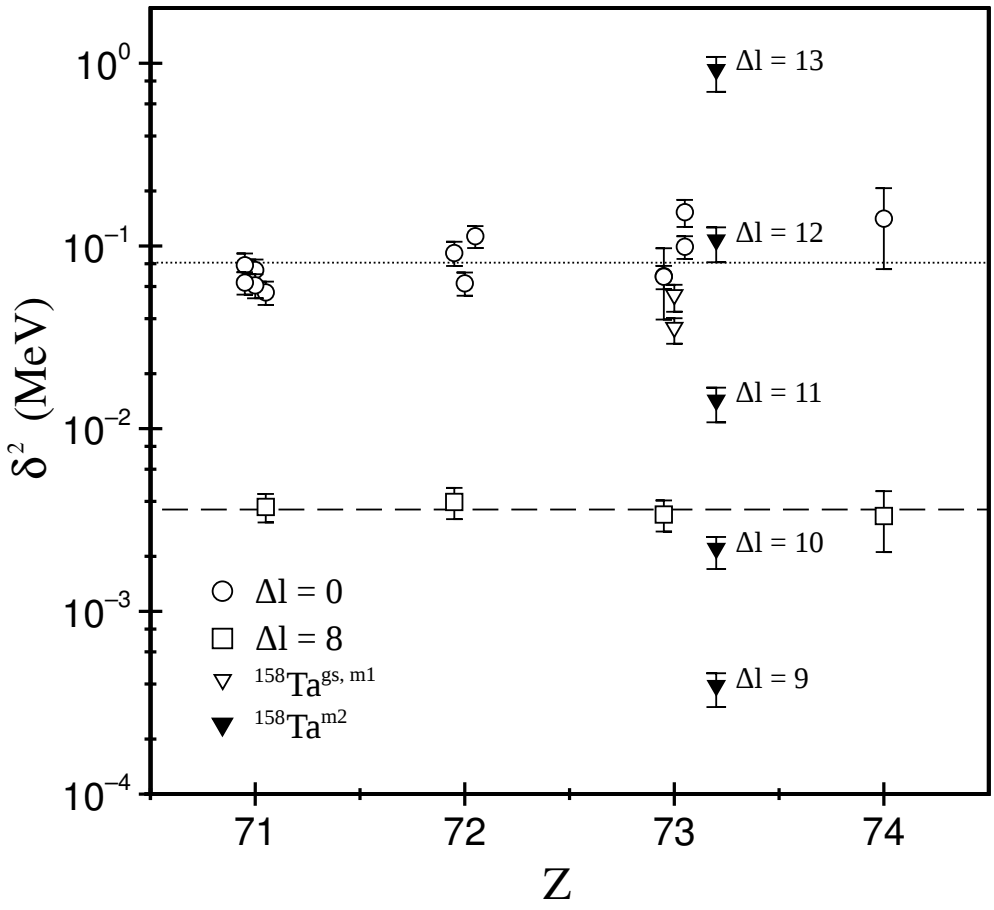


Figure 5.19: Reduced decay width $\delta^2$ as a function of proton number. Values of $\delta^2$ for the new $\alpha$ decay, carrying different angular momenta, have been calculated using the theory described in Section 2.4. An average value for $0^+ \rightarrow 0^+$ $\alpha$-decays in this region of the nuclear chart has been used to obtain a reference for favoured decays. Similarly, an average value for the decay widths of other high-spin *alpha*-decaying states in this region identifies expected values for hindered decays.

$^{157-159}$Ta and $^{158}$W are shown in Figure 5.19. A clear distinction can be seen between those decays that are unhindered, carrying no angular momentum from the nucleus, and those that are hindered. Calculations for the $\delta^2$ of the 8644 keV decay in $^{158}$Ta have been performed for a range of changes in angular momentum and give an indication of the spin change expected for a hindered decay.

Based on these calculations of the decay width, the spin change between the $^{158m2}$Ta high-spin isomer and the $^{154}$Lu$_{(9^+)}$ state is between 10 and 11 units of angular

momentum. This makes it possible to constrain the spin assignment of the $^{158m2}$Ta high-spin isomer to between 19 and 20.

This information has consequences for the multipolarities of the $\gamma$ rays that occupy the decay scheme below the high-spin isomer. The $\gamma$-ray spectroscopy was capable of assigning a multipolarity only to the 66 keV M1 transition, and from Weisskopf estimates an E3 multipolarity has been assigned to the 1002 keV transition. Multipolarities have not been determined for the other transitions, however, the constraints put on the high-spin isomer by the $\alpha$ decay require that the 253, 598 and 746 keV transitions are quadrupole transitions in order to reach the isomer spin of 19. No additional angular momentum can be generated without assigning E3 or M3 multipolarities to some of these transitions, incurring further, experimentally unobserved, isomerism.

The deduced level scheme, including sections above, below and bypassing the new high-spin isomer, with spin and parity assignments is shown in Figure 5.20.

## 5.2 Discussion

A level scheme for $^{158}$Ta has been constructed based on transitions that have been observed for the first time in this work. Nucleon configurations are deduced and will be compared with those of neighbouring isotones in order to observe the evolution of nuclear structure approaching, and crossing, the proton drip line.

### 5.2.1 Nucleon configurations of low lying states

Low-lying states in $^{158}$Ta are based on single-particle configurations of valence nucleons of which there are nine protons ($Z = 73$) and three neutrons ($N = 85$) above a semi-magic $^{146}$Gd core. As such, the orbitals available for proton occupation are the $1h_{11/2}$, $2d_{3/2}$ and $3s_{1/2}$ and for neutrons are the $2f_{7/2}$, $1h_{9/2}$ and $1i_{13/2}$

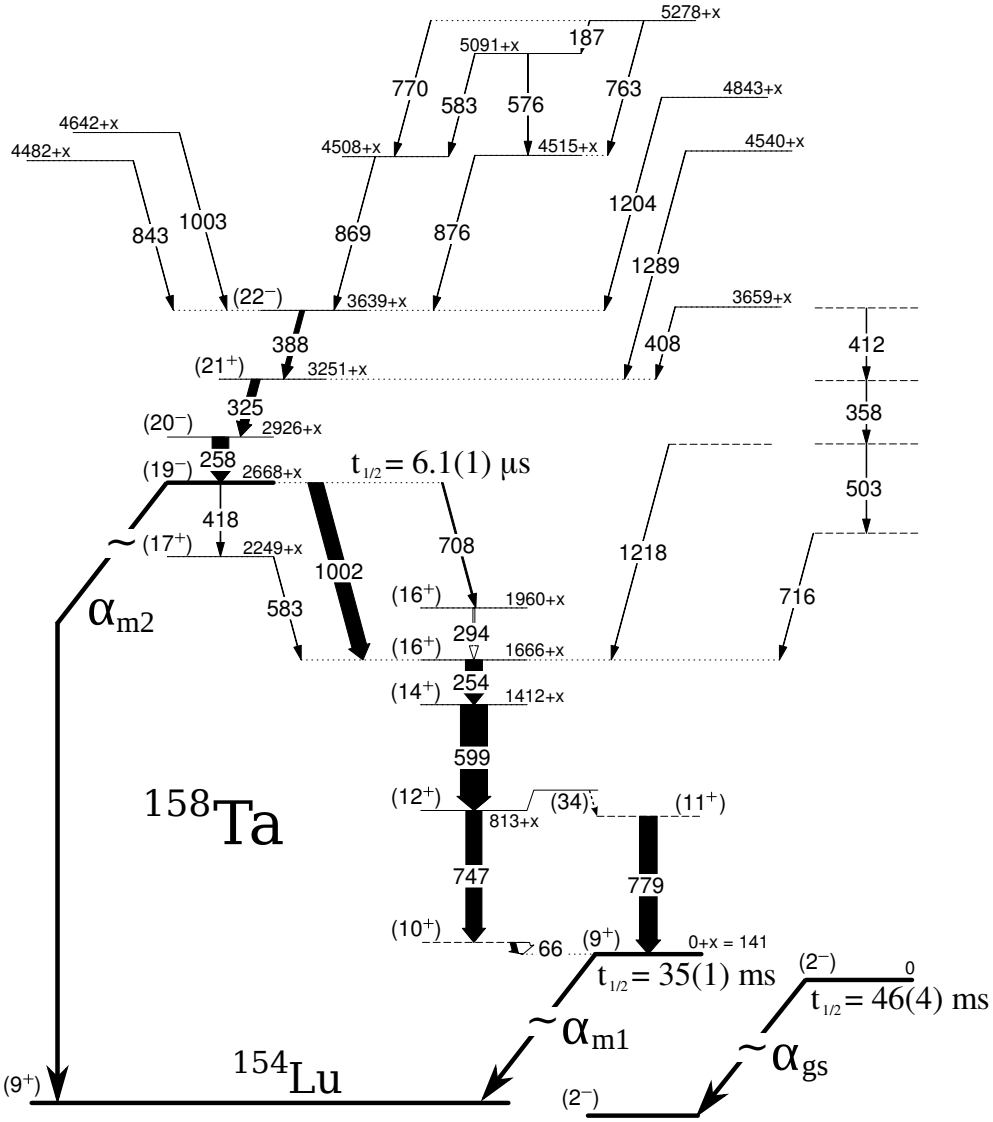


Figure 5.20: Decay scheme of $^{158}$Ta with deduced spin and parities based on analysis of the new $\alpha$ decay from the $^{158m2}$Ta state.

Based on previous observations of its $\alpha$ decay, the $^{158m1}$Ta state has been tentatively assigned a $(9^+)$ spin-parity [50] built on a $\pi h_{11/2} \otimes \nu f_{7/2}$ configuration. This structure assumes that the angular momenta of the odd proton and neutron couple parallel to each other, according to the "weak" coupling rule [53].

As will be discussed in Section 5.2.4, the deduced level scheme reveals a number of similarities with other $N = 85$ isotones, particularly in the low-lying states. Although the exact ordering of transitions below the $(12^+)$ state has not been confirmed in this work, systematics make it possible to assign the 34 and 66 keV transitions as either the $(10^+) \rightarrow (9^+)$ or $(12^+) \rightarrow (11^+)$ transitions, and the 747 and 778 keV transitions as the $(11^+) \rightarrow (9^+)$ or $(12^+) \rightarrow (10^+)$ transitions. To arrange these transitions differently would diverge considerably from systematic trends in the isotones, which is considered to be unlikely. The energies of the 747 and 778 keV transitions are similar to those corresponding to neutron pair breaking in this region of the nuclear chart [45, 47, 48].

Two separate structures dominate the low lying states, the $\pi h_{11/2} \otimes \nu(f_{7/2})^3$ configuration, which is maximally aligned at $13^+$ and the $\pi h_{11/2} \otimes \nu(f_{7/2})^2 h_{9/2}$ configuration, which is maximally aligned at $16^+$. The $f_{7/2}$ and $h_{9/2}$ orbitals are very close in excitation energy in this region of the nuclear landscape. This is consistent with the low energies assigned to the $(10^+) \rightarrow (9^+)$ and $(12^+) \rightarrow (11^+)$ transitions, which correspond to the de-excitation of a neutron from the $h_{9/2}$ orbital to the $f_{7/2}$ orbital.

While these configurations provide a mechanism for two structures, $(14^+) \rightarrow (13^+)$ and $(13^+) \rightarrow (11^+)$ transitions to populate and depopulate the $(13^+)$ state are not observed. The rather small differences in excitation energies between levels in these two bands suggest that it is possible that the $(13^+)$ state is higher in excitation energy than the $(14^+)$ state and, as a result of decreasing proximity to the yrast line, is not populated strongly in fusion evaporation reactions.

### 5.2.2 The $(19^-)$ isomer configuration

The 6.1(1) $\mu$s isomer with a spin and parity of $(19^-)$ has been observed for the first time in this work. Due to its proximity to the $N = 82$ neutron shell closure, $^{158}$Ta is considered to be near spherical hence the most likely cause of isomerism at such high spin is a large change in angular momentum. The decay time is sufficiently long to allow $\alpha$ decay to compete with the $\gamma$ decay.

A spin and parity of $(19^-)$ has been assigned to the isomer based on the arguments presented in Section 5.1.5. This spin assignment presents a problem in that no obvious configuration of nucleons give 19 units of angular momentum. If we assume that the $(16^+)$ state is correctly assigned, and that the 1002 keV transition is indeed of E3 character, then the number of possibilities available diminishes somewhat as a parity change is required. Measurements of the B(E3) are revealed to be rather low for the 1002 keV transition at 0.1 W.u. This is indicative of single-particle behaviour rather than collective behaviour.

There are only two available mechanisms to achieve the parity change, which are neutron excitation into the $1i_{13/2}$ orbital and proton excitation in either the $2d_{3/2}$ or $3s_{1/2}$ orbitals. The case of the later mechanism would require a protons pair to break before a proton can be excited into an even-parity orbital to ensure that the isomer configuration has a greater angular momentum than the maximally aligned $\pi h_{11/2} \otimes \nu(f_{7/2})^2 h_{9/2}$ configuration.

In the $\pi h_{11/2} \otimes \nu f_{7/2} h_{9/2} i_{13/2}$ configuration the maximally aligned configuration is $20^-$ and for the $\pi(h_{11/2})^2 d_{3/2} \otimes \nu(f_{7/2})^2 h_{9/2}$ and $\pi(h_{11/2})^2 s_{1/2} \otimes \nu(f_{7/2})^2 h_{9/2}$ configurations it is $22^-$ and $21^-$, none of which correspond to the assigned spin-parity of $(19^-)$. Clearly, the isomer cannot be constructed from such simple configurations.

Further insight into the nucleon configuration for the $(19^-)$ isomer comes from decay paths parallel to the 1002 keV $(19^-) \rightarrow (16^+)$ transition. Two alternative decay paths from the $(19^-)$ to the $(16^+)$ state have been observed; a $(19^-) \rightarrow (17^+)$

M2 followed by a $(17^-) \rightarrow (16^+)$ M1, and a $(19^-) \rightarrow (16^+)$ E3 followed by a $(16^+) \rightarrow (16^+)$ E0. Both of these paths require two transitions while the 1002 keV E3 is capable of making the same structural change in a single step. Such a structure could be achieved by exciting a neutron in the $f_{7/2}$ orbital to the $i_{13/2}$ orbital either directly, incurring a single transition, or via the $h_{9/2}$ orbital, incurring two transitions. A similar structure is observed in $^{153}$Yb [49], which is one neutron above the $N = 82$ shell closure, where from a $\nu f_{7/2}$ ground state configuration the neutron can be excited to the $i_{13/2}$ state directly or in two steps via the $h_{9/2}$ state.

For proton pair breaking to result in a similar structure at least one of the transitions, in the decay paths with two transitions, must be of high enough energy to account for the pair-breaking energy. The energy required to break a proton pair in this region is ∼800-1500 keV [45,47–49], considerably greater than those observed to de-excite the $^{158m2}$Ta$_{(19^-)}$ isomer. For this reason, proton pair breaking is not presently considered to be a mechanism for constructing the $(19^-)$ isomer. This leaves $\pi h_{11/2} \otimes \nu f_{7/2} h_{9/2} i_{13/2}$ as the most probable configuration for the $^{158m2}$Ta$_{(19^-)}$ isomer.

The issue of the spin and parity assignments for this state still remains. It seems that in the case of this isomer, the state of spin $j - 1$ is the lowest in excitation energy in the $\pi h_{11/2} \otimes \nu f_{7/2} h_{9/2} i_{13/2}$ configuration. Other examples of isomeric states adopting the $j - 1$ state as the lowest in excitation energy have been observed. One such example particularly noteworthy is the $19^-$ isomer in the $N = 85$ isotone $^{152}$Ho [52].

The $19^-$ isomer in $^{152}$Ho is very much analogous to the $^{158m2}$Ta$_{(19^-)}$ isomer. It has the same spin and parity assignments and the same neutron valency suggesting the possibility that they share a common coupling mechanism. It has been suggested that the $j - 1$ state in $^{152}$Ho is obtained for the isomer by coupling the valence neutrons to a three-proton multiplet whose angular momentum contribution is one

unit of angular momentum less than at full alignment [52]. Although additional proton pairs contribute to the configuration they are not considered to be broken as they have not been aligned. This means that the large energies required to break a proton pair would not be expected to be observed. The $19^-$ isomer in $^{152}$Ho is assigned a $[\pi(h_{11/2})^3_{9/2^-} \otimes \nu(f_{7/2}h_{9/2}i_{13/2})_{29/2^+}]_{19^-}$ configuration. This phenomenon is known as the "$j-1$ anomaly" [54–58].

Holmium has 67 protons which can be considered to be three valence protons above a Gadolinium core. As such, the coupling of a three proton multiplet to valence neutrons is plausible. Tantalum has an additional six valence protons to holmium, however, it is still possible to consider a three-particle multiplet if the $2d_{3/2}$ and $3s_{1/2}$ are filled before $1h_{11/2}$, or if the proton holes in the $1h_{11/2}$ are considered. These considerations make the behaviour of the $19^-$ isomers in $^{152}$Ho and $^{158}$Ta comparable, a justification for assigning the $[\pi(h_{11/2})^3_{9/2^-} \otimes \nu(f_{7/2}h_{9/2}i_{13/2})_{29/2^+}]_{19^-}$ configuration to the $^{158m2}\text{Ta}_{(19^-)}$ isomer.

An alternative mechanism to obtain this spin and parity assignment comes from the proposed explanation for the $(25/2^-)$ isomer in $^{155}$Lu [4] based on the proposed configurations of states in $^{151}$Ho and $^{153}$Tm [38,39], as previously discussed in Chapter 4.2. In the case of the $^{155}\text{Lu}_{(25/2^-)}$ isomer, the assigned spin of the state is one less than that of a fully aligned $\pi h_{11/2} \otimes \nu h_{9/2}f_{7/2}$ configuration. The mechanism proposed to account for this is a strong $[\pi h_{11/2}\nu h_{9/2}]_{1^+}$ attraction resulting in a higher seniority configuration, $[\pi(h_{11/2})^3_{9/2^-} \otimes \nu h_{9/2}f_{7/2}]_{(25/2^-)}$, at lower excitation energy.

Applying the $[\pi h_{11/2}\nu h_{9/2}]_{1^+}$ attraction to the $^{158m2}\text{Ta}_{(19^-)}$ isomer enables the spin assignment for the isomer to be constructed with a $[\pi(h_{11/2})^3_{9/2^-} \otimes \nu i_{13/2}h_{9/2}f_{7/2}]_{19^-}$ configuration. As such, the seniority inversion observed in $^{155}$Lu can describe the assigned spin and parity of the $^{158m2}\text{Ta}_{(19^-)}$ isomer.

There are a number of interesting similarities between the "$j-1$ anomaly" and

seniority inversion arguments for the assigned configuration. Both require a three-proton multiplet with the same substate population $(+j, -j, +(j-1))$ and both require coupling with valence neutrons for the effect to be observed. The main difference between the two arguments is that the "$j-1$ anomaly" considers two particles within the three-particle multiplet to couple to $0^+$ while seniority inversion relies on a particular coupling of an $h_{11/2}$ proton and an $h_{9/2}$ neutron. As the two mechanisms describe the observed effect in $^{158}$Ta so similarly it is not currently possible to comment on which plays the dominant role, however, the consistency of the substate occupancy between them means that a nucleon configuration of $[\pi(h_{11/2})^3_{9/2} \otimes \nu f_{7/2} h_{9/2} i_{13/2}]_{19^-}$ can be assigned to the $^{158m2}\mathrm{Ta}_{(19^-)}$ isomer.

### 5.2.3 Configurations above the $(19^-)$ isomer

Above the $(19^-)$ isomer the availability of nucleons to construct levels with greater angular momentum is limited to the two valence neutrons in the $f_{7/2}$ and $h_{9/2}$ orbitals, without breaking a proton pair. As previously stated, in this region of the nuclear chart it takes ∼800 to 1500 keV to break a proton pair and as the first three transitions above the $(19^-)$ isomer are all significantly less than this it has been assumed that the valence neutrons are responsible for the first three states above the $(19^-)$ isomer. Above these levels, proton pair breaking can take the nucleus to higher spin.

Neutron excitation into the $1i_{13/2}$ orbital can only account for two of the first three states above the isomer as there are only two units of angular momentum to be gained, therefore there must be another source of angular momentum. As the $20^-$ state was not observed to be the isomer following the excitation of a neutron into the $1i_{13/2}$ orbital, the fully aligned $\pi h_{11/2} \otimes \nu f_{7/2} h_{9/2} i_{13/2}$ configuration may construct a level at higher spin. This stands as further evidence that the $j-1$ spin assignment to the isomer is correct.

The next two states are then expected to be constructed from the $[\pi h_{11/2} \otimes \nu(i_{13/2})^2 f_{7/2}]_{21^+}$ and $[\pi h_{11/2} \otimes \nu(i_{13/2})^3]_{22^-}$ configurations. Excited states at higher energies and angular momenta are constructed following proton pair breaking, which is supported by the significantly larger transition energies feeding the $(22^-)$ state. Further detail has not been deduced due to the absence of reliable multipolarity information.

### 5.2.4 Systematics across $N = 85$ isotones

Recent work on $N = 85$ isotones [4] increasing in atomic number $Z$ from $^{149}$Gd, as shown in Figure 5.21, has revealed a number of interesting features. In particular, the clear lowering in excitation energy of states based on the $\pi h_{11/2} \otimes \nu(f_{7/2})^2 h_{9/2}$ (doubly-odd) and $\nu(f_{7/2})^2 h_{9/2}$ (odd-$A$) configurations ($10^+$, $12^+$, $14^+$ and $16^+$, $9/2^-$, $13/2^-$,$17/2^-$ and $21/2^-$) with respect to those based on the $\pi h_{11/2} \otimes \nu(f_{7/2})^3$ (doubly-odd) or $\nu(f_{7/2})^3$ (odd-A) configurations ($9^+$, $11^+$ and $13^+$, $7/2^-$, $11/2^-$ and $15/2^-$).

This lowering in excitation energy of states based on neutron occupation of the $h_{9/2}$ orbital relative to those based on neutron occupation of the $f_{7/2}$ orbital can be interpreted as an attraction between nucleons occupying the $h_{11/2}$ and $h_{9/2}$ spin-orbit partners. Increasing the proton occupation of the $h_{11/2}$ orbital increases that attraction, resulting in the phenomenon observed across the $N = 85$ isotones. Those states that are not lowered relative to the $\pi h_{11/2} \otimes \nu(f_{7/2})^3$ (doubly-odd) or $\nu(f_{7/2})^3$ (odd-$A$) configurations, with increasing proton number, are considered not to occupy the $\nu h_{9/2}$ orbital.

Plotting the excitation energies of states in $\pi h_{11/2} \otimes \nu(f_{7/2})^2 h_{9/2}$ and $\nu(f_{7/2})^2 h_{9/2}$ configurations relative to the $10^+$ and $9/2^-$ states, as shown in Figure 5.22, further reveals that these states maintain a rather constant trend with increasing proton number. This trend suggest that there is no additional interaction between the $h_{11/2}$ protons and $h_{9/2}$ neutrons, adding strength to the argument the these states

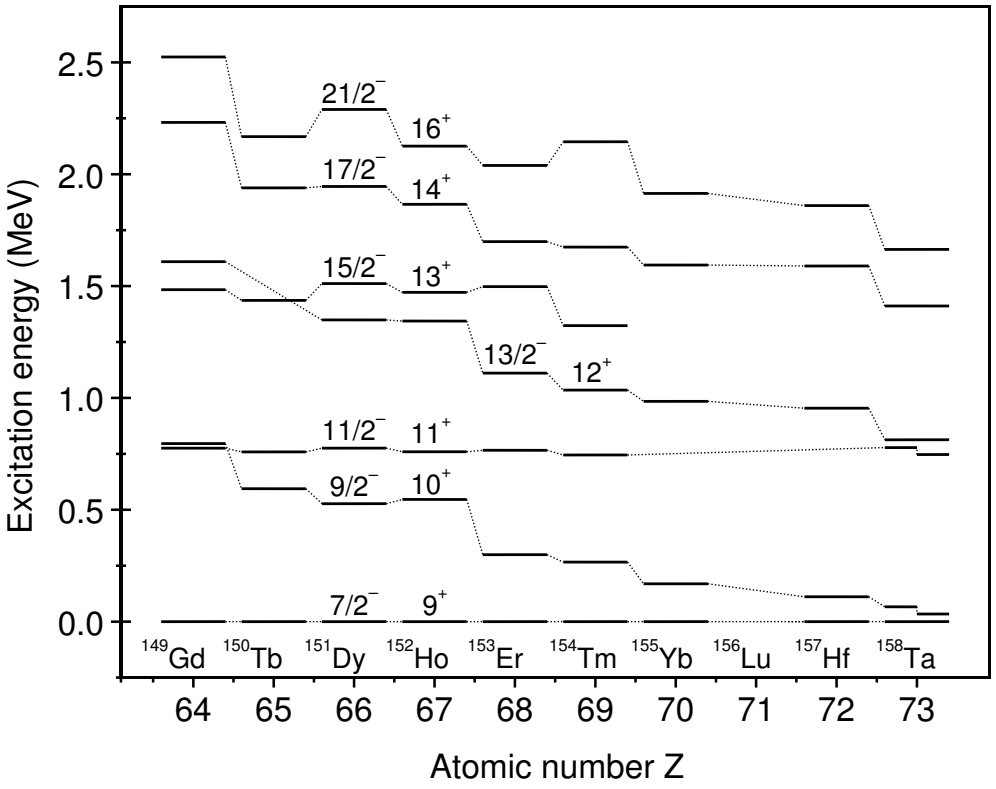


Figure 5.21: Excitation energies of states in $N = 85$ isotones above $^{149}$Gd relative to the $9^+$ or $7/2^-$ states [4, 42, 52, 59–63]. Both of the likely possibilities for the $10^+$ and $11^+$ states in $^{158}$Ta are displayed. Due to the absence of experimental clarification of a $9^+$ state, states in $^{156}$Lu, $^{159}$W and $^{160}$Re are not plotted. States based on the $\pi h_{11/2} \otimes \nu(f_{7/2})^3$ (doubly-odd) and $\nu(f_{7/2})^3$ (odd-$A$) configurations remain rather constant with increasing proton number. In contrast, states based on the $\pi h_{11/2} \otimes \nu(f_{7/2})^2 h_{9/2}$ (doubly-odd) and $\nu(f_{7/2})^2 h_{9/2}$ (odd-$A$) configurations are lowered in excitation energy with increasing proton number.

are constructed by coupling to a pair of $f_{7/2}$ neutrons rather than increasing the neutron population of the $h_{9/2}$ orbital.

The energy difference between the $9^+$ ($7/2^-$) and $10^+$ ($9/2^-$) states has been previously observed to drop to 111 keV in $^{157}$Hf. Observations of excited states in $^{159}$W and $^{160}$Re have not identified transitions between the two states, possibly as a result of the poor detection efficiencies at such low energies [6]. It is also possible that the two levels have inverted. In this work, the energy difference has been observed to have dropped as low as either 34 or 66 keV. The current explanation for the absence

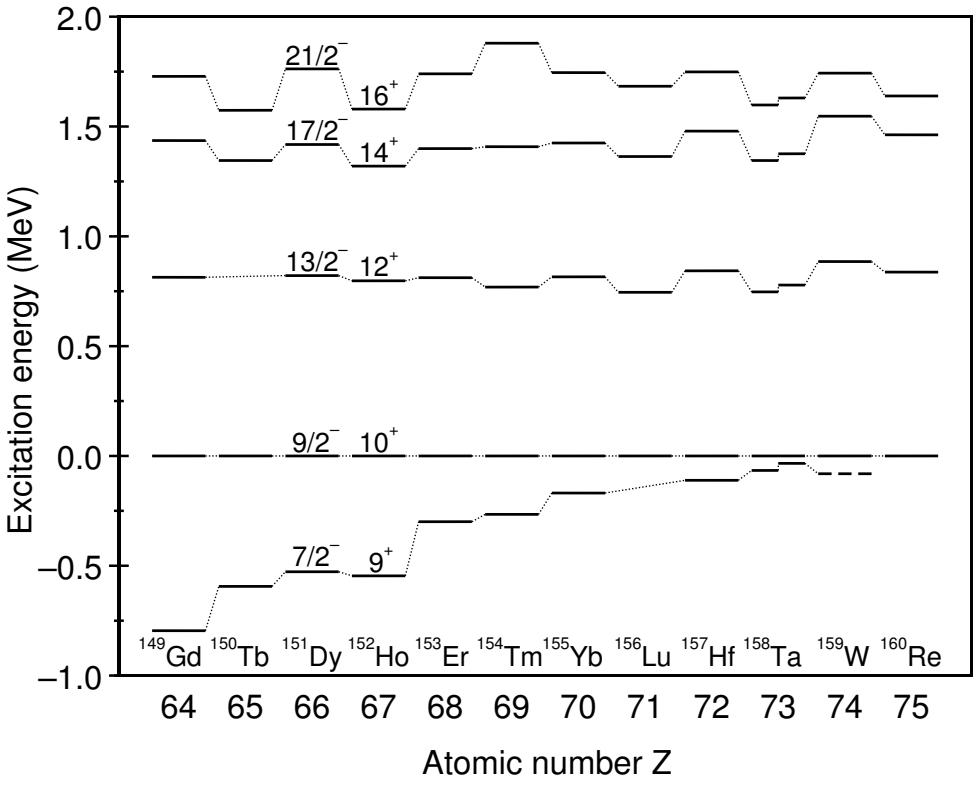


Figure 5.22: Excitation energies of levels in $N = 85$ isotones above $^{149}$Gd relative to the $10^+$ or $9/2^-$ states [4, 6, 42, 52, 59–63]. Both possible structures in $^{158}$Ta are displayed. The $\pi h_{11/2} \otimes \nu(f_{7/2})^2 h_{9/2}$ and $\nu(f_{7/2})^2 h_{9/2}$ structures are constant across the isotones. The difference in excitation energy between the $9^+$ and $10^+$ (or $7/2^-$ and $9/2^-$) states decreases with increasing $Z$.

of an observed $10^+ \rightarrow 9^+$ transition in $^{156}$Lu is that it lies in a region of low-energy detection efficiency [4]. Based on the $10^+ \rightarrow 9^+$ transition energies observed in doubly-odd $^{154}$Tm and $^{158}$Ta the energy for the $10^+ \rightarrow 9^+$ transition in $^{156}$Lu would be expected to lie between 34 and 266 keV. While this does not completely rule out the current explanation for its absence, extrapolation from systematic trends place this transition closer to ∼120 keV in energy, which may have been observable in the previous work. This introduces the possibility that there is a different explanation for the absence of an observable $10^+ \rightarrow 9^+$ transition in $^{156}$Lu.

### 5.2.5 High-spin isomerism beyond the proton drip line

The case of the $(19^-)$ isomer observed in this work is interesting in that it is sufficiently long lived for $\alpha$ decay to compete with $\gamma$ decay, yet it appears to be relatively stable with respect to proton decay despite a large proton Q-value of $Q_p = 3260$ keV [5, 40, 50]. Nuclei beyond the proton drip line are proton unbound and at higher excitation energies containment by the Coulomb barrier is less effective. Excited states whose $\gamma$-decays are relatively slow would be expected to decay via proton emission, however, as observed in the $(19^-)$ isomer in $^{158}$Ta no such proton decay is observed. This must be due to the centrifugal barrier, which dominates the Coulomb barrier in the case of protons carrying large angular momenta.

This isomer is currently unique in that it has the highest $Q_p$ of any known particle decaying state yet it remains stable to proton decay. Although it is essentially impossible to predict the existence of isomers with particular precision [64], the observation of such a state in $^{158}$Ta introduces the possibility that other high-spin isomeric states exist beyond the proton drip line, providing an opportunity to further probe nuclear structure in this region. This has broader consequences for the field as neutrons are also contained by the centrifugal barrier thus it is possible that similar high-spin isomeric states exist beyond the neutron drip line. The search for such isomers, when studies beyond the neutron drip line are achievable, may enable useful studies in regions where nuclear structure has no current experimental benchmarks.

## 5.3 Conclusions

Excited states in proton-unbound doubly odd $^{158}$Ta have been observed for the first time using $\gamma$-ray spectroscopy techniques. The deduced level scheme and assigned single-particle configurations are shown in Figure 5.23. Nuclei have been produced in fusion evaporation reactions and the two previously known $\alpha$ decays have been

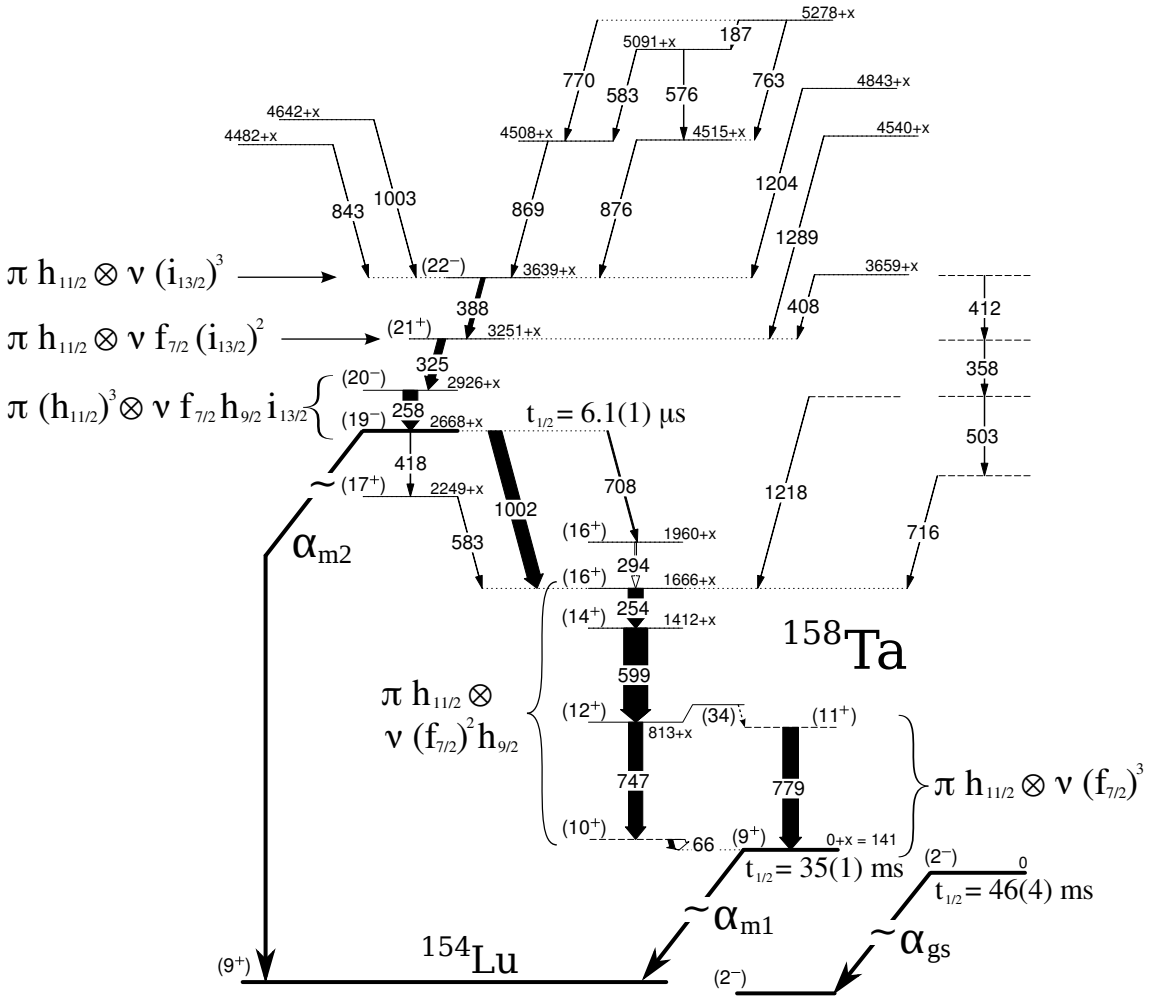


Figure 5.23: Level scheme for $^{158}$Ta based on analysis in this work with deduced nucleon configurations.

used to identify transitions associated with $^{158}$Ta nuclei using the RDT technique. No transitions have been observed feeding the $(2^-)$ state due to the limited state population in fusion evaporation reactions. Many transitions have been identified feeding the $(9^+)$ state and the presence of a isomer at high spin has made it possible to construct a scheme of low-lying levels with confidence.

Structures feeding the $(9^+)$ $\alpha$-decaying state have been assigned nucleon configurations based on valence nucleons in the $\pi h_{11/2} \otimes \nu(f_{7/2})^3$ and $\pi h_{11/2} \otimes \nu(f_{7/2})^2 h_{9/2}$ configurations, consistent with neighbouring $N = 85$ isotones. Systematic trends

in these isotones are adhered to by $^{158}$Ta, which features a lowering in excitation energy with increasing $Z$ of states built on the $\pi h_{11/2} \otimes \nu(f_{7/2})^2 h_{9/2}$ configuration.

Both $\alpha$ and $\gamma$ decays have been observed to depopulate a high-spin isomer. A spin and parity of $(19^-)$ has been assigned to this isomer based on calculations of the reduced decay width of the $\alpha$ decay combined with Weisskopf estimates for transitions below the isomer, which constrain the assignment. A comparable isomeric state with the same spin and parity assignment exists in the $^{152}$Ho isotone. The proposed nucleon configuration for this isomer is $[\pi(h_{11/2})^3_{9/2^-} \otimes \nu f_{7/2} h_{9/2} i_{13/2}]_{19^-}$.

Above the high-spin isomer, configurations are considered to been constructed from further neutron excitations into the $i_{13/2}$ orbital. Above the $\pi h_{11/2} \otimes \nu(i_{13/2})^3$ configuration, proton pair breaking is responsible for states at higher excitation energies.

Similar to observations of $N = 84$ isotones, levels based on $\pi h_{11/2} \otimes \nu f_{7/2}$ configurations exhibit a constant trend across $N = 85$ isotones, the increasing proton number having little effect on their excitation energies. This suggests that the interactions between the $h_{11/2}$ protons and $f_{7/2}$ neutrons are very weak. This differs considerably for states based on neutron occupation of the $h_{9/2}$ orbital. The excitation energy of these states decreases with increasing $Z$, which implies that the $h_{11/2}$ protons and $h_{9/2}$ neutrons experience a strong interaction. The increase in proton number will increase the strength of such interactions, lowering the excitation energy of the state.

All of the states based on the $\pi h_{11/2} \otimes \nu(f_{7/2})^2 h_{9/2}$ configuration maintain very similar excitation energies to each other relative to the $10^+$ state. This regularity suggests that $f_{7/2}$ neutrons are responsible for the structure, which further suggests that another neutron in the $h_{9/2}$ orbital would not experience the strength of the interaction with the $h_{11/2}$ protons as the first. It seems likely that a specific interaction between the $h_{11/2}$ protons and $h_{9/2}$ neutrons is particularly strong, facilitating an

interaction for only one neutron, which blocks $h_{11/2}$ proton interactions with other $h_{9/2}$ neutrons.

The single-particle structures observed in $^{158}$Ta provide a rigorous test for nuclear models. Reproduction of the range of phenomena exhibited as a result of the complex interactions between the individual nucleons, beyond the proton drip line, will extend our understanding of the atomic nucleus and the physics that it contains.

No proton decays have been observed to depopulated the high-spin isomer, despite the large proton Q-value. This indicates the importance of the centrifugal barrier in this region and introduces the possibility of more isomers existing at high-spin beyond the proton drip line. As neutrons are also affected by the centrifugal barrier, the presence of this $(19^-)$ isomer beyond the proton drip line is an indication that high-spin isomers may exist beyond the neutron drip line. When studies beyond the neutron drip line become achievable, searching for such isomers would be a valuable task as they may prove to be a useful probe of nuclear structure far from stability.

# Chapter 6

# Summary

In this work, excited states in two neutron-deficient nuclei in close proximity to the proton drip line and having few neutrons above the $N = 82$ shell closure have been studied. The experimental apparatus at the Accelerator Laboratory at the University of Jyväskylä has made it possible to produce, identify and study these nuclei in more detail than has been achieved previously.

The study of the odd-$A$ nucleus $^{155}$Lu using $\gamma$-ray spectroscopy techniques has enabled the previous work to be revised and extended. For the first time, the transition depopulating the $(23/2^-)$ state has been observed, proving that it is higher in excitation energy than the $(25/2^-)$ state, which is isomeric. States up to $(23/2^-)$ are assigned a $\pi h_{11/2} \otimes \nu(f_{7/2})^2$ configuration. The rather constant trend exhibited by these states across the $N = 84$ isotones indicates limited interaction between $h_{11/2}$ protons and $f_{7/2}$ neutrons.

The level scheme above the $(25/2^-)$ $\alpha$-decaying state has been significantly revised and extended in this work. The $(25/2^-)$ isomer and $(27/2^-)$ state are considered to be of a $\pi h^n_{11/2} \otimes \nu f_{7/2} h_{9/2}$ configuration where the proton seniority $n = 1$ for the $(27/2^-)$ state and $n = 3$ for the $(25/2^-)$ isomer. Comparison with neighbouring $N = 84$ isotones has revealed a systematic lowering in excitation energy of

the $(25/2^-)$ state relative to the $(11/2^-)$ state with increasing proton number. This behaviour is not observed in the $(27/2^-)$ state. Strong interactions between $h_{11/2}$ protons and $h_{9/2}$ neutrons due to their spatial overlap is the suggested mechanism for the lowering of the $(25/2^-)$ state with increasing proton number. The constant trend displayed by the $(27/2^-)$ state indicates that not all $h_{11/2}$ protons and $h_{9/2}$ neutrons experience this strong attraction.

The states immediately above the $(27/2^-)$ state have been assigned a $\pi h_{11/2} \otimes \nu f_{7/2} i_{13/2}$ configuration up to the fully aligned $(31/2^+)$ state. States based on similar configurations have been observed in the isotones. Proton pair breaking accounts for states above the $(31/2^+)$ state. More specific assignments have not been made in this work.

Excited states in the doubly-odd nucleus $^{158}$Ta have been observed for the first time in this work. Gamma-ray spectroscopy techniques have been used to construct a level scheme from which single-particle structures have been ascertained. The RDT technique has been used to identify transitions feeding the $(9^+)$ state, which is assigned the $\pi h_{11/2} \otimes \nu f_{7/2}$ configuration. This state is fed by two different structures. The $\pi h_{11/2} \otimes \nu (f_{7/2})^3$ configuration corresponds to neutron pair breaking to achieve higher spin. The $\pi h_{11/2} \otimes \nu h_{9/2} (f_{7/2})^2$ configuration corresponds to the excitation of the the odd neutron into the $h_{9/2}$ orbital, forming the $(10^+)$ state, and neutron pair breaking to achieve the fully aligned $(16^+)$ state.

The behaviour of states based on these two separate configurations across the $N = 85$ isotones is observed to be different. Those in the $\pi h_{11/2} \otimes \nu (f_{7/2})^3$ configuration exhibit a constant trend, relative to the $9^+$ state, with increasing proton number. Configurations that include a neutron in the $h_{9/2}$ orbital experience a decrease in excitation energy, relative to the $9^+$ state, with increasing proton number. This is similar to the phenomena observed in $N = 84$ isotones and is indicative of a strong interaction between $h_{11/2}$ protons and $h_{9/2}$ neutrons.

A high-spin isomeric state with a half-life of 6.1(1) $\mu$s, which exhibits $\alpha$-decay and $\gamma$-ray branches, has been observed for the first time and has been assigned $(19^-)$ spin and parity based on reduced decay width and Weisskopf estimate arguments. Although the proton-decay Q-value of this state is high at 3260 keV, no proton emission is observed. Proton emission from this state would be hindered by the centrifugal barrier. Such an observation introduces the possibility that similar isomers could exist in other nuclei beyond the proton drip line. Such isomers would prove to be valuable probes of nuclear structure in proton unbound nuclei. This observation has broader consequences for the field as neutrons are also affected by the centrifugal barrier. The possibility of high-spin isomers beyond the neutron drip line is very exciting for nuclear structure studies far from stability. When studies beyond the neutron drip line become achievable, such isomers may prove to be an useful probe of nuclear structure in regions that presently have no experimental benchmarks.

# Bibliography


[1] K. S. Krane, *Introductory Nuclear Physics* (John Wiley & Sons, 1988).

[2] R. B. Firestone, *Table of Isotopes* (John Wiley & Sons, 1996).

[3] National Nuclear Data Center, http://www.nndc.bnl.gov/, Accessed: 19/03/2012.

[4] K. Y. Ding *et al.*, Phys. Rev. C **64**, 034315 (2001).

[5] R. D. Page, Phys. Rev. C **83**, 014305 (2011).

[6] P. J. Sapple *et al.*, Phys. Rev. C **84**, 054303 (2011).

[7] R. D. Woods and D. S. Saxon, Phys. Rev. **95**, 577 (1954).

[8] M. G. Mayer, Phys.Rev. **75**, 1969 (1949).

[9] O. Haxel, J. Hans, D. Jensen, and H. E. Suess, Phys. Rev. **75**, 1766 (1949).

[10] A. H. Wapstra, *Nuclear spectroscopy tables* (North-Holland, Amsterdam, 1959).

[11] V. F. Weisskopf, Phys. Rev. **83**, 1073 (1951).

[12] G. Gamow, Z. Phys. **51**, 204 (1928).

[13] A. Leppänen, 2005, Research report No. 5/2005, University of Jyväskylä.

[14] J. O. Rasmussen, Phys.Rev. **113**, 1593 (1959).

[15] G. Igo, Phys. Rev. Lett **1**, 72 (1958).

[16] E. S. Paul *et al.*, Phys.Rev. **C51**, 78 (1995).

[17] F. A. Beck, Prog. Part. Nucl. Phys. **28**, 443 (1992).

[18] P. J. Nolan, F. A. Beck, and D. B. Fossan, Annu. Rev. Nucl. Phys. Part. Sci. **45**, 561 (1994).

[19] D. Seddon, 2008, Private communication.

[20] C. W. Beausang *et al.*, Nucl. Instr. and Meth. A **313**, 37 (1992).

[21] M. Leino *et al.*, Nucl. Instr. and Meth. B **99**, 653 (1995).

[22] R. D. Page *et al.*, Nucl. Instr. and Meth. B **204**, 634 (2003).

[23] I. H. Lazarus *et al.*, IEEE Trans. Nucl. Sci. **48**, 567 (2001).

[24] P. Rahkila, Nucl. Instr. and Meth. A **595**, 637 (2008).

[25] E. L. Grigorescu *et al.*, Appl. Radiat. Isot. **56**, 435 (2002).

[26] U. Schötzig, K. Debertin, and K. F. Walz, Appl. Radiat. Isot. **28**, 503 (1977).

[27] R. D. Macfarlane, Phys.Rev. **137**, 1448 (1965).

[28] S. Hofmann, W. Faust, G. Münzenberg, W. Reisdorf, and P. Armbruster, Z. Phys. A **291**, 53 (1979).

[29] S. Hofmann *et al.*, Z. Phys. A **333**, 107 (1989).

[30] K. S. Toth and W. Nazarewicz, Phys.Rev.C **48** (1993).

[31] K. S. Toth *et al.*, Phys.Rev.C **44**, 1868 (1991).

[32] D. Seweryniak *et al.*, ANL/PHY-97/1 , 247 (1996).

[33] J. A. Cizewski, K. Y. Ding, and M. B. Smith, Acta Physica Polonica B **32**, 933 (2001).

[34] A. Gavron, Phys. Rev. C **21**, 230 (1980).

[35] O. B. Tarasov and D. Bazin, Nucl. Intstr. Meth. B **204**, 174 (2003).

[36] J. McNeill *et al.*, Z. Phys. A **325**, 27 (1986).

[37] M. Lach *et al.*, Z. Phys. A **341**, 25 (1991).

[38] C. T. Zhang *et al.*, Z.Phys.A **348**, 65 (1994).

[39] C. T. Zhang *et al.*, Z.Phys.A **348**, 249 (1994).

[40] R. D. Page *et al.*, Phys. Rev. C **53**, 660 (1996).

[41] T. Kibédi, T. W. Burrows, M. B. Trzhaskovskaya, P. M. Davidson, and C. W. N. Jr., Nucl. Instr. and Meth. A **589**, 202 (2008).

[42] A. F. Saad *et al.*, Z. Phys. A **351**, 247 (1995).

[43] K. S. Toth *et al.*, Phys.Rev.C **38**, 1932 (1988).

[44] J. Gizon *et al.*, Z. Phys. A **301**, 67 (1981).

[45] D. Seweryniak *et al.*, Phys. Rev C **71**, 054319 (2005).

[46] P. Federman and S. Pittel, Phys. Rev. C **20**, 820 (1979).

[47] A. Kuhnert *et al.*, Phys. Rev. C **46**, 486 (1992).

[48] C. T. Zhang *et al.*, Z. Phys. A **345**, 327 (1993).

[49] J. H. McNeill *et al.*, Z. Phys. A , 369 (1993).

[50] C. N. Davids *et al.*, Phys. Rev. C **55**, 2255 (1997).

[51] A. N. Andreyev *et al.*, Nucl. Instr. and Meth. B **533**, 422 (2004).

[52] S. André *et al.*, Nucl. Phys. A **575**, 155 (1994).

[53] L. W. Nordheim, Rev. Mod. Phys **23**, 322 (1951).

[54] C. Gallagher and S. A. Moszkowski, Phys. Rev **111**, 1282 (1958).

[55] M. H. Brennant and A. M. Bernstein, Phys. Rev **120**, 927 (1960).

[56] A. Bohr and B. R. Mottelson, Dan. Mat. Fys. Medd **27** (1953).

[57] V. Paar, Phys. Lett **39B**, 587 (1972).

[58] P. Kemnitz, L. Funke, E. Will, and G. Winter, Phys. Scr. **24**, 253 (1981).

[59] M. Piiparinen *et al.*, Z. Phys. A **300**, 133 (1981).

[60] G. Duchêne *et al.*, Z. Phys. A **350**, 39 (1994).

[61] M. Piiparinen, S. Lunardi, P. Kleinheinz, H. Backe, and J. Blomqvist, Z. Phys. A **290**, 337 (1979).

[62] C. Foin, S. André, and D. Barnéoud, Z. Phys. A **305**, 81 (1982).

[63] C. Foin *et al.*, Eur. Phys. J. A **14**, 7 (2002).

[64] P. M. Walker and G. D. Dracoulis, Hyp. Int. **135**, 83 (2001).